Processing, Microstructure and Mechanical Properties of Ti_xAl_y/Al_2O_3 and $Al_2Ti_4C_2/Ti_xAl_y/Al_2O_3/TiC$ Composites

A thesis

submitted in partial fulfillment

of the requirements for the degree

of

Doctoral of Philosophy

The University of Waikato

Te Whare Wānanga o Waikato

Zhihong Cai

November 2002

Department of Materials and Processing Engineering
University of Waikato

Dedicated to my wife, Xiaoyu Si, and our family

Abstract

The Ti_xAl_y/Al_2O_3 metal-ceramic composites materials [Ti_xAl_y is α-Ti(Al,O), Ti_3Al, or TiAl] and $Al_2Ti_4C_2/Ti_xAl_y/Al_2O_3/TiC$ ceramic-ceramic composites with different volume fractions of ceramic reinforcement phases were synthesized using a complex combination of high energy mechanical milling, thermal treatment and powder consolidation processes. The thermal treatment process included reactions between carbon and TiO_2, and between Al and TiO_2, Ti_2O_3 or TiO_nC_{1-n}, which was produced by reacting TiO_2 and carbon. Heat treating C/TiO_2 composite powder produced pure Ti_2O_3. Pure TiO could not be obtained by only increasing the carbon to TiO_2 ratio in the C/TiO_2 composite powder. Instead, TiO_nC_{1-n} solid solution was formed. Reaction kinetic studies showed that higher carbon to TiO_2 ratios accelerated the reaction due to refinement of the C/TiO_2 composite structure. Reactions between Al and TiO_nC_{1-n} formed $Al_2Ti_4C_2/Al_2O_3$ ceramic-ceramic composite. When the aluminum content of the starting Al/TiO_nC_{1-n} composite powders was increased, $Al_2Ti_4C_2$ still formed, but small amounts of Ti_3Al or TiAl also formed. Producing TiC from Al and TiO_nC_{1-n} reaction depended on the value of n in the TiO_nC_{1-n} phase. When n is small enough, TiC formed; otherwise TiC did not form.

This study found that fully dense matrix phase of Ti_xAl_y/Al_2O_3 and $Al_2Ti_4C_2/Ti_xAl_y/Al_2O_3/TiC$ formed after sintering at 1550°C. The Al_2O_3 particles became fully sintered when the composites were sintered at 1650°C but not at 1550°C. The Al_2O_3 particles in the α-Ti(Al,O) and Ti_3Al based composites had a high coarsening rate above 1550°C, indicating that the oxygen and Al diffusion rates of α-Ti(Al,O) and Ti_3Al are very high at these temperatures. The Al_2O_3 particles in TiAl based composites also had a high coarsening rate above 1550°C, caused by TiAl being liquid at these temperatures. The Al_2O_3 particles in the $Al_2Ti_4C_2/Ti_xAl_y/Al_2O_3/TiC$ based composites had a much lower coarsening rate because of the $Al_2Ti_4C_2$ matrix the lower oxygen content and high melting point decreases oxygen and aluminum mobilty.

The size and volume fraction of Al_2O_3 particles in the composites strongly affected the mechanical properties of the Ti_xAl_y and $Al_2Ti_4C_2$ based composites. Hardness of α-Ti(Al,O), Ti_3Al, and $Al_2Ti_4C_2$ based composites was 800-1600 VHN and hardness of TiAl based composites was 150-500 VHN. Bending strength of Ti_xAl_y/Al_2O_3 composites was 105-230 MPa and bending strength of $Al_2Ti_4C_2/Ti_xAl_y/Al_2O_3/TiC$ based composites was 250-460 MPa. It appeared that 10 μm might be the critical size of Al_2O_3 particles. Below 10 μm bending strength dramatically improved with deceasing the Al_2O_3 particle size in the composites. The fracture toughness of these composites was 2-4.5MPa•$m^{1/2}$. Composite hardness increased and bending strength decreased with increasing Al_2O_3 particle size and volume fraction.

Acknowledgements

Firstly, I would like to thank my supervisor Associate Professor Deliang Zhang for supporting me for the last three years and for introducing me to the research field of metal-ceramic composites. I am fortunate to have a Foundation for Research, Science and Technology, New Zealand research scholarship.

Thanks are also given to the technicians Jijian Lu and Yuanji Zhang, for their support in the laboratory. Mr Gorgees Adam for his support and suggestions, Mr Alfred Harris for his support in the SEM unit.

Finally, to my wife and our family, thank you for everything, you are the best.

Table of Contents

Chapter One Introduction and Literature Review

Chapter Two Experimental Techniques

Chapter Three Solid State Reaction between C and TiO_2 and between TiO_2, Ti_2O_3 or TiO_nC and Al

Chapter Four Processing and Microstructure of Ti_xAl_y/Al_2O_3 and $Al_2Ti_4C_2/Ti_xAl_y/Al_2O_3$/TiC Composites

Chapter Five Mechanical Properties of Ti_xAl_y/Al_2O_3 and $Al_2Ti_4C_2/Ti_xAl_y/Al_2O_3/TiC$ Composites

Chapter Six Conclusions and Recommendations

Chapter One
Introduction and Literature Review

1.1 Introduction

Traditionally, metals and their alloys have been the main engineering materials used in many applications because of their favorable combination of strength, toughness, workability, reliability and modest cost. Ceramics, although light, abrasion resistant and capable of withstanding elevated temperature, have not been widely used for constructing primary structures or components because they lack toughness. Materials used in some areas such as the aerospace industry need to have a combination of properties such as strength, stiffness, density, durability, and ability to withstand high working temperatures. These requirements cannot be effectively satisfied by monolithic structural materials. Thus has driven research and development of advanced composites.

Low density metallic materials such as aluminum magnesium and titanium are always important in many economy areas ranging from the automobile industry to the aerospace industry. Titanium, the fourth most abundant metal in the earth's crust (behind Al, Fe and Mg), occurs mainly as rutile (TiO_2) and ilmenite ($FeTiO_3$). Titanium metal and alloys have excellent mechanical properties, including high strength and stiffness and good corrosion resistance. Titanium metal has a density of 4.5 g/cm^3 and melting point of 1675°C. The high materials and fabrication cost have limited the use of the materials in structural applications. In the automobile and construction industries, cost is extremely important, while in medical applications and in the aerospace industry performance rather than the cost is emphasized.

Research into low-cost processing of Ti or Ti-alloy based composites has great potential to expand titanium use in many areas. Materials based on Ti-alloy/ Al_2O_3 composites have many favorable properties because they combine the good mechanical properties of Al_2O_3 and Ti-alloy phases (such as high strength and hardness) with the toughness of composites.

The objective of the research in this thesis is to define the processing /microstructure/properties relationships of titanium alloy based composites materials produced using TiO_2, Al and carbon. The research also includes an investigation of the phases that form during some of the reactions in the processing.

This thesis is divided into six chapters. The first chapter is the literature review. The second chapter describes the experimental methodology used in the study. The third chapter describes and discusses the reactions that occur between TiO_2, Al, and C. The fourth chapter describes and discusses the results of a study on processing and the microstructure of Ti_xAl_y/Al_2O_3 and $Al_2Ti_4C_2/Ti_xAl_y/Al_2O_3/TiC$ based composites. The fifth chapter describes and discusses the results of a study on the mechanical properties of Ti_xAl_y/Al_2O_3 and $Al_2Ti_4C_2/Ti_xAl_y/Al_2O_3/TiC$ based composites. Finally, the sixth chapter summarizes the main conclusions and makes recommendations for future work.

1.2 Synthesis of metal ceramic composites

There are many methods to synthesize metal-ceramic composites. Including conventional solid state powder mixing and consolidation, liquid mixing, reactive or non-reactive liquid infiltration, and self-propagating high temperature synthesis. The following sections review these methods.

1.2.1 Liquid mixing

In liquid mixing processes, ceramic solid particulates are incorporated into a molten metallic matrix by mixing and then the ceramic/molten metal mixture is cast to form metal-ceramic composites. Several approaches can be taken to introduce ceramic particulates into an alloy melt. Mixing techniques generally used for introducing and homogeneously dispersing ceramic particulate or short fibers in a molten metal include: adding particles to a vigorously agitated, fully or partially molten alloy; injecting ceramic particulate or short fibres into the melt with an injection gun; dispersing pellets or briquettes formed by compressing a mixture of base alloy powder and a ceramic phase into a mildly agitated melt;

adding powders to an ultrasonically agitated melt; adding powders to an electromagnetically stirred melt; and centrifugally dispersing particles in a melt [1]. For example, an Al-Al_2O_3 composite can be prepared by adding TiO_2 particulates to aluminum melt using a vortex produced by mechanical agitation [2-3].

In all the above approaches, uniform particle dispersion in a melt is achieved by applying external force to transfer a non-wetting ceramic phase into an alloy melt and to create a homogeneous ceramic particulate suspension in the melt. After mixing ceramic particles in the metal melt, squeeze casting is often used to fabricate the metal ceramic composites [4-7].

Despite encouraging results from research on preparing metal ceramic composites via liquid mixing techniques, the process has some difficulties including ceramic particles agglomerating during agitation; ceramic particles settling; secondary phases segregating in the metallic matrix; extensive interfacial reactions occurring; and ceramic particles fracturing during mechanical agitation [8].

1.2.2 Direct oxidation of alloy melt

Direct oxidation of molten metals has been used to produce metal-ceramic composites [9]. This process can produce particulate-reinforced and fibre-reinforced composites with a wide range of compositions and microstructures. The direct oxidation process involves oxidising a bulk molten metal with a gas to produce a solid ceramic body via directed growth process from the unusual oxidation behavior. Reaction product forms initially on the exposed surface of a pool of molten metal and then grows inward. Oxide growth is maintained by transporting additional metal through the reaction product. The amount of metal remaining in the composite produced depends on the processing conditions and starting materials [10].

Direct oxidation of molten metal route has some unique features [11] including

- The composite structure typically consists of both interconnected oxide and interconnected metal phases.

- The process occurs at a high rate only over a certain temperature range. Outside this temperature range, growth rate can be several orders of magnitude lower.

The product of the direct oxidation process is a metal-ceramic composite. Composite composition is determined by the parent metal and the oxidizing atmosphere chosen. The volume fractions of the ceramic phase, the scale of the microstructure, the porosity level, and the degree of interconnectivity of the metallic phase in the product can be controlled by varying processing temperature, atmosphere and time. For example, reacting an aluminum alloy with air or oxygen produces an Al-Al_2O_3 alloy composite containing a three-dimensionally interconnected network of Al_2O_3 and Al-alloy phases [12-13].

1.2.3 Liquid metal infiltration process

In the melt infiltration process, a liquid is infiltrated into a porous ceramic body [14-16]. The melt infiltration technique can basically be divided into reactive and non-reactive processes. In non-reactive infiltration, the liquid phase simply fills the open spaces in the ceramic preform. So the process is usually simple. The composite material can be made with desired dimensions, shapes and density. The amount of molten metal required can be determined from the volume of open spaces in the ceramic preform. This fabrication method allows choice in selecting the amount of ceramic reinforcements. Also, near-net shape components can be produced [18].

The reactive melt infiltration process is very similar to the non-reactive infiltration. The porous preform reacts with the molten metal, often releasing considerable heat. Many variables, such as volumetric change, the amount of heat released, and reaction kinetics effect the process. A lot of research has been done on this process [19-24]. In making Al-Al_2O_3 composite by reaction infiltration of Al melt into mullite, Gao [20] has found that the composite formed in three stages. First, Al infiltrated into the mullite ceramic through grain boundaries and reacted with mullite at the grain boundaries. In the second stage, a complete reaction converted mullite to a composite of Al_2O_3 and Al-Si phase. In the final

stage, the Si produced by reducing SiO_2 diffused from the Al/Al_2O_3 composite through the molten metal channels.

1.2.4 Powder mixing and consolidation

Powder mixing and consolidation has been successfully applied to a large number of metal/ceramic combinations to fabricate ceramic reinforced metal matrix composites [25-27]. Ceramic particles dispersion and characteristics of the particle-matrix interface depend on the processing conditions. This method involves several steps before the final consolidation. The powder mixing and consolidation method usually consists of the following steps: [8] De-agglomeration of ceramic reinforcement and metal powders, Mixing and degassing, Green compact consolidation, Primary processing: rolling, extrusion, forging, Secondary processing: forming, joining, machining.

The powder mixing and consolidation route has several attractive features [28]. The reaction between the metal matrix and the ceramic particles can be minimized by solid state processing. Effective control of volume fraction of reinforcements is also possible. The techniques used for consolidating the mixed powder include normally pressure-less sintering, hot isostatic pressing, or hot pressing. Understanding the kinetics of composite densification with a range of ceramic volume fractions increases effective use of the consolidation methods. With a low volume fraction of ceramic phase, composite densification is controlled by the matrix phase. However, the ceramic phase still influences local densification kinetics, and normally reduces densification rate [29-30].

To produce a metal-ceramic composite with a high volume fraction of ceramic phase, two phases must have the same densification rate. Achieving sintering rate uniformity across a composite is a considerable challenge because the nature of each phase affects sintering rate significantly. The ceramic phase generally densifies far slower than the metals. Fine modification of sintering kinetics of a composite must be done so that each composite phase can densify at the same rate under identical temperature and pressure conditions. This can be accomplished by a variety of methods. Powder particle size can affect sintering kinetics as when

sintering Mo-AlN composites [31] and ZrO_2-Ni composites [32]. A small quantity of sintering aid can increase the sintering rate of the ceramic phase. For examples, adding Fe_2O_3 lowered sintering temperature of MgO to near that of nickel [33], and adding Cr_3C_2 increased the sintering rate of TiC to match the sintering rate of Ni_3Al [34].

1.2.5 The SHS method

Past decade, there has been a great interest in synthesizing advanced materials by solid-state combustion. Combustion synthesis of materials can be conducted in two modes [29]; the self-propagating high-temperature synthesis (SHS) mode and the thermal explosion mode. In the self-propagating high-temperature synthesis mode, highly exothermic reactions become self-sustaining and yield the final product initiated by an external energy source without requiring additional heat. The thermal explosion mode is also called reactive sintering, and is achieved by heating the sample uniformly in a controlled manner until the reaction occurs simultaneously throughout the volume.

The concept of solid-state exothermic reaction was known for a long time. Metalothermic reactions were discovered by Beketov in 1865 [29] and combustion synthesis was started by Goldschmidt in 1895 [30]. Since then, a substantial and continuously increasing research effort has developed more than 300 compounds and metal ceramic composites (e.g. TiC-Ni, TiC- (Ni, Mo), WC-Co, Cr_2C_3- (Ni, Mo)) [31].

The SHS process needs energy for igniting. Normally it is difficult to ignite a gas-less system. The self-propagation combustion process involves two steps; firstly, reaction initiation and then reaction self-propagation. There is extensive literature on theoretical and experimental studies of the mechanism of combustion reaction [32-42].

Zhang et al. [33] has proposed a model for the reaction (equation 1-1) process as shown in Figure 1.1.

$$A_{(s)} + B_{(s)} \rightarrow AB_{(s)} \qquad (1\text{-}1)$$

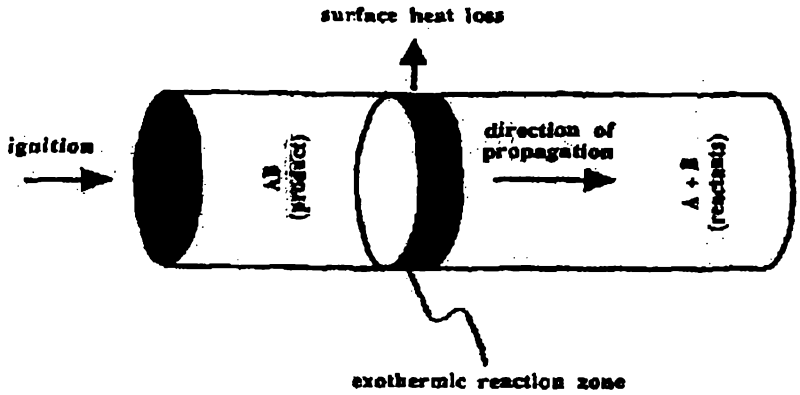

Figure. 1.1 Reaction configuration of SHS [33].

The ignition criteria for a condensed system is related to local heat generation, activation energy of the reaction, and surface heat loss by convection and radiation [33].

Bowen and Derby have used a finite-difference method to model SHS process. They considered the reactants as a one-dimensional array of cells initially at room temperature. When the first two cells are ignited to combustion temperature, heat energy will be transferred to the third cell. Once the third cell is ignited, the reaction begins to propagate. The reaction becomes self-propagating if equation 1-2 is satisfied.

$$\frac{(T_{ad} - T_{ig})}{(T_{ig} - T_{start})} \geq \frac{C_p(\text{reactants})}{C_p(\text{products})} \qquad 1\text{-}2$$

Where T_{ad} is adiabatic combustion temperature, T_{ig} is ignition temperature, T_{start} is starting temperature, and C_p is specific heat of substance. The various reactions from literature are plotted in Fig. 1.2 [38].

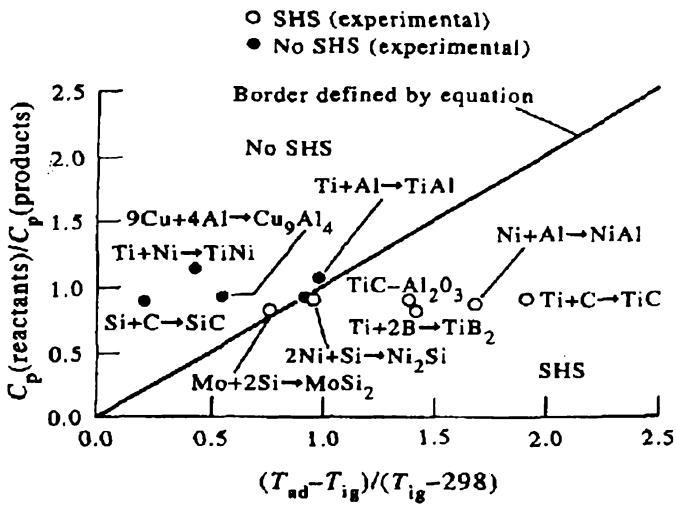

Figure 1.2 Summary of SHS reactions from published literature.

The SHS reaction has been used for producing composites. This process is economical because naturally occurring and low cost raw materials can be used. Equation 1-3 shows how the TiC/MgO composite can be prepared by reacting TiO_2, Mg, and C. This process is more economical than using elemental reactants.

$$TiO_2 + 2Mg + C = TiC + 2MgO \qquad 1\text{-}3$$

The advantage of the SHS process for preparing composites is that combustion synthesis offers the possibility of forming all compositions at the same time as the entire composite is being prepared. This is different from the typical process of first mechanically mixing ceramic particulate with the matrix material and then processing the mixture to form the composite. Many investigations have used of the SHS process to synthesize metal ceramic composites. Materials studied include Fe/TiC [44], MnNi/TiC [45], Ni/TiC, and Ti/TiB_2 composites [46].

The complexity of the kinetics of forming metal-ceramic composites was demonstrated in the study to synthesize TiC-MnNi composite [45]. The velocity of combustion decreased in composition in the range 0 to 50 wt.% of MnNi, and had minimum and maximum values at 10 and 30 wt.% of MnNi respectively. The initial decrease in combustion velocity was due to an increase in the thickness of the TiC forming on the graphite particle surface and acting as barrier. The increase in combustion velocity over 10 to 30 wt.% MnNi was due to the increase liquid phase fraction and decrease in TiC fraction. As MnNi phase increase above 30 wt%, overall reaction became weaker and combustion velocity decreased.

1.2.6 Aluminum based thermite reaction method

The thermite reaction was initially used to describe exothermic reactions had involved reducing metallic oxides with aluminum to form aluminum oxide and metals or alloys. Currently, the term thermite reaction is used to describe a much wider range of reactions involving a metal reacting with a metal or non-metal oxide to form a more stable oxide and a metal or non-metal corresponding to the reactant oxide [47]. Aluminum and zirconium have comparable reducing abilities, but aluminum is more commonly used because it is more readily available. Thermite reactions have the advantage over many combustion synthesis reactions using elemental powders because it use naturally occurring oxides. In addition, the simultaneous formation of the uniformly distributed multiple phases can be produced.

Many oxides can be reduced by aluminum because Al_2O_3 is a vary stable oxide. The general form of reaction is:

$$Al+M_xO_y \rightarrow M_xAl_y+Al_2O_3+\Delta H \quad (1\text{-}4)$$

Where: M_xAl_y is a metal aluminide or metal, and M_xO_y is a metal oxide, and ΔH is the heat generated by the reaction. A Al-based thermite reaction process is shown in Figure 1.3 [48].

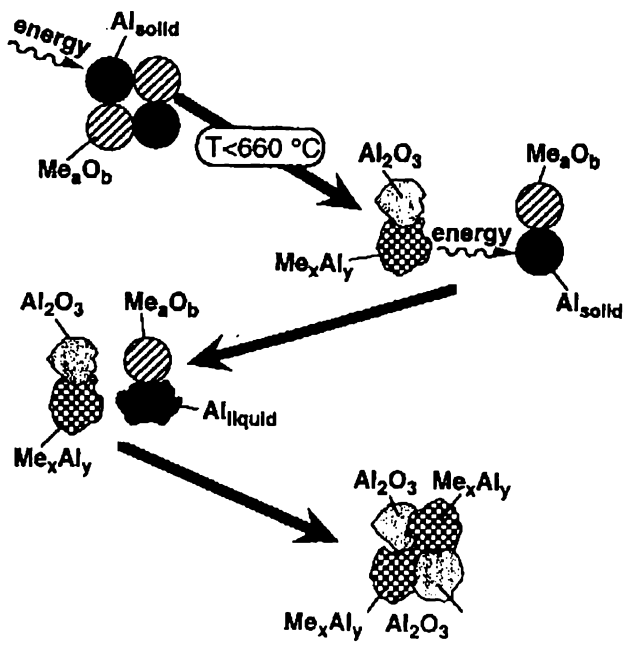

Figure 1.3 Schematic diagram of Al-based thermite reaction [48].

The oxides of many metals including Ti, Fe, Ni, Cr, V, and W, can be reduced by Al [48-53]. Carbon, Si, or B are commonly used as reducing agents to form metallic carbides (e.g. TiC), silicides (e.g. $MoSi_3$), or borides (e.g. TiB_2) and Al_2O_3 ceramic composite materials [54-61].

Variation of these classic thermite-based reactions was recently used to produce alumina-aluminide alloys (3A) composites with inter-penetrating networks [62]. The 3A process involves a novel pressure-less reaction to sinter a compact of intensively milled metal oxide/Al powder in a non-oxidizing atmosphere [63]. High energy ball milling is often used to produce the fine metal oxide/Al powder. The using of high energy ball milling to produce metal-ceramic composite will be reviewed in section 1.2.7.

The kinetics of the 3A aluminum-based thermite reaction has been theoretical modeled and investigated experimental [64-65]. This process usually releases a large amount of heat. Gaus have developed a continuum model using mass and energy balances to model this exothermicity. The parameters in the model include rate of local heat generation, tactivation energy, rate of heat redistribution, and rate of heat transfer by convection and conduction.

The continuum model was then used to model formation of Ti_xAl_y-Al_2O_3 composites from sintering TiO_2/Al powder mixtures. Using a slow heating rate ($<3^oC$/min) and an inert gas with high thermal conductivity (e.g. He) instead of vacuum allowed better heat transfer via convection and helped control the reaction. The reaction may also be controlled by reducing initial reactant concentrations. This reduced melting forming a liquid phase that caused large pores during sintering. By controlling the reaction, it was possible to obtain products of several materials with wide range of compositions [66-67]. Fully dense composites were obtained using a slow heating (1^oC/min) under pressure-less sintering [68-70].

Sintering atmosphere can also affect densification. In study of $ZrAl_3/Al_2O_3$ composite [71], it was found that the using of N_2 and Ar caused only small shrinkage of samples and therefore lower final densities than using a vacuum

(Figure 1.4). This was because the gaseous species were trapped in closed pores, preventing most of the shrinkage.

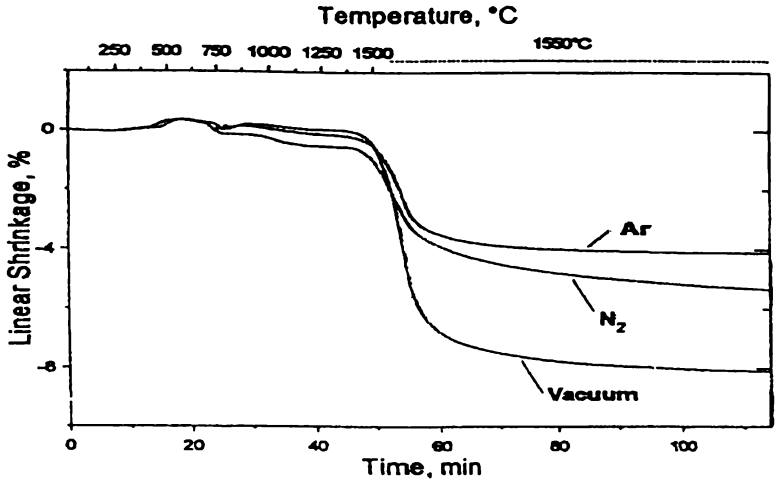

Figure 1.4 Dimensional changes of $ZrAl_3/Al_2O_3$ composites sintered in different atmospheres measured by using a dilatometer [71].

1.2.7 High energy mechanical milling techniques

Milling materials is a major practice in powder metallurgy and the ceramic processing industries. The aims of milling include changing particle shape, reducing particle size, and homogenously mixing different powders. High-energy milling is often used, it is commonly called mechanical alloying. When high-energy milling is used to achieve solid state alloying [72]. This process was originally developed by Benjamin and colleagues in their study on mechanical alloying of nickel-based superalloy. As more research was done it became clear that high energy ball milling was a universal method for producing materials with a metastable microstructure. Research in high-energy ball milling has since blossomed into other areas including [73]: modeling the ball milling process and phase formation during mechanical alloying [74], amorphization by mechanical alloying [75], milling of immiscible systems [76] and synthesis of nanocrystalline materials by ball milling [77-83].

High-energy milling of a powder is a complex dynamic process. During mechanical milling, the powder particles are plastically deformed, cold welded and fractured repeatedly. A composite structure is formed in each powder particle (Figure 1.5) [84].

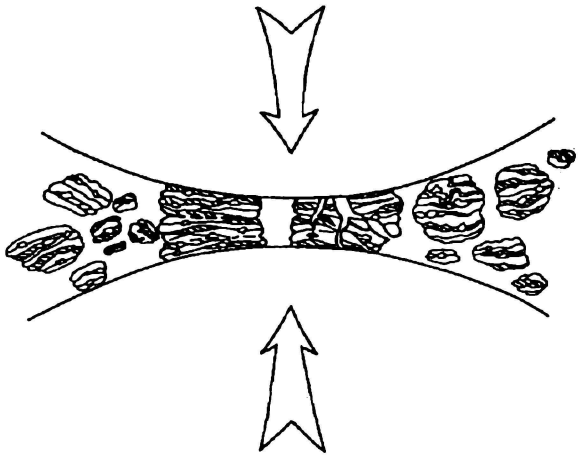

Figure 1.5 Schematic diagram showing ball-powder-ball collision [84].

Mills used for mechanical alloying typically include tumbler ball mills, attrition mills, planetary mills and vibratory mills. The tumbler ball mill is cylindrical container rotating about its axis, which makes the balls inside move and impact on the powder charge. In attrition mill, an agitator is used to stir balls and powder charge in a stationary container. The motion of the balls causes much greater surface contact than in tumbler ball mills [85]. Vibratory mills (for example, the SPEX 8000 Mixer/Mill) are commonly used as high-energy ball mills to process small amounts of powder (about 10 gram) in the laboratory. The vial containing the powder and balls vibrates in three mutually perpendicular directions. This is higher energetic compared to the motion in attrition, planetary or tumbler mills. An attritor mill and a SPEX mill are shown in Figure 1.6 [86].

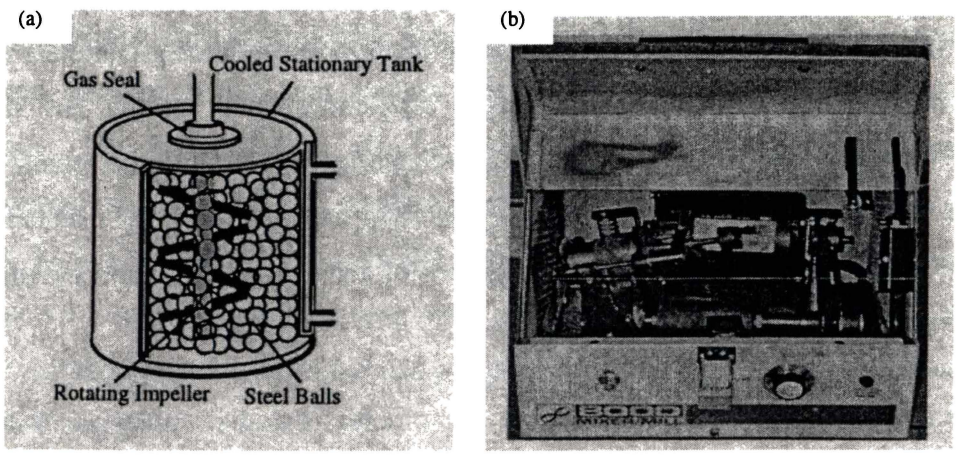

Figure 1.6 Attritor (a) and SPEX 8000 mixer/mill (b) [86].

The efficiency of milling depends on the rotation speed of the cylinder in tumbler mills, rotation speed of the shaft in attritor mills, and the vibration frequency of

the vial in vibratory mills. The mass ratio of ball/powder may also affect the milling efficiency. Normally this ratio is in the range 1 to 10 [87].

One of the major problems when producing metal-ceramic composites via powder mixing and consolidation route is agglomeration of reinforcement particles due to particle size differences between the metallic and ceramic powders. High-energy mechanical milling was introduced to prepare composite powders so each particle was a homogenous distribution of reinforcement particles in a metal matrix (Figure 1.7) [88]. After milling for long enough, the small ceramic reinforcement particles are embedded into the metal matrix and a homogenous composite powder is formed.

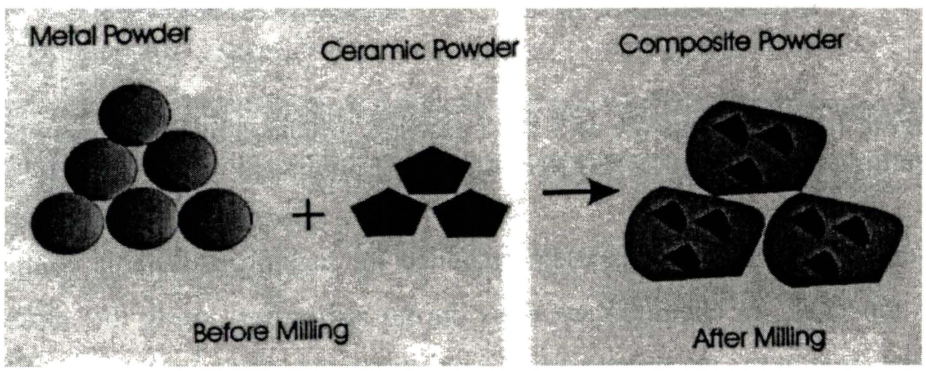

Figure 1.7 Schematic of high-energy ball milling for preparing composite powder [88].

Al/SiC composite powders with 20 vol% SiC have been produced by milling a Al/SiC powder mixture by using a planetary ball mill [89]. During 50 hours of milling, the SiC particle size decreased gradually and the SiC particles became embedded in the Al matrix to form a composite powder (Figure 1.8). The micrograph of the Al/SiC composite powders produced after milling for 50 hours clearly showed that 1μm SiC particles were homogenously distributed in the Al matrix.

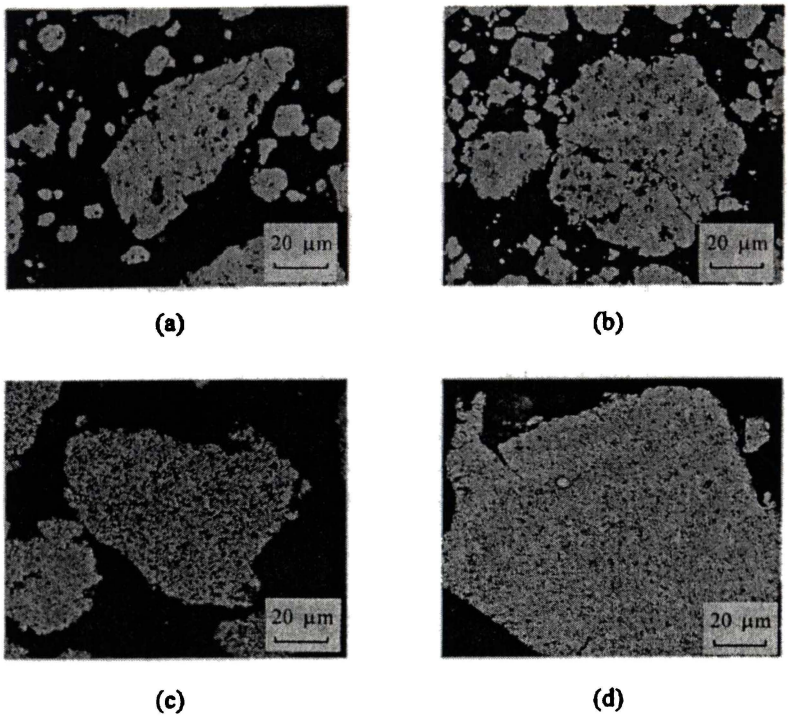

Figure 1.8 Microstructure of SiC/Al powders produced by high energy ball milling for (a) 4 hours, (B) 10 hours, (c) 31 hours and (d) 50 hours [89].

High-energy ball milling has been examined for making metastable compounds and composites via chemical reactions during milling or during the subsequent heat treatment of the as-milled powders [90-96a]. The starting temperature for the reaction between Al and TiO_2 decreases with increasing milling time [91], due to formation of the Al/TiO_2 composite particles and further refining of the composite structure. Ying et al. [94a] also obtained fine Al/TiO_2 composite particles less than 500 nm after 8 hours of milling in a SPEX mill. After heat treating the as-milled powders, a fine structure of Ti-alloy based Al_2O_3 composite particles 200 nm to 3 μm was produced.

1.3 Mechanical properties of metal ceramic composites

1.3.1 Plastic deformation and fracture behaviour

When a load is applied to a piece of metal, it deforms elastically and then plastically as the load increases. Ceramics deform elastically and fracture at the limit of their tolerance. Stress-strain curves of ceramic matrix composites do not normally show the onset of plastic yielding before fracturing. In metal matrix

composites, the transition from elastic to plastic deformation is often smooth and non-linear. The fundamental mechanisms explaining these properties differ for metal and ceramic matrices. In metallic matrices, the composites show plastic deformation under load, while ceramic matrices, only show elastic deformation with matrix cracking under loading. The fundamental mechanism explaining fracture of a ceramic matrix composite is mainly matrix cracking, while fracture of a metal matrix composite is due to plastic deformation.

The stress-strain curve of metal-ceramic composites is shown in Figure 1.9 [97]. The metal-ceramic composite material exhibits elastic and plastic deformation because of its metal content. Material strength increases when the metal is reinforced with a ceramic phase. The overall mechanical properties of metal-ceramic composites generally depend on factors such as the concentration, shape, contiguity and the distribution of the reinforcement and the metal phases. Rule of mixture is often used to estimate composite mechanical properties, using the volume fraction of each phase.

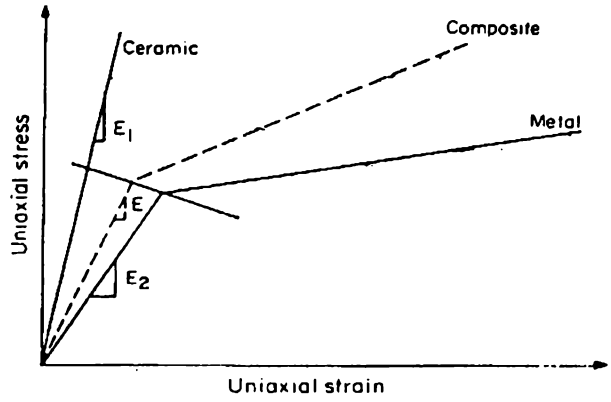

Figure 1.9 Uniaxial elastic-plastic deformation of a metal-ceramic composite [97].

1.3.2 Effect of microstructure on strength

Increasing material strength, in a broad sense, usually implies the increase in stiffness, yield stress, and fracture toughness. The basic strengthening mechanisms of metal-ceramic composites are continuing micromechanism and the movement of dislocation. There are several popular micromechanism models including: rule of mixture, Eshelby's model, and numerical models [98-100]. As mentioned before, Rule of Mixture model considers that the overall properties of

composite are contributed by the volume fraction each phase in the composite. Eshelby's model is mainly used to calculate the stress field interaction in and around an ellipsoidal inclusion, which has the same properties as those of the surrounding matrix. All these models calculate the stress field in and around a local inclusion, which has properties the same as those of surrounding infinite matrix. Numerical models calculate stress and strain at a specific location within the matrix and reinforcement.

All these models are good for defining general trends and giving detailed information about the stress and strain state at specific locations within the composites. The major shortcoming of these models is that they cannot account for the mechanical behaviours in the ceramic particulate in the composite. As an example, the strength of SiC particulate reinforced SiC/Al composite increased with volume fraction of SiC particles, and decreased with the increasing SiC particle size (Figures 1.10 and 1.11) [101].

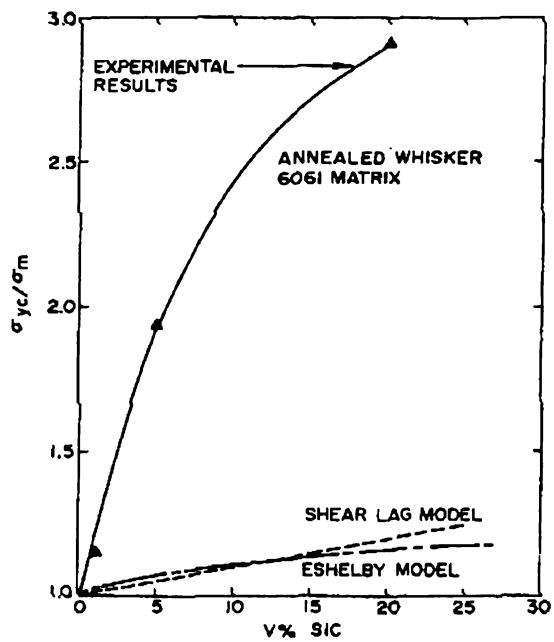

Figure 1.10 The ratio of the yield stress of the composite to that of the metal matrix vs volume fraction of a SiC short fibre [101].

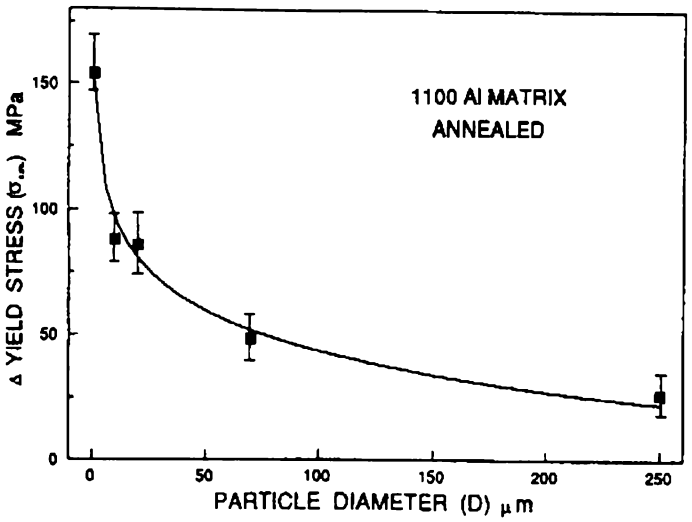

Figure 1.11 Effect of SiC particle size on yield stress [101].

To explain the effect of particle size of the particulate reinforcement on composite strength, dislocation movement mechanism was established [102-103]. This model considers that the microstructure affects composite strength. The major changes are due to the dislocations generated, which relax the thermal residual stresses caused by difference in the thermal expansion coefficients of the reinforcement and the matrix [104-106]. This theory also considers that dislocation motion is controlled either by the dislocation-dislocation interaction, dislocation-particulates interaction, or by dislocation interaction with matrix.

The dislocation mechanism model uses two parameters dislocation density and subgrain size of reinforced particles. The subgrain is a form of lower energy dislocation configuration. The model calculates the stress-strain field as a function of the number and size of dislocations, and shows that increasing the dislocation density and decreasing subgrain size increases composite strength. It also formulated a relationship between dislocation density and subgrain size of the matrix and the volume fraction and particle size of the reinforcement phase (Figure 1.12 and 1.13). For example, in Al/SiC metal matrix composite, the dislocation density increases and the subgrain size decreases with increasing of the SiC volume fraction. Dislocation density decreases and subgrain size increases with increasing SiC particle size [101].

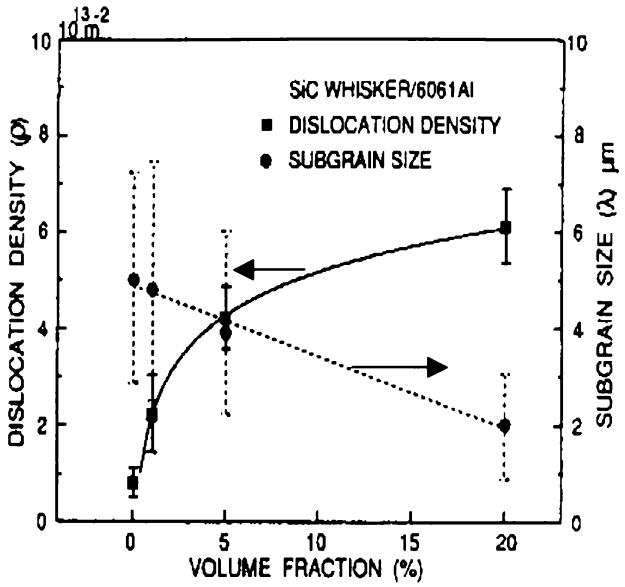

Figure 1.12 Effect on SiC volume fraction on dislocation density and subgrain size [101].

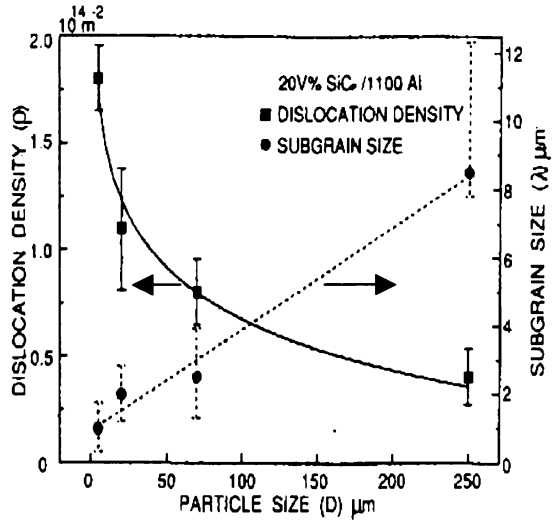

Figure 1.13 Effect on SiC particulate size on dislocation density and subgrain size [101].

1.3.3 Effect of microstructure on fracture toughness

The toughening mechanisms in ceramic matrix composites and metal matrix composites are different. For the particulate reinforced ceramic matrix composites, the brittle ceramic is often toughened by ductile metallic particulate. The following mechanisms have been suggested:

- Crack front bowing model. This model defines the critical energy release rate from a brittle matrix via crack front and the interaction between particles reinforcement and the crack propagation [107-108].
- Crack deflection model. This model focused only on the geometry of cracks being deflected by particles and ignores the effects of local stress concentrations due to the particles and thermal residual stresses [109]. Rod-shaped particles were found to be most effective in enhancing composite fracture toughness, followed by disk-shape particles, while spherical particles gave only a modest increase.
- Ductile particle bridging model. When reinforcement particles are softer than the matrix, they can undergo plastic deformation before they fail. This model considers that ductile particles bridge the upper and lower faces of the main two-dimensional crack [110].
- Residual stress toughness model. Thermal residual stress is induced during heating and cooling due to the having different thermal expansion coefficients between matrix and particles [111-112]. This thermal stress field consists of tensile and compressive stresses in equilibrium. Fracture toughness of the composite is increased by introducing this compressive stress into the composite.
- Transformation toughening. Some ceramic particles can undergo a martensitic transformation under stress and/or temperature change. Phase transformation increases composite fracture toughness because the changes in particle induce compressive stress around the reinforcement particles and matrix [113-114].

Toughening mechanism of metal matrix composites differs from that of ceramic matrix composites. Fracture toughness of composites is always less than the fracture toughness of the metal matrix. For example, the 20 vol% SiC particulate reinforced Al alloy composite has a fracture toughness of 10 $MPa \cdot m^{1/2}$ while the fracture toughness of Al alloy is about 40 $MPa \cdot m^{1/2}$ [113].

Popular mechanisms used to describe how fracture toughness of particulate reinforced metal matrix are void nucleation and growth model [115-117] and the

reinforcement fracture model [118-119]. In the void nucleation and growth model, the space between void nucleation particles and the tensile strength of the matrix are considered to influence composite fracture toughness. Fracture toughness is proportional to the square root of the average space between void nucleation particles, and average space between void nucleation particles decreases with increasing volume fraction of reinforcement. There has been supported experimentally (Figure 1.14) [101].

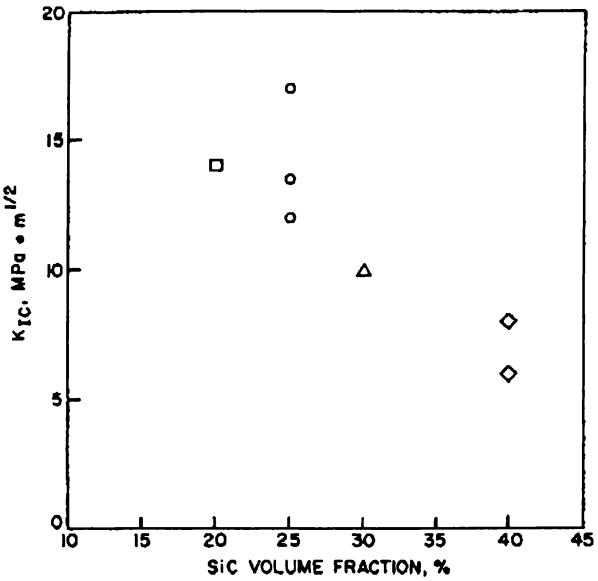

Figure 1.14 Effect of SiC volume fraction on fracture toughness Al-SiC composites [101].

Fracture toughness of Al-SiC composites decreases with increasing average particle size of SiC (Figure 1.15) [101]. The reinforcement fracture model was used to explain this effect. This model suggests that large-size particles fracture before smaller particles as applied strain increases. The reinforcement fracture model predicts that increasing the reinforcement particle size will increase the probability of particle cracking. Thus, composite fracture toughness will decrease reinforcement particle size increases.

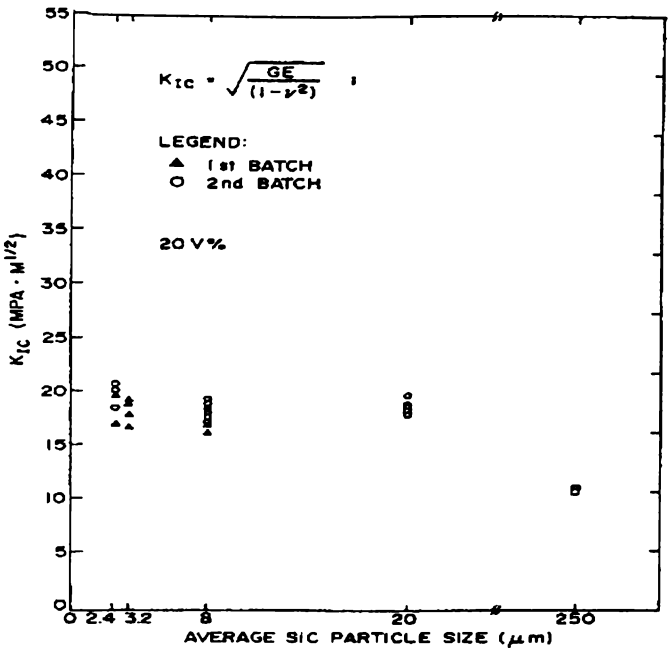

Fig. 1.15 Effect of SiC particle size on fracture toughness of Al- 20 vol.% SiC composite [101].

1.3.4 Effect of the metal-ceramic interface on mechanical properties

The properties of the metal-ceramic interface play a key role in the mechanical properties of composite materials. There have been many studies on the formation of metal-ceramic interfaces [120-123]. The strength of the interface bond and chemical properties can strongly affect overall mechanical properties [124-130].

Chemical reactions at metal-ceramic interfaces, generally the reaction products, decrease composites strength [131-134]. Several discrete phases such as Ti_5Si_3, Ti_2AlC and Ti_3AlC were found at interface of the Ti-14Al-21Nb/SiC composite [134]. These reaction products decreased composite fracture toughness. Heat-treated Ti/Al_2O_3 composite at low temperatures produce weakly bonded interfaces between Ti and Al_2O_3 [135]. This interface decreases composite strength. Heating the composite at high temperatures (1000°C and above) created a strongly bonded Ti_3Al intermetallic layer due to the reaction between Ti and Al_2O_3. As a result, fracture toughness of the Ti/Al_2O_3 composite decreased, but strength increased.

Fracture mechanisms at metal ceramic interfaces include ductile void growth in metal adjacent to the interface, brittle debonding, and micro-crack coalescence

(Figure 1.16). Good interface bonding increases composites strength but decreases fracture toughness. This can be controlled by the releasing of fracture energy [136]. Fracture energy releases differently at different interface phases, increasing in the order amorphous oxides, crystalline oxides and intermetallic compounds. All these mechanisms indicate that morphological adaptation of the contact surface, bond formation and controlling residual stresses at the interfaces need to be considered to achieve good mechanical properties of metal-ceramic interface.

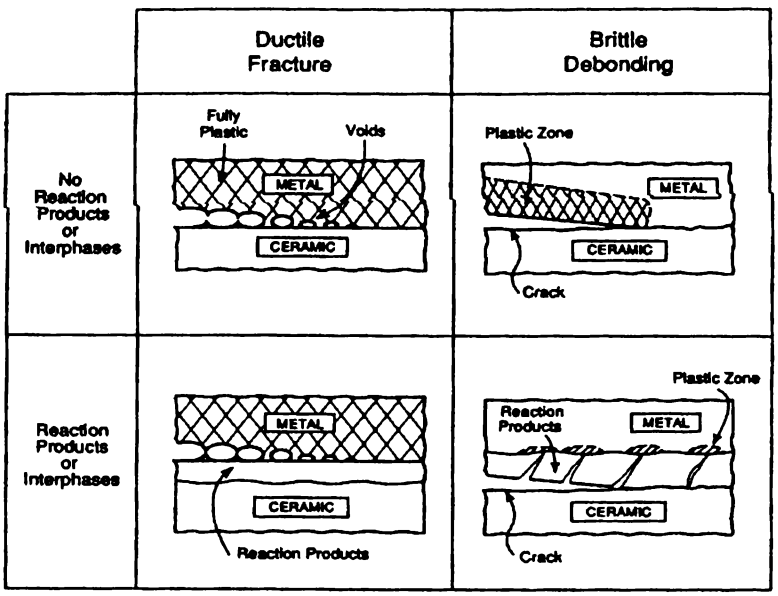

Figure 1.16 Various fracture mechanisms that occur at metal-ceramic interfaces [136].

1.4 Objective of the thesis

The microstructure of metal-ceramic composites strongly affects their mechanical properties. To achieve good mechanical properties, a clear understanding of the microstructure-mechanical properties relationship needs to be achieved. To achieve desirable microstructures, processing conditions-microstructure relationships must also be established. These relationships are not yet known for new materials such as Ti_xAl_y/Al_2O_3 and $Al_2Ti_4C_2/Ti_xAl_y/Al_2O_3/TiC$ composites. To establish the processing-microstructure-property relationships of a wide range of new Ti_xAl_y/Al_2O_3 and $Al_2Ti_4C_2/Ti_xAl_y/Al_2O_3/TiC$ based composites produced from Al, TiO_2 and carbon. In particular, this study investigates the effect of processing conditions on composites phase formation and microstructure such as porosity level and Al_2O_3 particles size and the effects of this microstructure on composites hardness, bending strength and fracture toughness.

References

1. P. Rohatgi, Cast metal-matrix composites, Metal Handbook, ninth edition, 840-854, (1996) ASM International, P.C.
2. Maity, P.N. Chakraboty, S.C. Panigrahi, Journal of Materials Processing Technology, **53**, 857-870, (1995).
3. B.F. Quigley, G.J. Abbaschian, R. Wunderlin, and R. Mehrabian, Metallurgical Transactions A, **13A**, 93-100, (1982).
4. M.A.H. Howes, Journal of Metals, March, 28-34, (1986).
5. J. Singh, S.K. Goel, V.N.S. Mathur, M.L. Kapoor, J. Mater. Sci., **26**, 2750-2758, (1991).
6. D.G. Gelderloos, K.R. Krasek, J. Mater. Sci., **3**, 232-238, (1984).
7. H.X. Peng, D.Z. Wang, L. Geng, C.K. Yao, Scripta Materialia, **37**, 199-204, (1997).
8. I.A. Ibrahim, F.A. Mohamed, E.J. Lavernia, J. Mater. Sci., **26**, 1137-1156, (1991).
9. S.P. Gaus, M.P. Harmer, H.M. Chan, H.S. Caram, J. Am. Ceram. Soc., **82**, 897-908, (1999).
10. S.P. Gaus, P.M. Sheedy, H.S. Caram, H.M. Chan, M.P. Harmer, , J. Am. Ceram. Soc., **82**, 909-915, (1999).
11. M.S. Newkirk, A.W. Urquhart, H.R. Zwicker, J. Mater. Res., **1**, 81-89, (1986).
12. S. Antolin, A.S. Nagelberg, D.K. Creber, J. Am. Ceram. Soc., **75**, 447-454, (1992).
13. S. Antolin, A.S. Nagelberg, A.W. Urquhart, J. Am. Ceram. Soc., **75**, 455-462, (1992).
14. M.K. Aghajanian, M.A. Rocazella, J.T. Burke, S.D. Keck, J. Mater. Sci., **26**, 447-454, (1991).
15. I.A. Ibrahim, F.A. Mohamed, E.J. Lavernia, J. Mater. Sci., **26**, 1137-1156, (1991).
16. W.B. Hillig, American Ceramic Society Bulletin, **73**, 56-62, 1994.
17. 17.B.D. Flinn, F.W. Zok, F.F. Lange and A.G. Evans, Materials Science and Engineering, **A144**, 153-157, (1991).
18. X.F. Yang and X.M. Xi, J. Mater. Res., **10**, 2415-2417, (1995).
19. R.E. Loehman, K. Ewsuk, A.P. Tomisa, J. Am. Ceram. Soc., **79**, 27-32, (1996).
20. Y. Gao, J. Jia, J. Mater. Res., **10**, 1216-1225, (1995).
21. E. Saiz, A.P. Tomsia, J. Am. Ceram. Soc., **81**, 2381-93, (1998).
22. S. Wu, A. J. Gesing, N.A. Travitzky, N. Claussen, J. Euro. Ceram. Soc., **7**, 277-281, (1991).
23. X.M. Xi , X.F. Yang, J. Am. Ceram. Soc., **79**, 102-108, (1996).
24. E.J. Gonzalez, K.P. Trumble, J. Am. Ceram. Soc., **79**, 114-120, (1996).
25. S. Krishnamurthy, Y.W. Kim, G. Das, F.H. Froes in "Metal-ceramic matrix composites: Processing, modeling and mechanical behavior," Ed. by R.B. Bhagat, A.H. Claver, P. Kumar and A.M. Ritter, The Minerals, Metals/Materials Society, Warrendale, PA, P. 145, (1990).
26. H.J. Rack, in "Processing and Properties of Powder Metallurgy Composites," Ed. by P. Kumar, K. Vedula, and A. Ritter, The Metallurgical Society, Warrendale, PA, P. 155, (1988).

27. W.H. Tuan, W.B. Chou, J. Am. Ceram. Soc., **80**, 2418-2420, (1997).
28. M.K. Srivasrava, R.K. Mandal, S. Mohan, J.P. Pathak, and S.N. Ojha, Indian Journal of Engineering and Materials Sciences. **5**, 234-239, (1997).
29. C-I. Fun, M. Rahaman, J. Am. Ceram. Soc., **75**, 2056-2065, (1992).
30. O. Sudre, F.F. Lange, J. Am. Ceram. Soc., **75**, 519-524, (1992).
31. A. Kawasaki, J.F. Li, R. Watanabe, T. Matsubara, in 3th Int. Symp. on 'Structural and functional gradient materials', 433-439, (ed. B. Ilschner and N. Cherradi) Lausanne, Switzerland, (1994).
32. M. Takemura, A. Yoshitake, H. Hayakawa, T. Hyakubu, M. Tamura, in Proc. of 1th Int. Symp. On 'Functional Gradient Materials' 97-100, Japan, (1990), Ed. M. Yamanouchi et al.
33. R.Z. Yuan, L.M. Zhang, Q.J. Zhang, X.F. Tang, J. Mater. Synth. Process. **1**, 171-179, (1993).
34. L.M. Zhang, R.Z. Yuan, M. Omori, T. Hirai, in 3th Int. Symp. on 'Structural and Functional Gradient Materials', 59-64, Lausanne, Switzerland, Ed. B. Ilschner and N. Cherradi, (1994).
35. V.M. Kostylev, V.G. Nabatov, Inzhenerno-Fizicheskii Zhurnal, (English translation) **9**, 377-383, (1965).
36. V.I. Ermakov, A.G. Strunina, V.V. Barzykin, Combustion, Explosion, and Shock Wave (English translation), **14,** 36-44, (1978).
37. M.A. Korchagin, V.A. Podrgin, Combustion, Explosion, and Shock Wave (English translation), **15**, 48-53, 1979.
38. C.R. Bowen, B. Derby, Acta metall. Mater. **43**, 3903-3913, (1995).
39. A.G. Merzhanov, Self-propagating high-temperature synthesis: Twenty years of search and findings, In Combustion and Plasma Synthesis of High-Temperature Materials. Ed. Z.A. Munir and J.B. Holt, VCH Publishers, Inc., 32-40, (1990).
40. K.A. Philpot, Z.A. Munir, J.B. Holt, Journal of Materials Science, **22**, 159-169, (1987).
41. A.A. Shidlovskii, V.V. Gorbunov, Combustion, Explosion, and Shock Wave (English translation), **18**, 40-42, 1981.
42. J.F. Powell, G.M. Janowski, In Situ Reactions for Synthesis of Composites, Ceramics, and Intermetallics, Ed. by E.V. Barrera, S.G. Fishman, F.D.S. Marquis, N.N. Thadhani, W.E. Frazier, Z.A. Munir, The Minerals, Metals & Materials Society, 129-140, (1995).
43. Z.A. Munir, U. Anselmi-Tamburini, Materials Science Reports **3**, 277-365, 1989.
44. A. Saidi, A. Chrysanthou, J.V. Wood, J.L.F. Kellie, J. Mater. Sci., **29**, 4993-4998, (1984).
45. A.N. Tabachenko, T.A. Panteleeva, V.I. Itin, Combustion, Explosion, and Shock Wave (English translation), **20**, 387-384, (1984).
46. Y. Miyamoto, K. Hirao, M. Koizumi, in: Proceedings of International Symposium on Fundamental Research Strategy in Development of New Materials for Efficient Energy Conversion, Osaka, 134-141, (1987).
47. L.L. Wang, Z.A. Munir, Y.M. Maximov, J. Mater. Sci., **28**, 3693-3708, (1993).

48. D.E. Garcia, S. Schicker, J. Bruhn, R. Janssen, N. Claussen, J. Am. Ceram. Soc., **80**, 2248-2252, (1997).
49. D. Belitskus, Journal of Metals, **7**, 39-44, (1973).
50. A.O. Kunrath, T.R. Strohaecker, J.J. Moore, Scripta Materialia, **34**, 175-181, (1996).
51. A.O. Kunrath, T.R. Strohaecker, J.J. Moore, Scripta Materialia, **34**, 183-188, (1996).
52. F.H. Perfect, Transactions of the Metallurgical Society of AIME, **239**, 1282-1286, (1967).
53. A.G. Strunina, V.I. Ermakov, and E.A. Averson, Combustion, Explosion, and Shock Wave (English translation), **15**, 77-84, (1979).
54. A.O. Kunrath, T.R. Strohaecker, J.J. Moore, Scripta Materialia, **34**, 189-194, (1996).
55. K.G. Ewsuk, S.J. Glass, R.E. Loehman, A.P. Tomsia, W.G. Fathenholtz, Metallurgical and Materials Transactions A, **27A**, 2122-2129, (1996).
56. R. Abramovici, Materials Science and Engineering, **71**, 313-320, (1985).
57. C.F. Feng, L. Froyen, Scripta Materialia, **39**, 109-118, (1998).
58. Y. Choi, S.W. Rhee, J. Mater. Res., **9**, 1761-1766, (1994).
59. E.V. Chernenko, L.F. Afanaseva, V.A. Lebedeva, V.I. Rozenband, Combustion, Explosion, and Shock Wave (English translation), **24**, 3-11, (1987).
60. A.G. Strunina, V.I. Ermakov, V.V. Barzykin, Combustion, Explosion, and Shock Wave (English translation), **12**, 211-217, (1976).
61. S.V. Kostin, A.G. Strunina, V.V. Barzykin, Combustion, Explosion, and Shock Wave (English translation), **18**, 32-38, (1981).
62. N. Claussen, D.E. Garcia, R. Janssen, J. Mater. Res. **11**, 2884-2888, (1996).
63. P. Matteazzi, G.L. Caer, J. Am. Ceram. Soc., **75**, [10], 2749-2755, (1992).
64. S.P. Gaus, M.P. Haemer, H.M. Chan, H.S. Caram, N. Claussen, J. Am. Ceram. Soc., **83**, 1599-1605, (2000).
65. S.P. Gaus, M.P. Haemer, H.M. Chan, H.S. Caram, J. Bruhn, N. Claussen, J. Am. Ceram. Soc., **83**, 1606-1612, (2000).
66. D.E. Garcia, S. Schicker, J. Bruhn, N. Claussen, J. Am. Ceram. Soc., **81**, 429-432, (1998).
67. T. Klassen, R. Gunther, B. Dickau, A. Bartels, R. Bormann, H. Mecking, J. Am. Ceram. Soc., **81**, 2504-2506, (1998).
68. S. Schicker, D.E. Garcia, J. Bruhn, R. Janssen, N. Claussen, J. Am. Ceram. Soc., **80**, 2294-2300, (1997).
69. D.E. Garcia, S. Schicker, J. Bruhn, R. Janssen, N. Claussen, J. Am. Ceram. Soc., **80**, 2248-2252, (1997).
70. C. Scheu, G. Dehm, W.D. Kaplan, D.E. Garcia, N. Claussen, J. Am. Ceram. Soc., **83**, 397-402, (2000).
71. D.E. Garcia, S. Schicker, J. Bruhn, R. Janssen, N. Claussen, The American Ceramic Society, **54**, 219-230, (1996).
72. J.S. Benjamin, Metall. Trans. **1** 2943-51, (1970).
73. C.C. Koch, Materials Transactions, JIM. **36**, 85-95, (1995).

74. R.M. Davis, B. McDermott, C.C. Koch, Metallurgical Transactions A, **19A**, 2867-2874, (1988).
75. Zhenguo Yang, Ruiming Ren, Leon L. Shaw, J. Am. Cream. Soc., **83**, 1897-904, (2000).
76. Z.G. Li, D.J. Smith, Appl. Phys. Lett. **55**, 919-921, (1989).
77. H. Gleiter, Nanocrystalline materials, Prog. Mater. Sci. **33** 233-268, (1990).
78. R.O. Hughes, S.D. Simth, C.S. Pande, H.R. Johnson, R.W. Armstrong, Scripta Metall. **20,** 93-99, (1986).
79. L.E. McCandlish, B.H. Kear, B.K. Kim, Nanostructured Materials, **1**, 119-124, (1992).
80. L.L. Ye, M.X. Quan, Nanostructured materials, **5**, 25-31, (1995).
81. Zhen-Guo Yang, L.L. Shaw, Nanostructured materials **7**, 873-886, (1996).
82. N.J. Welham, D.J. Lewellyn, J. Euro. Ceram. Soc., **19**, 2833-2841, (1999).
83. J.C. Kim, B.H. Ko, I.H. Moon, Nanostructured materials **7**, 877-903, (1996).
84. P.S. Gilman, J.S. Benjamin, Annu. Rev. Mater. Sci. **13**, 279-300, (1983).
85. C.C. Koch, J.D. Whittenberger, Intermetallics **4**, 339-355, (1996).
86. Wei Wang, PhD Thesis, 12-13, University of Waikato, (2000).
87. C.C. Koch, Annu. Rev. Mater. Sci. **19**, 121-143, (1989).
88. D.L. Zhang, Prog. In Mat. Science, in press.
89. L. Lu, M.O. Lai, Mechanical Alloying, Kluwor Academic Publishers, 118-123, (1998)
90. N.J. Welham, P.E. Willis, T. Kerr, J. Am. Ceram. Soc., **82**, 2332-2336, (1999).
91. N.J. Welham, Materials Science and Engineering, **A255**, 81-89, (1998).
92. N.J. Welham, Journal of Alloys and Compounds, **270**, 228-236, (1998).
93. Y. Chen, T. Hwang, M. Maesh, J.S. Williams, Metallurical and Materials Transcations A, **28A,** 1115, (1997)
94. D.L. Zhang, M. Newby, US patent, US6,264,719 B1, Jul, 24, 2001.

94a. D.Y. Ying, D.L. Zhang, M. Newby, Metallurgical and Materials Transaction, in press.

95. N.J. Welham, Intermetallics, **6**, 363-368, (1998).
96. C.F. Feng, L.Froyen, Composites: Part A, **31**, 385-390, (2000).

96a. D.L. Zhang, D.Y. Ying, G. Adam, Mat. Sci. Forum, 287-292, (2002).

97. S. Suresh, A. Mortensen, International Materials Reviews, **42**, 85-90, (1997).
98. R.K. Everett, R.J. Arsenault, Metal Matrix Composites: Mechanisms and Properties, Academic Press, London, 123-127, (1991).
99. M. Taya, R.J. Arsenault, Metal Matrix Composites: Thermomechanical Behaviour, Pergamon Press, Oxford, London, 314-319, (1991).
100. D. Eshelby, Proc. R. Soc. **A241**, 376-381, (1957).
101. R.J. Arsenault, S. Fishman, M. Taya, Progress in Materials Science, **38**, 1-157, (1994).
102. N. Hansen, Acta Metall., **25**, 863-871, (1997).
103. R.J. Arsenault, N. Shi, Mater. Sci. Eng. **81**, 175-181, (1986).
104. R.J. Arsenault, R.M. Fisher, Scr. Metall. **17**, 67-74, (1983).
105. M.F. Ashby, Phil. Mas. **21**, 399-407, (1970).
106. M. Vogelsang, R.J. Arsenault, R.M. Fisher, Metall. Trans., **17A**, 379-383, (1980).

107.B.D. Flinn, M. Rohle, A.G. Evans, Acta Metall. **37**, 3001-3006, (1989).

108.F.F. Lang, Phil. Mag. **22**, 983-996, (1970).

109.A.G. Evens, Phil. Mag. **26**, 1327-1330, (1972).

110.K.T. Fabers, A.G. Evens, Acta Metall., **31**, 565-571, (1983).

111.B.Budiansky, J.C. Amazigo, A.G. Evens, J. Mech. Phys. Solids, **36**, 167-174, (1988).

112.G.C Wei, P.F. Becher, J.Am. Ceram. Soc. **67**, 571-576, (1984).

113.C.H. McMurtry, W.D.G. Boecker, S.G. Seshadri, J.S. Zanghi, J.E. Garnier, Am. Ceram. Soc. Bull., **66**, 325-330, (1987).

114.L.R.F. Ross, J. Mech. Phys. Solids, **35**, 383-389, (1987).

115.A.V. Virkar, D.L. Johson, J.Am. Ceram. Soc. **60**, 513-521, (1977).

116.G.G. Garret, J.F. Knott, Metall. Trans. **9A**, 1187-1195, (1978).

117.G.LeRoy, J.D. Embury, G. Edwards, M.F. Ashby, Acta Metall. **29**, 1509-1517, (1981).

118.D.L. Davidson, Metall. Trans. **18A**, 2115-2119, (1987).

119.G.T. Hahn, Metall. Trans., **15A**, 947-955, (1984).

120.Y. Flom, R.J. Arsenault, Acta Metall. **37**, 2413-2423, (1989).

121.M. Humenik, W.D. Kingery, J. Am. Ceram. Soc., **37**, 18-23, (1954).

122.N. Eustathopoulos, Acta Mater., **46**, 2319-2327, (1998).

123.M. Rohle, A.G. Evans, Materials Science and Engineering, **A107**, 187-197, (1989).

124.J.M. Howe, International Materials Reviews, **38**, 233-256, (1993).

125.A.G. Balogh, M.P. Macht, V. Naundorf, J. Mater. Res., **9**, 406-409, (1994).

126. H. Jang, D.N. Seidman, Scr. Metall., **26**, 1493-1498, (1992).

127.Y. Yoshino, T. Shibata, J. Am. Cream. Soc., **75**, 2756-2760, (1992).

128.M. Wagner, T.Wanger, D.L. Carroll, J. Marien, D.A. Bonnell, M. Rohle, MRS Bulletin, **8**, 42-48, (1997).

129.K. Burger, W. Mader, M. Rohle, Ultramicroscopy, **22**, 1-14, (1987).

130.Y. Ishida, J.Y. Wang, T. Suga, ISIJ International, **30**, 1041-1045, (1990).

131.B. Derby, C.D. Qin, Acta Metall. Mater., **40**, Suppl. 53-58, (1992).

132. J.A. Yeomans, T.F. Page, J. Mater. Sci., **25**, 2312-2320, (1990).

133.S. Zhang, Materials Science and Engineering, **A163**, 141-148, (1993).

134. E.L. Hall, A.M. Ritter, J. Mater. Res., **8**, 1158-1168, (1993).

135.J.C. Yang, Y.C. Lu, S.L. Sass, Materials Science and Engineering, **A162**, 97-106, (1993).

136.A.G. Evans and B.J. Dalgleish, Acta Metal. Mater., **40**, 295-304, (1992).

Chapter Two
Experimental Techniques

2.1 Introduction

This chapter describes the powders used, experimental setup, sample preparation processes investigated, material characterization method, and mechanical testing techniques used in this study.

2.2 Powders used

Commercially available powders were used (Table 2.1).

Table 2.1 Powders used in the study

Powder	Purity	Particle Size	Manufacturer
Aluminum Powder	99.5%	- 80 μm	Alfa
Rutile (TiO_2)	99%	- 80 μm	Millennium Chemicals
Graphite Powder (C)	99.5%	- 80 μm	CERAC

2.3 Powder milling

For the milling experiments, the required proportions of powders for milling 8 grams were weighed and then placed in a stainless steel vial, 50 mm in diameter and 80 mm long. Then about 0.5 g of ethanol was added as a process control agent. Four 12.5 mm diameter stainless steel balls were also added to the vial, give a ball to powder weight ratio of 4:1. The vial was subsequently sealed in a gove-box filled with argon gas.

The SPEX 8000 Mixer/Mill (CertiPrep) was used as a high-energy ball mill to produce the composite powders. The powders were mechanically milled for four hours. After milling, the as-milled powder was left overnight at 90°C to evaporate the ethanol.

2.4 Thermal treatment and consolidating the powder

To study the reaction between TiO_2 and C, the TiO_2/C composite powder produced using mechanical milling was heated to temperatures in the range 1400°C to 1600°C for 5 hours under flowing argon. The Al/TiO_2, Al/Ti_2O_3, and Al/TiO_nC_{1-n} composite powders were pressed into bars at 30 MPa using a uniaxial die-press, and then pressed again at 200 MPa using a Stansted FPG2347 cold isostatic press. The samples were loaded in Al_2O_3 boats and placed in a Ceramic Engineering HT05/18 tube furnace with a Eurothem 902 programmable controller. Samples were sintered at different temperatures in the range 1300-1650°C for 1 hour. The typical heating and cooling rates were 3°C/min. The furnace atmosphere was controlled by flowing argon at a flowing rate of 20 mL/min.

Some of the pressure-less sintered samples were further densified by hot isostatic pressing at 1300°C for 2 hours at 200 MPa. Two sets of samples were prepared. One set of samples was hipped without canning, and the other set were hipped after being sealed in a Ti tube. The heating rate during hipping was 3°C/min. When the temperature reached 1300°C, the pressure inside the furnace was gradually increased to 200 MPa.

2.5 Density

Density is defined by the mass of material per unit volume. The standard Archimedes method was used to measure bulk density. Sample volume was calculated using the difference between sample weight measured in air (W_{air}) and the weight when the sample was suspended in water (W_{water}). The sample's bulk density, ρ, is given by:

$$\rho = \frac{W_{air}}{W_{air} - W_{water}} \quad (2\text{-}1)$$

The theoretical density of a material corresponds to material without any defects. By definition, a single unit cell is used to calculate the theoretical density. The relative density can be determined by comparing the measured density with the theoretical density,

2.6 Microstructure examination

After consolidation, samples were first ground using SiC paper (Struers) of grit #320, #1000, and then #2000. After grinding, samples were polished for 15 minutes with Leco 1 micron diamond synthetic polishing media.

Scanning electron microscopy (SEM) and energy disperse X-ray (EDX) spectrometry analyses were performed using a Hitachi S4000 SEM system equipped with a Kevex EDX micro-analyzer. The SEM images were taken using back-scatter setting at 20 KV voltage.

2.7 XRD analyses

Phases in the samples were determined using X-ray diffraction. X-ray analysis was performed on powders or the polished surfaces of consolidated samples using a Philips X'Pert X-ray diffratometer with a current of 15 mA and a voltage of 45 KV and CuK_{α} radiation. The XRD patterns were obtained using a 0.02 degree pre second scan rate.

2.8 Hardness and fracture toughness measurement

The Vickers hardness testing technique was used to measure sample hardness. A square-base diamond pyramid indenter with a 136° angle between opposite faces was used. Hardness was expressed as Vickers hardness number (VHN), which is defined as the load divided by the surface area of the indentation (equation 2-2).

$$VHN = \frac{2P\sin(\theta/2)}{L^2} \qquad 2\text{-}2$$

Where P = applied load in kg;

L = average length of diagonals in mm;

θ = angle between opposite faces of diamond (typically 136°).

The hardness test was performed on the polished surfaces of the sample using a Zwick 3212 B Hardness Tester. The typical impact velocity was 0.3 mm/s with 10 kg load. The mean of three indentations was calculated. After indentation,

samples were examined using SEM to measure the length of diagonals in the indents.

To determine fracture toughness, the crack length (Figure 2.1), after indentation was measured using SEM. The mean of duplicate test was calculated and used in equation 2-3 to calculate fracture toughness.

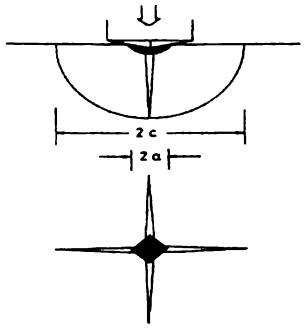

Figure 2.1 Indent deformation fracture pattern for the Vickers indenter [2].

$$K_C = 0.016(\frac{E}{H})^{1/2}(\frac{P}{C^{3/2}}) \quad (2\text{-}3)$$

Where C is penny-like radial/median crack length and α is the half length of the diagonal line of the indent, E is the Young's modulus of the material, H is the Vickers hardness, P is the load in Newtons, and C is median crack length in mm.

2.9 Bending strength

Flexure testing was performed using an Instron 4204 universal tester with an IEEE-488 interface. A strain gauge was used to measure beam deflection. All tests were run at 0.2 mm/min. The test was done in duplicate on identical bars 20-mm long, 5-mm wide and 3-mm thick.

The maximum tensile stress, σ_{max}, is determined for the 3-point loading from the equation [3]:

$$\sigma_{max} = \frac{3PL}{2bh^2} \quad (2\text{-}4)$$

Where P is the maximum load in Newton, L is the length, b is the width of specimen, and h is the thickness (in mm).

2.10 Thermal analyses

Differential thermal analysis (DTA) and thermal gravity analysis (TGA) were performed in a TA Instruments SDT 2960 differential thermal analyzer. Samples were heated a 20°C/min from room temperature to 1400°C. The atmosphere of the furnace was argon flowing at 20ml/min.

2.11 Image analyses

The area of each particle was calculated from black and white binary colour SEM images using Scion Image Bate 3b software. The particle size calculated from the model assumes a round particle cross-section. The average particle size was calculated so composites produced under different processing conditions could be compared.

References

1. R.B. Pipes, R.A. Blake, J.W. Gillespie, L.A. Carlsson, Test Methods, Technomic Publish Inc. 24-25, (1990).
2. G.R. Anstis, P.Chantikul, B.R. Lawn, and D.B. Marshall, J. Am. Ceram. Soc. **64**, 533-538, (1981).
3. G.E. Dieter, Mechanical Metallurgy, McGraw-Hill Book Co. Singapore, P. 331, (1988).

Chapter Three
Solid State Reactions between TiO_2 and C and between Ti_2O_3 or TiO_nC_{1-n} and Al

3.1 Solid state reactions between TiO_2 and C

3.1.1. Introduction

Carbon is commonly used in metallurgical industry to reduce metal oxides to metals. This study investigated solid state reactions between carbon and TiO_2 by heating TiO_2/C composite powders prepared using high energy ball milling. Refined conditions were used to obtain titanium sub-oxides and carbide such as Ti_2O_3 and TiO_nC_{1-n}. The Ti_2O_3 and TiO_nC_{1-n} were then used to fabricate titanium-based metal-ceramic and ceramic-ceramic composites.

Different proportions of rutile (99% purity) and graphite powder (99% purity) were weighed according to the following nominal reactions. Samples with compositions corresponding to four equations were called powder C1, C2, C3, and C4 respectively. It was not possible to reduce TiO_2 to Ti_2O and Ti as implicated in equation 3-3 and 3-4. This is not surprising because the reaction 3-3 is not thermodynamically favorable [1, 2]. These reactions only show the starting ratio of carbon and TiO_2.

$$2TiO_2 + C \rightarrow CO + Ti_2O_3 \qquad 3\text{-}1$$

$$TiO_2 + C \rightarrow CO + TiO \qquad 3\text{-}2$$

$$2TiO_2 + 3C \rightarrow 3CO + Ti_2O \qquad 3\text{-}3$$

$$TiO_2 + 2C \rightarrow 2CO + Ti \qquad 3\text{-}4$$

3.1.2 Reaction kinetics and phase formation

The XRD patterns of the starting rutile and graphite powders and the as-milled TiO_2/C composite powder C1. Indicated that the carbon and TiO_2 did not react to any significant degree during the milling stage (Figure 3.1). The carbon crystals must have broken into nanometer-sized grains as a clear carbon peaks did not

appear in the XRD as-milled composite powder. Similar results were also obtained for powders C2, C3 and C4 not shown.

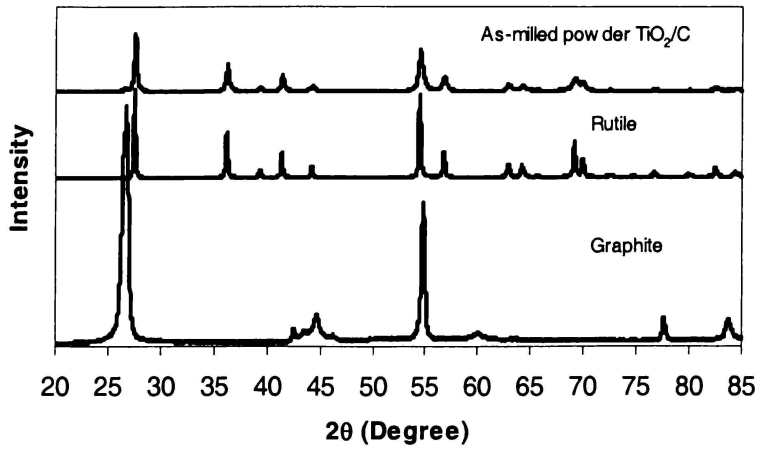

Figure 3.1 XRD patterns of raw materials and composite C1 after high energy ball milling.

The SEM micrographs of cross-sections of as-milled C1 and C4 powders after 4 hours of milling in the SPEX mill are shown in Figure 3.2. The bright phase is TiO_2 and the dark phase is carbon. Both powders consisted of powder particles with a sub-micron composite structure. The average TiO_2 particle sizes of C1 and C4 powders after 4 hours milling powder C1 were 0.5 μm and 0.3 μm respectively. The fine composite structure increased the reaction rate between carbon and TiO_2, as shown in TGA analyses results.

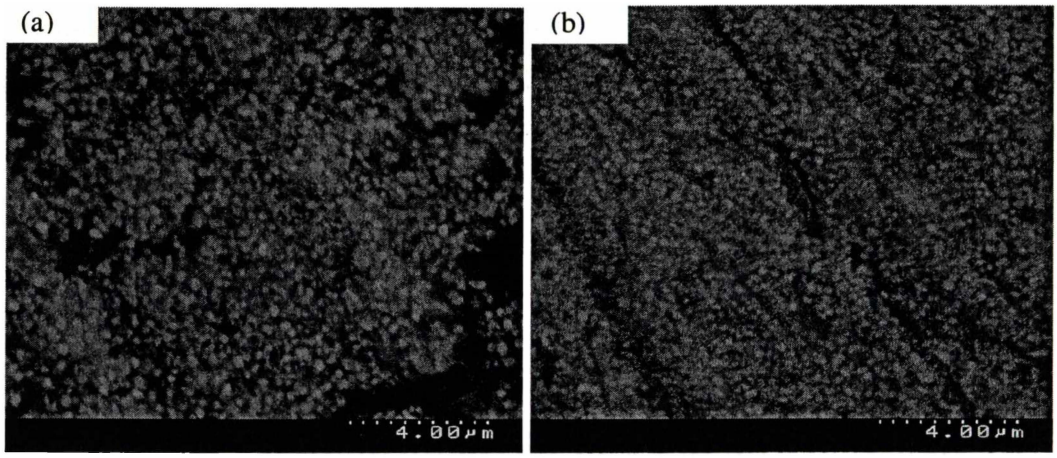

Figure 3.2 SEM micrograph of as-milled powder C1 (a) and C4 (b) after 4 hours milling.

There is no exothermic reaction peak when the powders were heated to 1400°C (Figure 3.3 and 3.4). The TGA traces show that mass decreased sharply when the temperature was above 1100°C, which indicated that carbon started to reduce

TiO_2 above 1100°C. The TGA traces indicated that with greater the carbon in the powder, the greater the rate of weight loss above 1100°C. When heated from1100°C to 1400°C, powder C4 lost about 25% of its mass, C3 powder lost about 16%, and C1 and C2 powders both lost about 11%. In summary, increasing the TiO_2/C ratio in the initial C/TiO_2 composite powder caused a higher reaction rate when the temperature was above 1100°C.

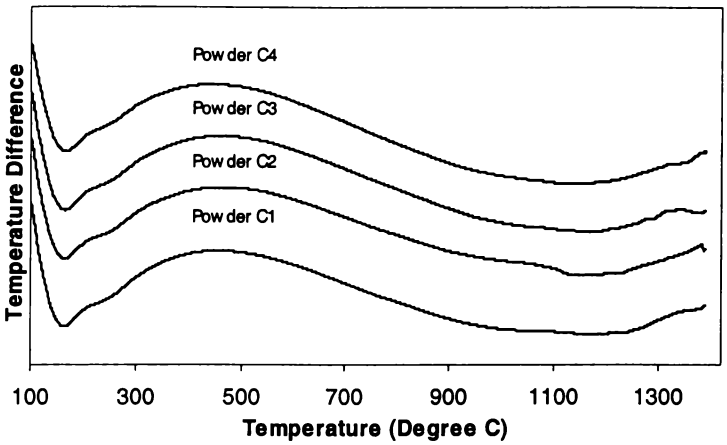

Figure 3.3 DTA traces of powders C1, C2, C3 and C4 during heating.

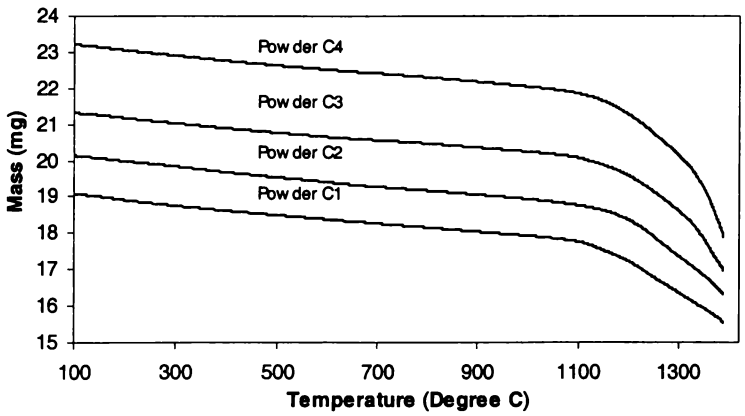

Figure 3.4 TGA traces of powders C1, C2, C3 and C4 during heating.

When powder C1 was heat treated at 1400°C, the TiO_2 peaks in the XRD pattern disappeared indicated that all the TiO_2 was consumed during this heat treatment Figure 3.5 and Ti_2O_3 was formed. Some free carbon still remained in the powder after the reaction. When the temperature was increased to 1500°C or 1600°C, all the carbon reacted as all the free carbon peaks disappeared. The major phase was Ti_2O_3 and the minor phase was TiO_nC_{1-n}. The data show that carbon can reduce TiO_2 to Ti_2O_3 above 1400°C. The Ti_2O_3 phase is stable over the temperature range 1400°C to 1600°C.

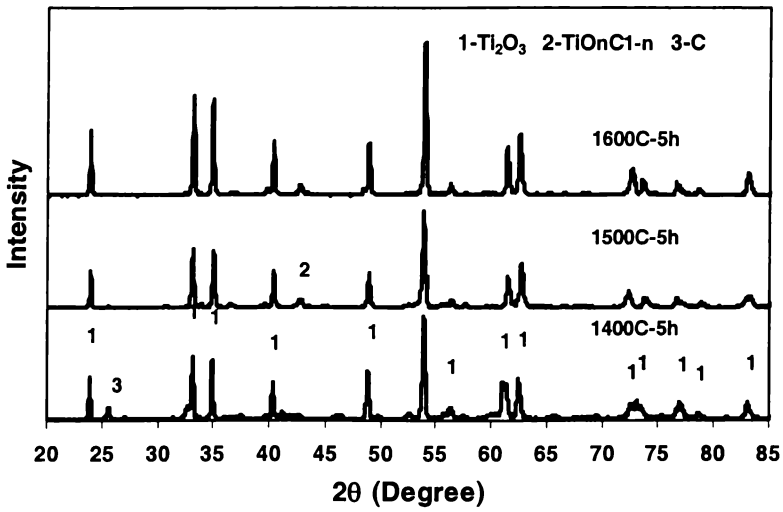

Figure 3.5 The XRD patterns of powder C1 after being heat treated at different temperatures.

Powder C2 had a cubic structure after heat treatment, (indexed as '2' in Figure 3.6). This phase can be attributed to both the TiO and TiC phases, because these compound have very similar crystal structures and lattice parameters, which the XRD technique cannot differentiate. As which TiC and TiO can form solid solutions, they may not be present as separate phases. Therefore, this phase has been denoted as TiO_nC_{1-n} ($n<1$). The reaction between the heat-treated powders with aluminum used to indicate the value of n. When the temperature was increased to 1500°C, the amount of TiO_nC_{1-n} increased (Figure 3.6). Increasing the temperature to 1600°C, further increased the amount of TiO_nC_{1-n}, but the powder was still a mixture of TiO_nC_{1-n} and Ti_2O_3 phases. No free carbon was detected in the heat treated powder C2, which indicated that carbon probably dose not reduce TiO_2 to TiO_nC_{1-n} when the C/TiO_2 ratio corresponds to equation 3-2.

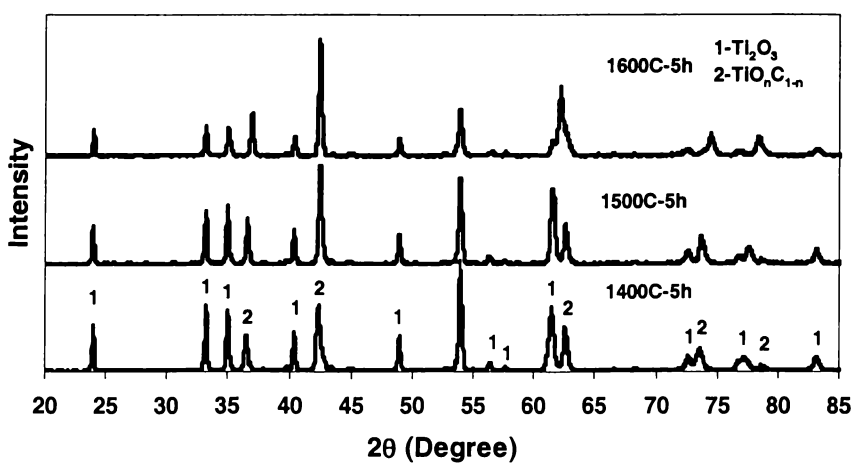

Figure 3.6 The XRD patterns of C2 powder after being different heat treatments.

C3 powder still had un-reacted carbon after being heat treated at 1400°C (Figure 3.7). TiO_nC_{1-n} is the major phase and Ti_2O_3 and C are minor phases in the powder. When temperature was increased to 1500°C and 1600°C, more free carbon is used and the amount of TiO_nC_{1-n} significantly increased. A comparison of the XRD patterns, it shows that C3 powder contains more TiO_nC_{1-n} phase than C2 powder, and also higher temperatures favour for the reduction of TiO_2 to TiO_nC_{1-n}.

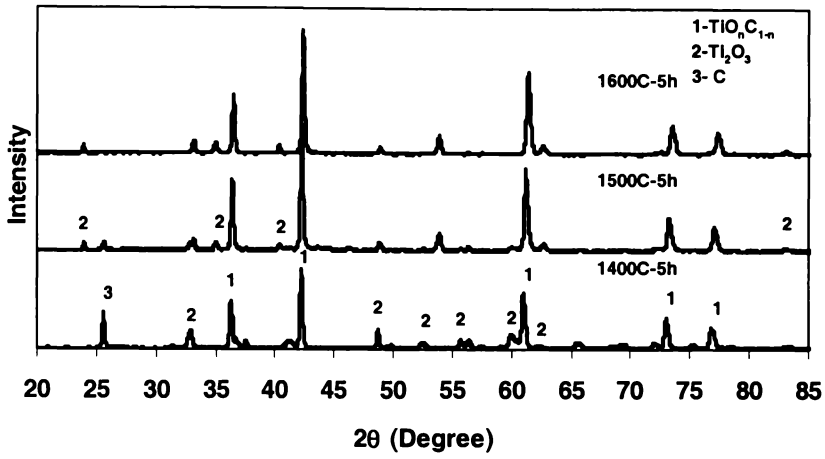

Figure 3.7 The XRD patterns of C3 powder after different heat treatments.

C4 powder had the highest C/TiO_2 mole ratio of the TiO_2/C composite powder. After being heat treatment at 1400°C, C4 powder contained a mix of free carbon, Ti_2O_3 and TiO_nC_{1-n} phase (Figure 3.8). When the temperature was increased to 1500°C or 1600°C, only peaks of cubic TiO_nC_{1-n} were identified in the XRD patterns. The data clearly show that the reaction temperature decrease as the C/TiO_2 ratio increases. This might be because the size of the C/TiO_2 reaction couples in the as-milled TiO_2/C composite powder with a higher C/TiO_2 mole ratio is finer as shown in Figure 3.2.

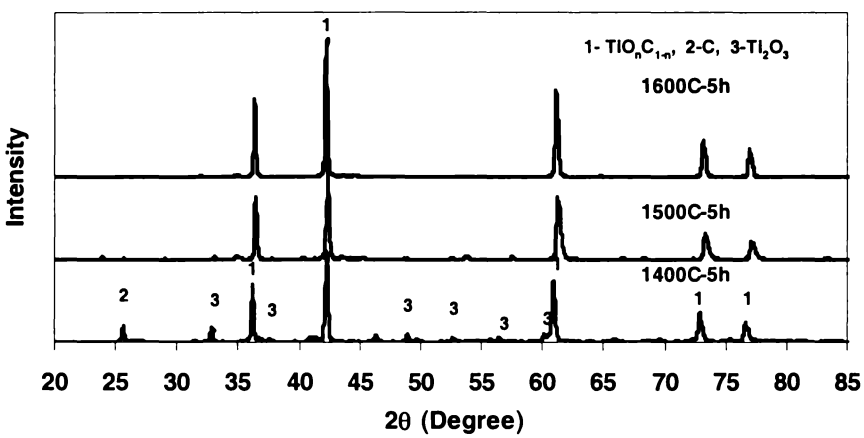

Figure 3.8 The XRD patterns of C4 powder after different heat treatments.

3.2 Solid state reactions between Al and TiO_x or TiO_nC_{1-n}

3.2.1 Introduction

Aluminum can reduce metal oxides. Solid state reactions between Al and TiO_2 have been previously studied [3-5]. Ying [5] discussed the Al and TiO_2 reaction and the microstructure of the Al/TiO_2 composite powder during heating. The purpose of this study is to establish the phase formation process when Al/TiO_2, Al/Ti_2O_3, and Al/TiO_nC_{1-n} composites are heated. The starting powders were Al, TiO_2 and powders C1 to C4. A series of powders were produced by high energy ball milling for 4 hours under argon (Table 3.1).

Table 3.1 Composites produced by high energy ball milling

Composite	Starting powder	Target phases	Nominal reaction
A1	Al/C0 (TiO_2)	Ti, Al_2O_3	$3TiO_2 + 4Al = 3Ti + 2Al_2O_3$
B1	Al/C1 (Ti_2O_3)	Ti, Al_2O_3	$Ti_2O_3 + 2Al = 2Ti + Al_2O_3$
C1	Al/C2 (Ti_2O_3 and TiO_nC_{1-n})	Ti, Al_2O_3	$Ti_2O_3 + 2Al = 2Ti + Al_2O_3$ $3TiO_nC_{1-n} + 2Al = 3Ti + Al_2O_3$
D1	Al/C3 (TiO_nC_{1-n})	Ti, Al_2O_3 and TiC	$3TiO_nC_{1-n} + 2Al = 3Ti + Al_2O_3$+TiC
E1	Al/C4 (TiO_nC_{1-n})	Ti, Al_2O_3 and TiC	$3TiO_nC_{1-n} + 2Al = 3Ti + Al_2O_3$+TiC
A2	Al/C0 (TiO_2)	Ti_3Al, Al_2O_3	$3TiO_2 + 5Al = Ti_3Al + 2Al_2O_3$
B2	Al/C1 (Ti_2O_3)	Ti_3Al, Al_2O_3	$3Ti_2O_3 + 8Al = 2Ti_3Al + 3Al_2O_3$
C2	Al/C2 (Ti_2O_3 and TiO_nC_{1-n})	Ti_3Al, Al_2O_3	$3Ti_2O_3 + 8Al = 2Ti_3Al + 3Al_2O_3$ $3\ TiO_nC_{1-n} + 3Al = Ti_3Al + Al_2O_3$
D2	Al/C3 (TiO_nC_{1-n})	Ti_3Al, Al_2O_3 and TiC	$3TiO_nC_{1-n} + 3Al = Ti_3Al + Al_2O_3$+TiC
E2	Al/C4 (TiO_nC_{1-n})	Ti_3Al, Al_2O_3 and TiC	$3TiO_nC_{1-n} + 3Al = Ti_3Al + Al_2O_3$+TiC
A3	Al/C0 (TiO_2)	TiAl, Al_2O_3	$3TiO_2 + 7Al = 3TiAl + 2Al_2O_3$
B3	Al/C1 (Ti_2O_3)	TiAl, Al_2O_3	$Ti_2O_3 + 4Al = 2TiAl + Al_2O_3$
C3	Al/C2 (Ti_2O_3 and TiO_nC_{1-n})	TiAl, Al_2O_3	$Ti_2O_3 + 4Al = 2TiAl + Al_2O_3$ $3TiO_nC_{1-n} + 5Al = 3TiAl + Al_2O_3$
D3	Al/C3 (TiO_nC_{1-n})	TiAl, Al_2O_3 and TiC	$3TiO_nC_{1-n} + 5Al = 3TiAl + Al_2O_3$+TiC
E3	Al/C4 (TiO_nC_{1-n})	TiAl, Al_2O_3 and TiC	$3TiO_nC_{1-n} + 5Al = 3TiAl + Al_2O_3$+TiC

3.2.2 Phase formation

The as-milled B1 and B3 composite powder microstructure of powder particles are shown in Figure 3.9. The bright phase is Ti_2O_3 and the dark phase is Al. After 4 hours milling in the SPEX mill, the Ti_2O_3 particles size in B1 had an average of about 1 μm. The Ti_2O_3 particles were uniformly distributed of in an Al matrix. The Ti_2O_3 particles in composite powder B3 had an average size of about 2 μm and were also uniformly distributed in Al matrix. The rest of the composite powders used in this study had similar microstructures to those of B1 and B3.

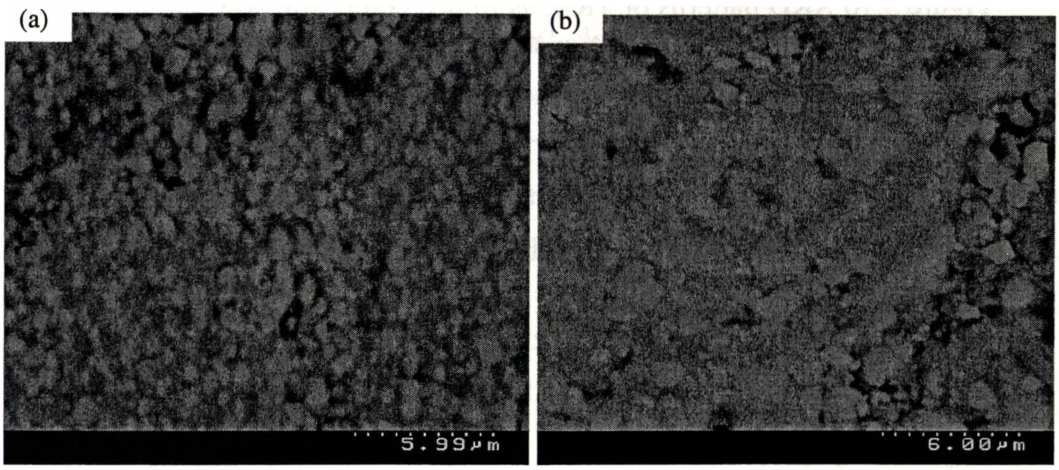

Figure 3.9 SEM micrograph of as-milled B1 (a) and B2 (b) composite powders after 4 hours of milling.

The XRD data indicates no significant reaction between Al and TiO_2 during milling (Figure 3.10). After sintering at 1300°C, the targeted metal Ti phase had still not been obtained. Instead, α-Ti(Al,O), which is the solid solution of oxygen and Al in Ti, formed. The Al_2O_3 phase formed at the same time. When the sintering temperature was increased to 1650°C, the phases in composite A1 remained stable. A small amount of TiO phase formed above 1650°C because oxygen in the Ar atmosphere caused oxidation.

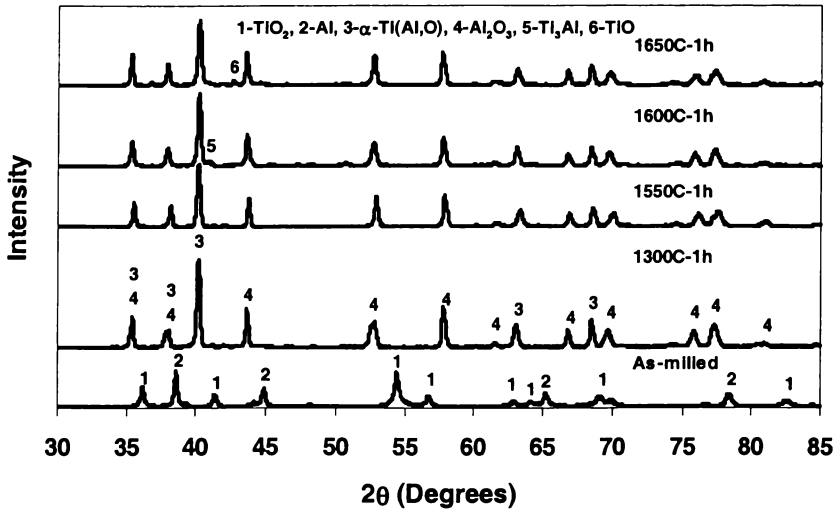

Figure 3.10 XRD patterns of TiO_2, as-milled composite powder A1, and composite A1 sintered at different temperatures.

Composites A1 to C1 consisted of α-Ti(Al,O) with a substantial amount of dissolved Al and oxygen, and Al_2O_3 phases after heat treatment at 1300°C (Figure 3.11). The Al and oxygen contents of the metallic Ti(Al,O) phase, measured by EDX will be discussed in chapter 4.

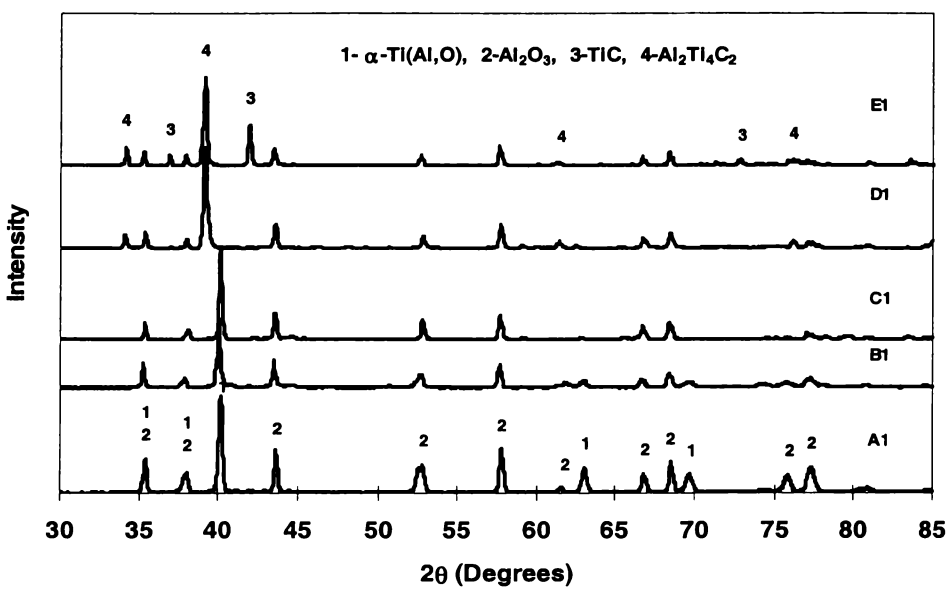

Figure 3.11 XRD patterns of composites A1 to E1 after sintering at 1300°C for 1 hour.

Ti(Al,O) present in composites A1, B1 and C1 indicates that Al can reduce not only TiO_2 but also the titanium suboxides Ti_2O_3 and TiO_nC_{1-n}. The XRD patterns indicated that Al_2O_3 decreased from composite A1 to C1. Sintering the composites at a higher temperature did not affect phase composition. The small

TiO peak in composite C1 (Figure 3.12) was caused by the reaction between the material and oxygen present in the argon.

After being heated to 1300°C, the major phases of the composite D1 were $Al_2Ti_4C_2$ and Al_2O_3. There were no TiC peaks probably because that the n value of the TiO_nC_{1-n} phase in the initial D1 powder was still high enough to prevent TiC being formed from the $Al_2Ti_4C_2$. XRD pattern of composite E1 clearly shows the TiC peaks, indicating that E1 was a composite of $Al_2Ti_4C_2/Al_2O_3/TiC$. This shows that the n value of the TiO_nC_{1-n} phase in initial E1 powder must be relatively small and the extra carbon reacted with Ti to form TiC the $Al_2Ti_4C_2$ formed. The intensity of the Al_2O_3 peaks decreased from composite D1 to E1. When sintering temperature was increased to 1650°C, the phases of composites D1 and E1 remained stable.

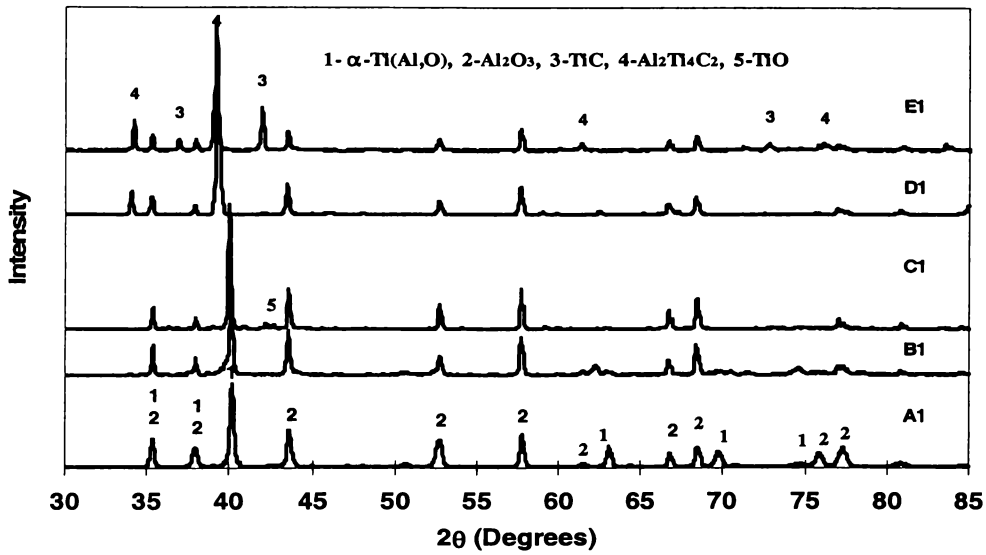

Figure 3.12 XRD patterns of composites A1 to E1 after sintering at 1650°C for 1 hour.

This study shows that when composite powders Al to C1 are heated above 1300°C, Al and TiO_2 or Ti_2O_3 react to form α-Ti(Al,O) and Al_2O_3. When composite powders D1 and E1 are heated above 1300°C, Al and TiO_nC_{1-n} react to form $Al_2Ti_4C_2$ and Al_2O_3. If the n value of TiO_nC_{1-n} is low enough, as in the C4 powder, TiC also forms.

As in the α-Ti(Al,O) based composites, the Ti_3Al and Al_2O_3 phases formed after sintering composites A2 to C2 at 1300°C. These phases were stable when the samples were sintered at higher temperatures (Figure 3.13 and 3.14). The small

amount of TiO composite B2 was due to the reaction between titanium and oxygen present in argon. The intensity of Al_2O_3 peaks decreased from composite A2 to C2. The XRD patterns indicated that the matrix phase of composites D2 and E2 was $Al_2Ti_4C_2$ mixed with a small amount of Ti_3Al. When sintering temperature increased to 1650°C, the phases in composite D2 and E2 were stable. The TiC phase was present in composite E2, indicating that the value of n in TiO_nC_{1-n} was greater in E2 powder than in D2 powder.

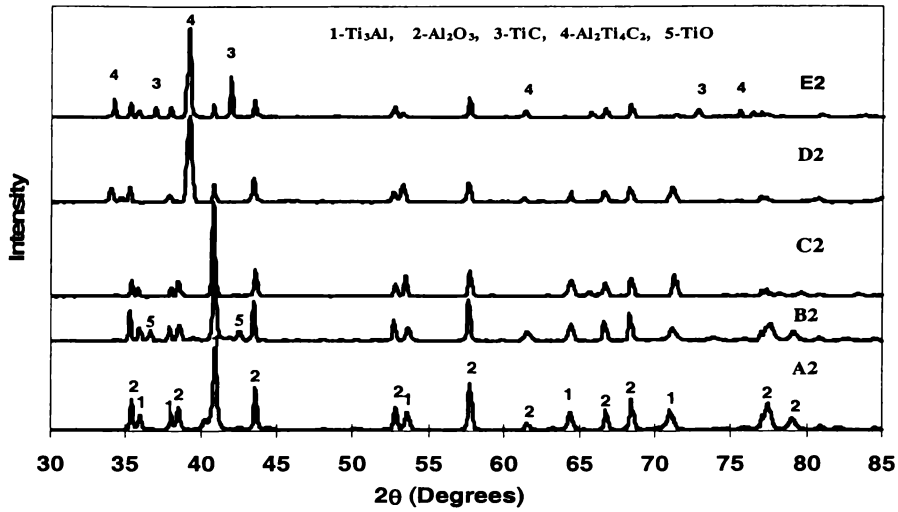

Figure 3.13 XRD patterns of composites A2 to E2 after sintering at 1300°C for 1 hour.

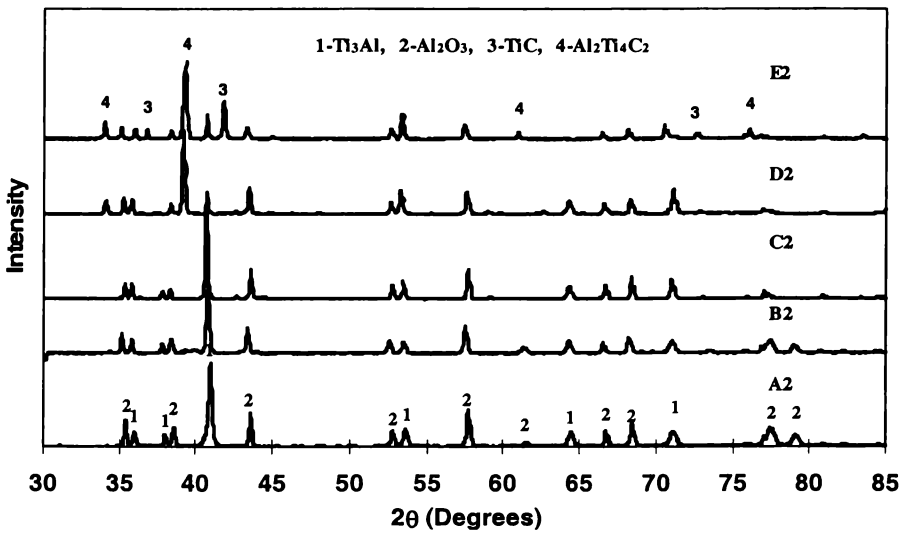

Figure 3.14 XRD patterns of composites A2 to E2 after sintering at 1650°C for 1 hour.

This study shows that when composite powders A2 to C2 are heated to 1300°C and above, Al and TiO_2 or Ti_2O_3 react to form Ti_3Al and Al_2O_3. When composite powders D2 and E2 are heated above 1300°C, Al and TiO_nC_{1-n} react to form $Al_2Ti_4C_2$, Ti_3Al and Al_2O_3. If the n value is low enough, TiC also forms.

The TiAl and Al_2O_3 phases formed when composites A3, B3, and C3 were sintered at 1300°C. These phases were stable when the samples were sintered at higher temperatures (Figures 3.15 and 3.16). The presence of small amount of α-Ti and Ti_3Al in composites A3 and B3 may be due to the non-uniform distribution of the Al phase in the initial powder. The XRD patterns of composites D3 and E3 indicated that the matrix phases of the composites were $Al_2Ti_4C_2$ with a small amount of TiAl phase. The TiC phase was clearly present in composite E3. When sintering temperature increased to 1650°C, the phases of composites D3 and E3 remained stable.

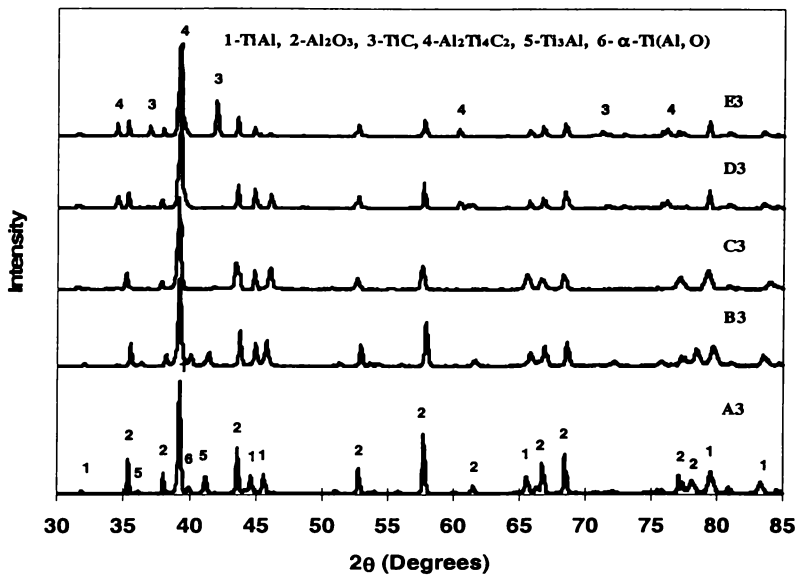

Figure 3.15 XRD patterns of composites A3 to E3 after sintering at 1300°C for 1 hour.

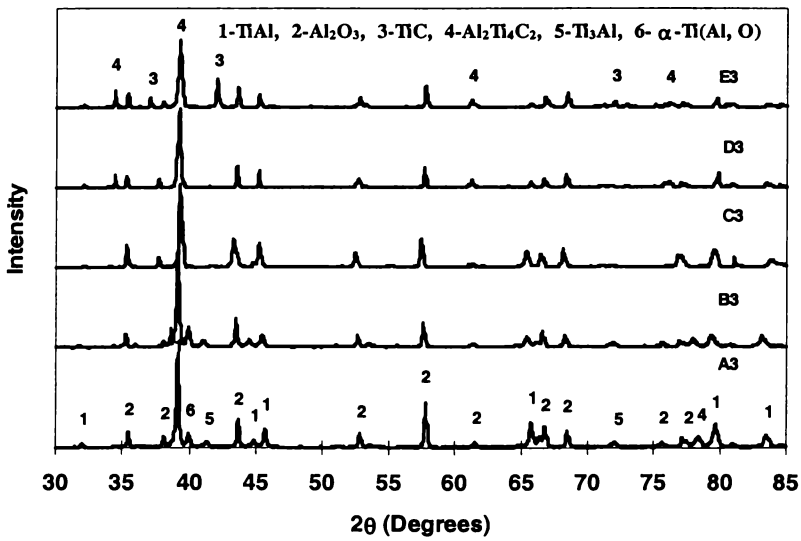

Figure 3.16 XRD patterns of composites A3 to E3 after sintering at 1650°C for 1 hour.

This study shows that heating composite powders A3 to C3 to 1300°C and above allows the Al to react with TiO_2 or Ti_2O_3 and form TiAl and Al_2O_3. When composite powders D3 and E3 are heated to 1300°C and above, the Al and TiO_nC_{1-n} react to form $Al_2Ti_4C_2$, TiAl and Al_2O_3. If the n value in TiO_nC_{1-n} is low enough TiC also forms.

3.3 Discussion

Carbon is used as a common reducing agent for carbothermal reactions. Much work has been done on increasing the efficiency of reducing ilmenite and rutile [6]. This study shows the reaction between carbon and rutile started at 1100°C. The lower reaction temperature was due to forming of TiO_2/C composite powder using high energy ball milling. Forming titanium suboxides depended on the initial TiO_2 and carbon mole ratio. This study showed that carbon can reduce TiO_2 to pure Ti_2O_3. As the amount of carbon increases, TiO_2 can be reduced to TiO_nC_{1-n}. However, TiO_2 could not be reduced to pure TiO by increasing the C/TiO_2 ratio. Instead, TiO_nC_{1-n} was formed. When the carbon ratio in C/TiO_2 is high enough, TiC is the reaction product because TiC is a more thermodynamically stable phase [7].

Zhang et al [8] reported the reaction kinetic and microstructure development when TiO_2 and Al reacted to form α-Ti and Al_2O_3. This study showed that different titanium alloy or titanium aluminide/Al_2O_3 composites can be formed by using different initial Al/TiO_2 mole ratios. Aluminium cannot reduce TiO_2 and Ti_2O_3 to pure Ti. Instead, α-Ti(Al,O), which is a solid solution of oxygen and aluminium in a Ti matrix is formed. As the aluminium amount increases, $Ti_3Al(O)$, and TiAl(O) can be formed. The phases in the composites produced from various reactions were stable over a wide range of sintering temperatures (1300°C to 1650°C).

Reactions between Al and TiO_nC_{1-n} form the $Al_2Ti_4C_2/Al_2O_3$ ceramic-ceramic composite. The $Al_2Ti_4C_2$ is a stable phase. The $Al_2Ti_4C_2$ formed at the interface of Ti(Al) solution and SiC particles in the Ti-alloy/SiC metal matrix composite [9]. When the aluminium content in the starting Al/ TiO_nC_{1-n} composite powders

increased, the $Al_2Ti_4C_2$ still forms but a small amounts of Ti_3Al and TiAl also form. It is clear whether TiC can form from the reaction between Al and TiO_nC_{1-n} depends on the n value of the TiO_nC_{1-n} phase. When n is small enough, TiC forms. Further work is needed to quantify the critical value.

3.4 Summary

This study shows that heating C/TiO_2 composite powder to a high temperature can produce Ti_2O_3 powder. When the carbon/TiO_2 ratio in the starting C/TiO_2 composite powder increases, pure TiO phase cannot be obtained. Instead TiO_nC_{1-n} forms. At higher C/TiO_2 ratios, the initial reaction temperature decreases because of the finer C/TiO_2 composite structure.

The actual reactions between Al and TiO_2, Ti_2O_3 and TiO_nC_{1-n} can be summarized by the following reactions.

$$3TiO_2 + 4Al \rightarrow 3\alpha\text{-}Ti(Al,O) + 2Al_2O_3$$

$$Ti_2O_3 + 2Al \rightarrow 2\alpha\text{-}Ti(Al,O) + Al_2O_3$$

$$TiO_nC_{1-n} + Al \rightarrow Al_2Ti_4C_2 + Al_2O_3 \text{ (When n is large)}$$

$$TiO_nC_{1-n} + Al \rightarrow Al_2Ti_4C_2 + Al_2O_3 + TiC \text{ (When n is small)}$$

When the amount of aluminium is increased, the reactions in the initial composite powders become:

$$3TiO_2 + 5Al \rightarrow Ti_3Al + 2Al_2O_3$$

$$3Ti_2O_3 + 8Al \rightarrow 2Ti_3Al + 3Al_2O_3$$

$$TiO_nC_{1-n} + Al \rightarrow Al_2Ti_4C_2 + Al_2O_3 + Ti_3Al \text{ (When n is large)}$$

$$TiO_nC_{1-n} + Al \rightarrow Al_2Ti_4C_2 + Al_2O_3 + TiC + Ti_3Al \text{ (When n is small)}$$

When the amount of aluminium is increased further, the reactions in the starting composite powders become:

$$3TiO_2 + 7Al = 3TiAl + 2Al_2O_3$$

$$Ti_2O_3 + 4Al = 2TiAl + Al_2O_3$$

$$TiO_nC_{1-n} + Al \rightarrow Al_2Ti_4C_2 + Al_2O_3 + TiAl \text{ (When n is large)}$$

$$TiO_nC_{1-n} + Al \rightarrow Al_2Ti_4C_2 + Al_2O_3 + TiC + TiAl \text{ (When n is small)}$$

References

1. I.E. Grey, D.G. Jones, A.F. Reid, Transactions of the Institution of Mining and Metallurgy, **82C,** 151-152 (1973).
2. D.G. Jones, Transactions of the Institution of Mining and Metallurgy, **82C,** 186-192 (1973).
3. N.J. Welham, Materials Science and Engineering, **A255**, 81-89, (1998).
4. N.J. Welham, Intermetallics, **6**, 363-368, (1998).
5. D.Y. Ying, PhD Thesis, University of Waikato, (2001).
6. N.J. Welham, Minerals Enigneering **9**, 1189-1200 (1996).
7. Y. Chen, T. Hwang, M. Marsh and J.S. Williams, Metallurgical and Materials Transactions A, **28A,** 1115-1121, (1997).
8. D.Y. Ying, D.L. Zhang, and M. Newby, Metallurgical and Materials Transaction in pressing.
9. E.L. Hall, A.M. Ritter, J. Mater. Res., **8**, 1158-1168, (1993).

Chapter Four
Processing and Microstructures of Ti_xAl_y/Al_2O_3 and $Al_2Ti_4C_2/Ti_xAl_y/Al_2O_3/TiC$ Composites

4.1 Introduction

This chapter described the fabrication of Ti_xAl_y/Al_2O_3 and $Al_2Ti_4C_2/Ti_xAl_y/Al_2O_3/TiC$ composites and the processing condition /microstructure of the composites. Different composites based on α-Ti(Al,O), Ti_3Al, TiAl and $Al_2Ti_4C_2$ were studied and a code was assigned to the composites for convenience (Table 4.1).

Table 4.1 Code used for composites produced and their Al_2O_3 content (vol.%).

Code	Matrix	Al_2O_3	Code	Matrix	Al_2O_3	Code	Matrix	Al_2O_3
A1	α-Ti(Al,O)	58	A2	Ti_3Al	56	A3	TiAl	47
B1	α-Ti(Al,O)	55	B2	Ti_3Al	47	B3	TiAl	43
C1	α-Ti(Al,O)	48	C2	Ti_3Al	44	C3	TiAl	39
D1	$Al_2Ti_4C_2$	42	D2	$Al_2Ti_4C_2/Ti_3Al$	38	D3	$Al_2Ti_4C_2$/TiAl	37
E1	$Al_2Ti_4C_2$	39	E2	$Al_2Ti_4C_2/Ti_3Al$	37	E3	$Al_2Ti_4C_2$/TiAl	35

Theoretical densities of Ti, Ti_xAl_y, $Al_2Ti_4C_2$, TiC and Al_2O_3 are listed in Table 4.2. The theoretical densities of Ti_xAl_y/Al_2O_3 and $Al_2Ti_4C_2/Ti_xAl_y/Al_2O_3/TiC$ composites were calculated according to the rule of mixtures (Table 4.3).

Table 4.2 Theoretical densities (g/cm^3) of Ti, Ti_xAl_y, Al_2O_3, and TiC

Material	Theoretical density	Reference
Ti	4.52	1
Ti_3Al	4.31	1
TiAl	3.87	1
$Al_2Ti_4C_2$	4.11	1
TiC	4.93	1
Al_2O_3	3.95	1

Table 4.3 Theoretical densities (g/cm^3) of composites

Code	Theoretical Density	Code	Theoretical Density	Code	Theoretical Density
A1	4.28	A2	4.07	A3	3.92
B2	4.33	B2	4.10	B3	3.91
C1	4.35	C2	4.11	C3	3.90
D1	4.37	D2	4.05	D3	3.93
E1	4.48	E2	4.35	E3	4.19

4.2 Density of composites

4.2.1 α-Ti(Al, O) and $Al_2Ti_4C_2$ based composites

The relative bulk density of the five α-Ti(Al, O) and $Al_2Ti_4C_2$ based composites (A1, B1, C1, D1, E1) increased dramatically and almost linearly from 72-82% to 92-96% as the pressure-less sintering temperature increased from 1300°C to 1650°C (Figure 4.1). After being sintered at 1650°C, the relative bulk densities of these five composites was about 92-96% of the theoretical density. The density of E1 was 72% after pressure-less sintering at 1300°C while composite D1 had a relative density of 82% when sintered under the same conditions. After being sintered at 1550°C, composite A1, B1 and C1 had relative densities 86-92% and composite C1 and D1 had 2 to 4 % lower than those of composite A1, B1 and E1.

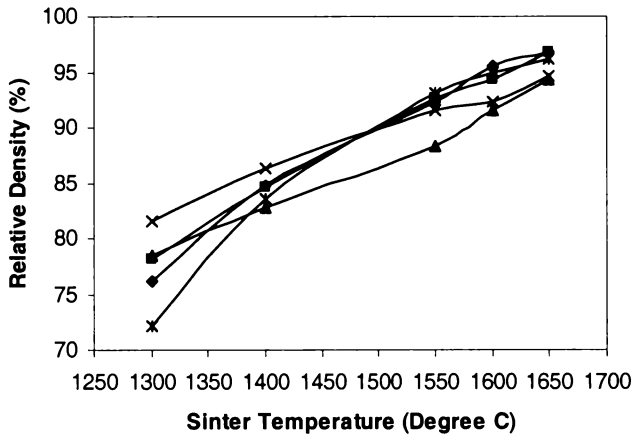

Figure 4.1 Effect of pressure-less sintering temperature on relative density of composites A1 (◆), B1 (■), C1 (▲), D1 (×) and E1 (✳).

Sintering temperature affected the size of pores in the composites. For example, samples of A1 sintered at 1400°C had a large number of open pores largely distributed in the metallic phase (Figure 4.2a). The Al_2O_3 phase was present as

small particles, which had no pores. The microstructure of the powder particles can clearly be distinguished from the bulk composite, indicating that the sintering effect was minimal. When sintering temperature was increased to 1550°C, the pores in the metallic phase disappeared (Figure 4.2b). Most of the open pores were closed and the pores were located ether inside the Al_2O_3 particles or at the $Ti(Al,O)/Al_2O_3$ interface. After being sintered at 1650°C, pores inside the Al_2O_3 particles disappeared. Although, there were some pores at the $Ti(Al,O)/Al_2O_3$ interface. Similar changes in pore structure with increasing sintering temperature were observed in composites B1 and C1 not shown.

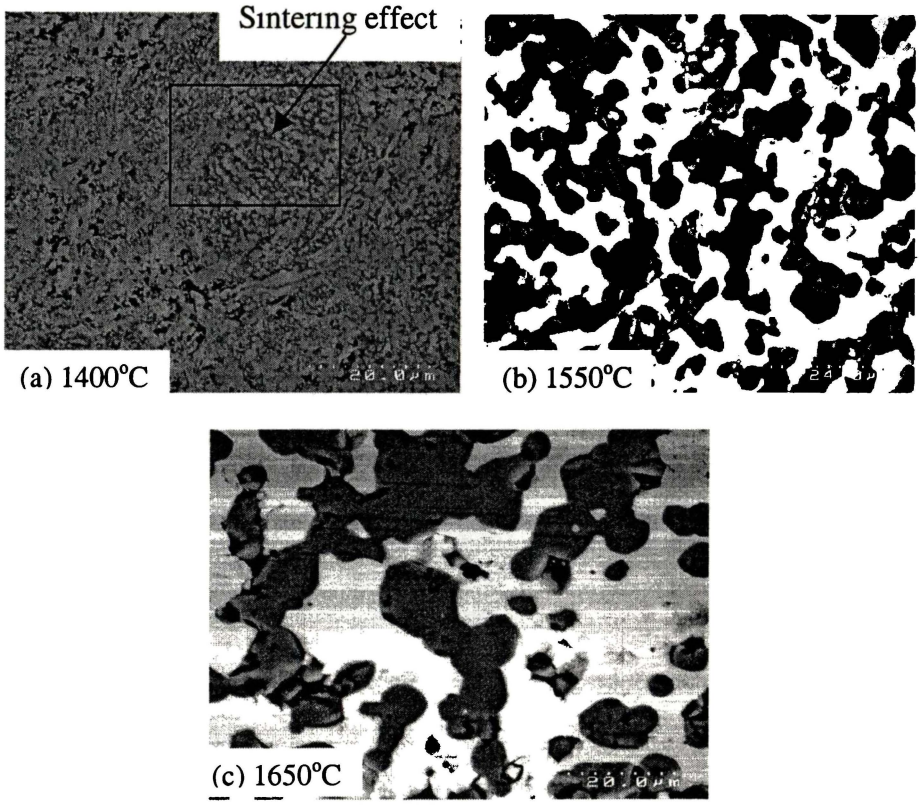

Figure 4.2 SEM images of composite A1 pressure-less sintered at 1400°C, 1550°C, and 1650°C.

The effect of being pressure-less sintering temperature on composite E1 was shown in Figure 4.3. The bright phase is $Al_2Ti_4C_2/TiC$, the dark grey phase is Al_2O_3, and very dark phase is pores. Samples sintered at 1400°C had large regions with the original powder particle microstructure. The pores were interconnected via channels. About 2-3% of the pores were inside Al_2O_3 particles or at the matrix/particle interfaces. After the samples were sintered at 1550°C, the pores became isolated. Some pores were inside the large Al_2O_3 particles but the

small particles had few pores. The pores in the metallic phase were distributed discretely. After the samples were sintered at 1650°C, pores were eliminated from the large Al_2O_3 particles and all pores were located at the metal/ceramic interfaces. These observations indicated that the sintering effect on Al_2O_3 was achieved at 1650°C. Sintering temperature had the same effect on the pores in composites D1 and E1.

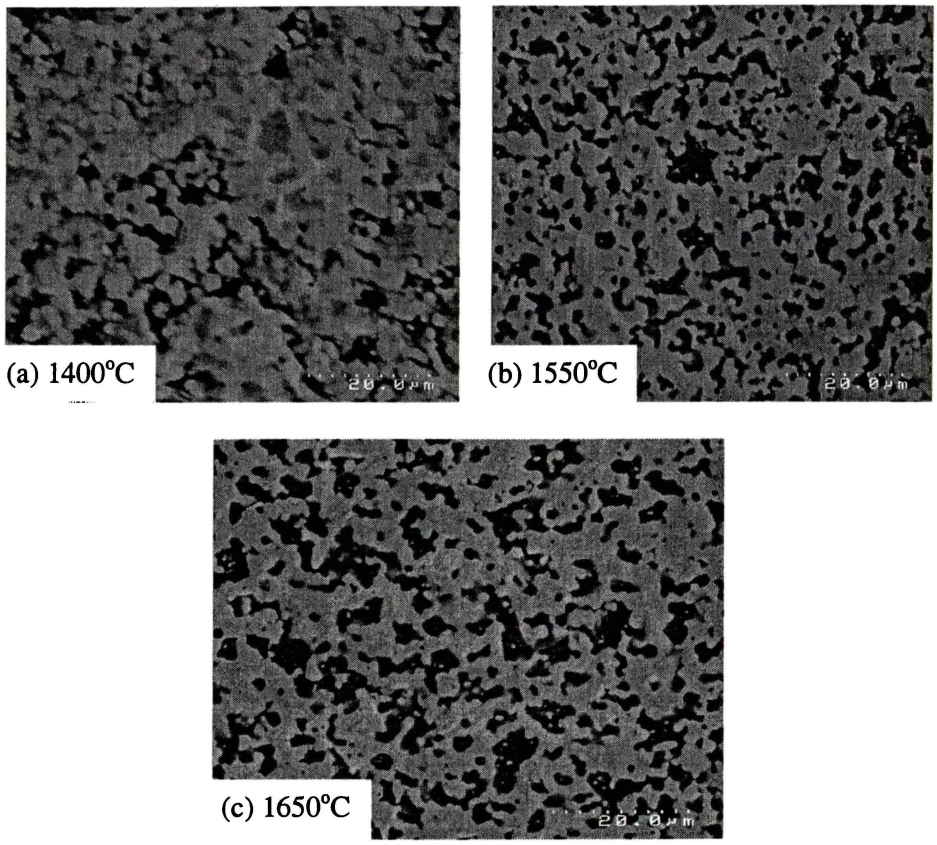

Figure 4.3 SEM images of composite E1 pressure-less sintered at 1400°C, 1550°C and 1650°C.

The effect of hipping on the relative density of pre-sintered composites was shown in Figure 4.4. After hipping, the relative density of composite A1 pre-sintered at 1400°C was increased by 8% (Fig. 4.4a). The effect of hipping on relative density decreased with increasing pre-sintering temperature. Thus, relative density increased about 2% after being pre-sintered at 1600°C or 1650°C. Hipping had a similar effect on the relative density of composite B1 (Figure 4.4b). Relative density increased by 5% after hipping of the samples pre-sintered at 1400°C. For the samples pressure-less sintered at 1650°C, the relative density increased by 1% after hipping. Relative densities of composite C1 and D1 were

increased by 4% after hipping (Figure 4.4c-d). The effect of hipping on the relative density of composite E1 was similar and only increasing 2 %.

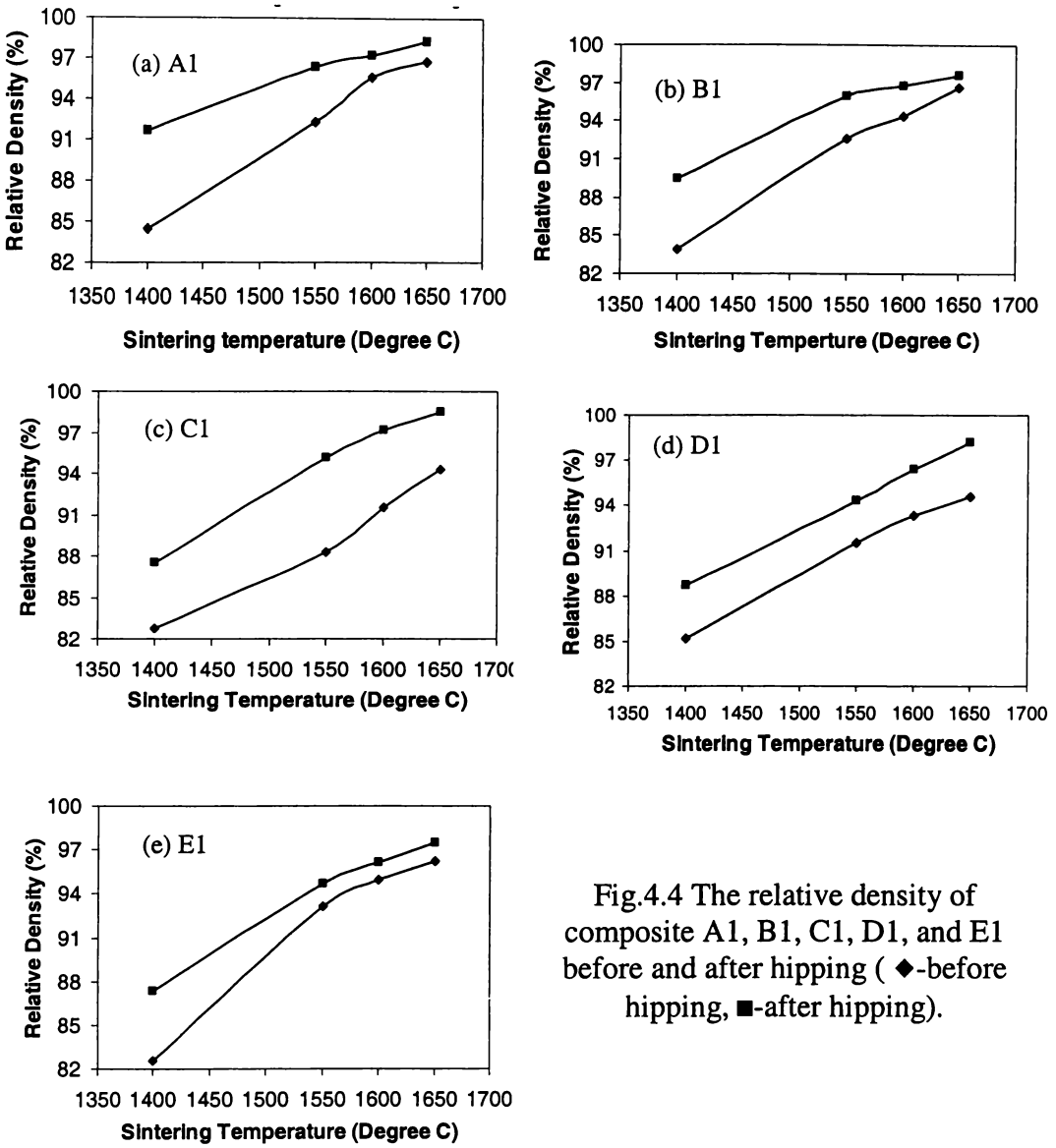

Fig.4.4 The relative density of composite A1, B1, C1, D1, and E1 before and after hipping (◆-before hipping, ■-after hipping).

Hipping reduced the number of open pores present in A1 composite sintered at 1400°C (Figure 4.5a). Hipping also removed most of pores in the Al_2O_3 particles and the Ti(Al,O) in A1 composite pre-sintered at 1550°C (Figure 4.5b). A small amount of pores were still present at Ti(Al,O)/Al_2O_3 interfaces. This indicates that closing the pores at the interfaces is more difficult than closing the pores in metallic and ceramic phases. The effect of hipping on the pore structure of pre-sintered composites B1 and C1 was similar to that on the composite A1 not shown. The extent of sintering increased dramatically after hipping composites D1 and E1 pre-sintered at 1400°C. For the samples being pre-sintered at 1550°C,

most of the pores were eliminated in both metallic and ceramic phases. The remaining pores were located at $Al_2Ti_4C_2/Al_2O_3$ interfaces.

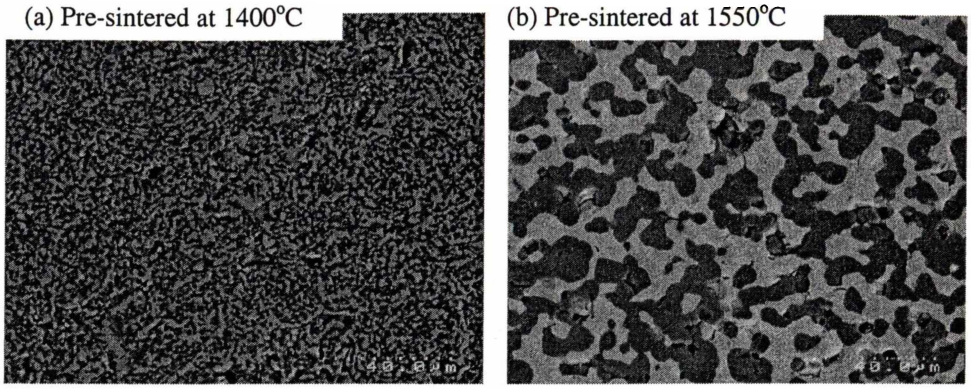

Figure 4.5 SEM images of composite A1 produced by hipping pre-sintered samples.

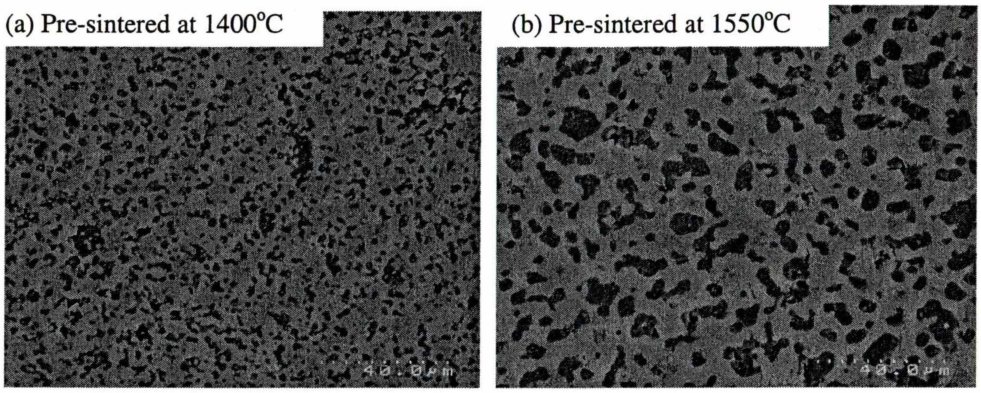

Figure 4.6 SEM images of composite E1 produced by hipping pre-sintered samples.

4.2.2 Ti_3Al and $Al_2Ti_4C_2/Ti_3Al$ based composites

The relative bulk density of the five α-Ti(Al, O) and $Al_2Ti_4C_2$ based composites (A2, B2, C2, D2, E2) increased dramatically and almost linearly from 70-79% to 93-96% as the pressure-less sintering temperature increased from 1300°C to 1650°C (Figure 4.7). There was about 9% difference in relative densities of these five composites after being sintered at 1300°C. When the sintering temperature was raised to 1650°C, the difference was narrowed down to 4%. The relative densities of these five composites increased approximately linearly with increasing the sintering temperature. For composite B2, the relative density increased almost linearly with sintering temperature in the range of 1400°C to 1650°C.

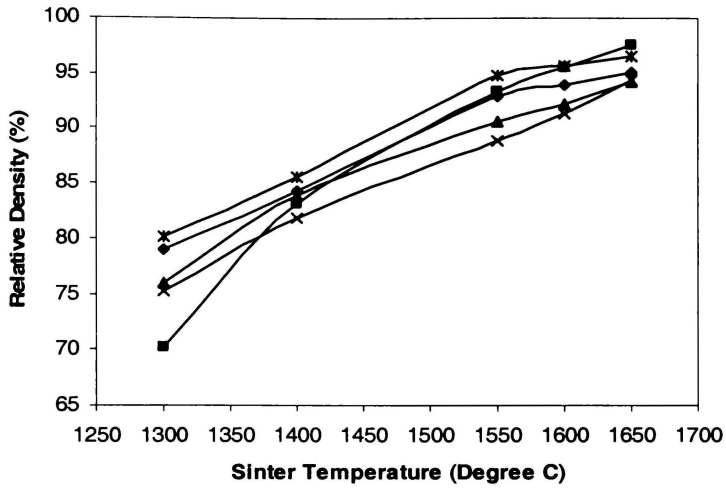

Figure 4.7 Effect of pressure-less sintering temperature on relative density of composites A2 (◆), B2 (■), C2 (▲), D2 (×) and E2 (✳).

The pores were largely distributed in the Ti_3Al phase, and both open pores and closed pores were present when the samples were sintered at 1400°C (Figure 4.8a). After sintering at 1550°C, the metallic phase became fully dense by eliminating the pores and at the same time pores formed inside the coarsened Al_2O_3 particles. When the sintering temperature was raised to 1650°C, there were still some pores in the large Al_2O_3 particles, as shown in Figure 4.8(c).

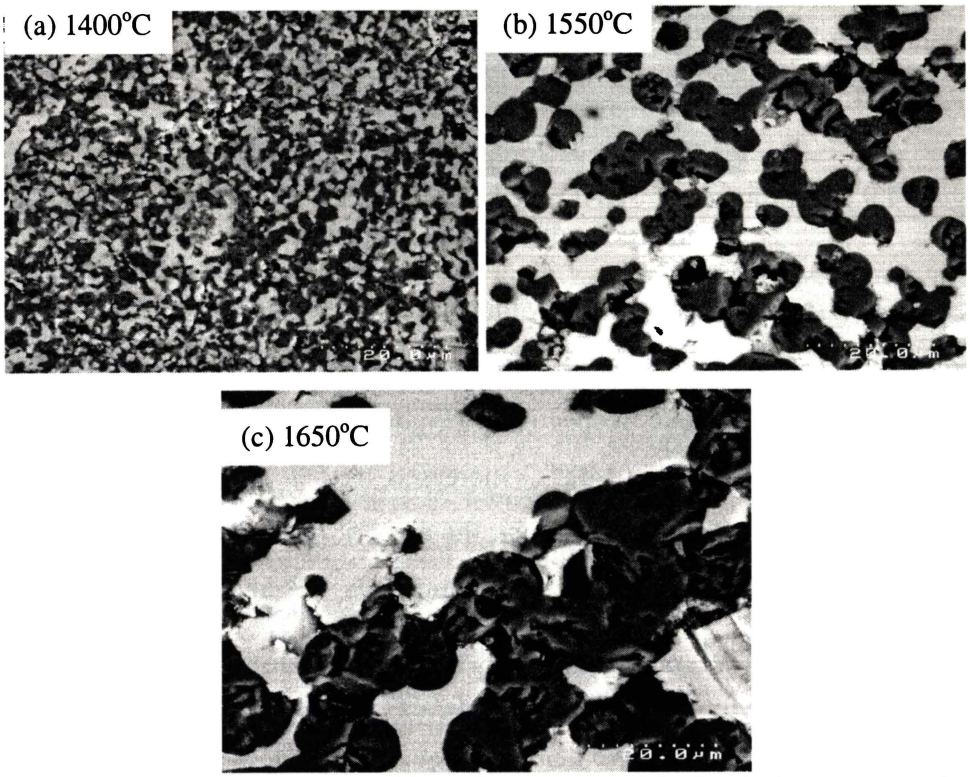

Figure 4.8 SEM images of Ti_3Al based composite A2 after being pressure-less sintered at different temperatures.

A large number of open pores were still present in composite E2 after sintering at 1400°C (Figure 4.9a). The original powder particle structure and boundaries were still evident indicating that the sintering effect at this temperature was limited. When the sintering temperature was raised to 1550°C, most of the $Al_2Ti_4C_2/Ti_3Al$ matrix became fully dense but there were some pores in the large Al_2O_3 particles. The pores were mainly at matrix/Al_2O_3 interfaces after sintering at 1650°C (Figure 4.9c).

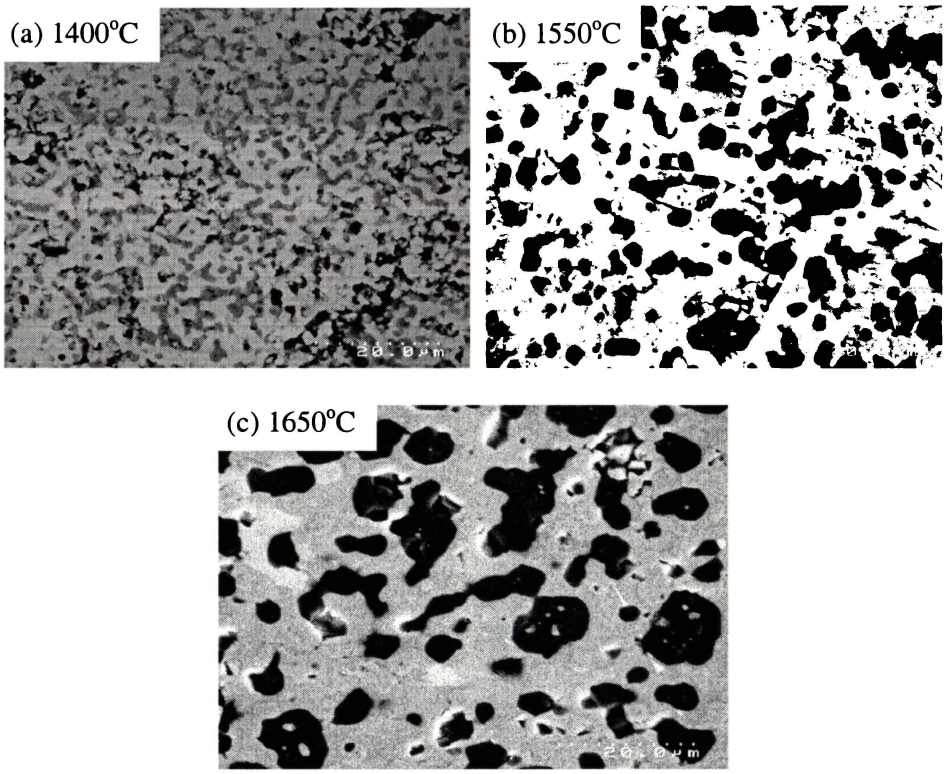

Figure 4.9 SEM images of Ti_3Al based composite E2 after being pressure-less sintered at different temperatures.

For composite A2, the relative density increased by 8% after hipping samples pre-sintered at 1400°C and increased by 4-5% after hipping samples pre-sintered at 1550°C, 1600°C and 1650°C respectively (Figure 4.10a). The relative density of composite B2 pre-sintered at 1400°C increased by 6% after hipping. With the increase of the pre-sintering temperature, the amount of relative densities increase caused by hipping became lower. For composites D2 and E2, the amount of relative density increase caused by hipping decreased from 9% to 5% for composite D2 and from 5% to 2% for composite E2. For the samples per-sintered at 1550°C and above, the relative densities had similar values in the range 97-98% after hipping.

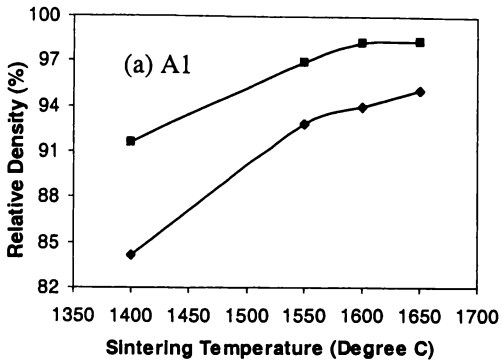

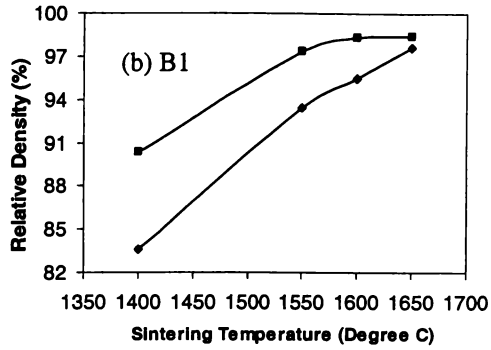

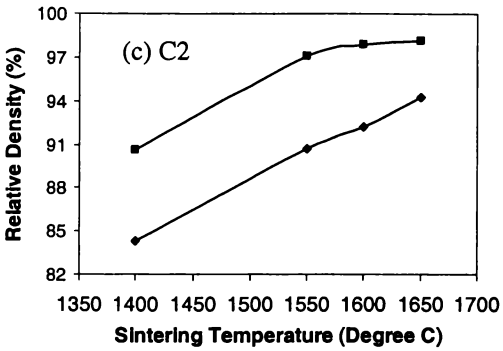

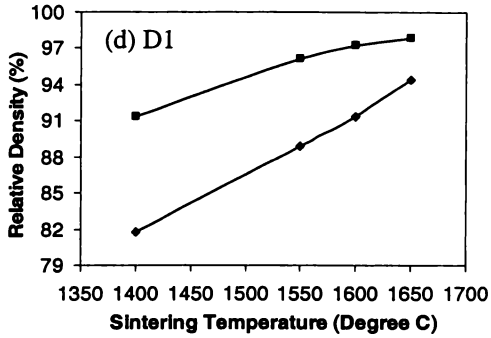

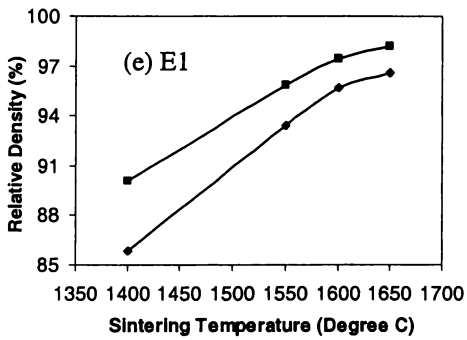

Fig.4.10 The relative density of composite A2, B2, C2, D2, and E2 before and after hipping (◆-before hipping, ■-after hipping).

For the samples pre-sintered at 1400°C, there were still some open pores present in composite A2 after hipping but the extent of sintering was dramatically improved (Figure 4.11). A number of pores were discretely distributed in the bulk sample. For sample pre-sintered at 1550°C, the composite reached fully dense. Similar pore structure was found in composites B2 and C2 after hipping not shown. Open pores were still present in composite E2 after hipping the sample pre-sintered at 1400°C (Figure 4.12). This shows the limited effect of hipping on the open pores in the composites. For the samples pre-sintered at 1550°C, there were few open pores discretely distributed mainly at the interface between the Al_2O_3 particles and the $Al_2Ti_4C_2/Ti_3Al$ matrix.

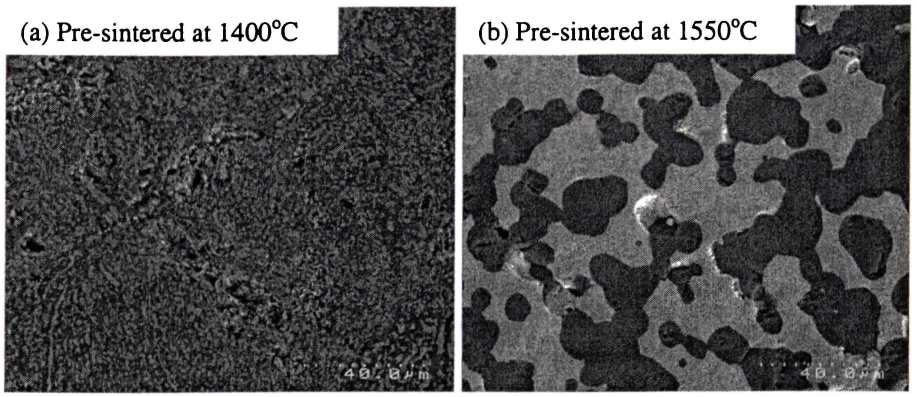

Figure 4.11 SEM images of composite A2 after hipping of pre-sintered samples.

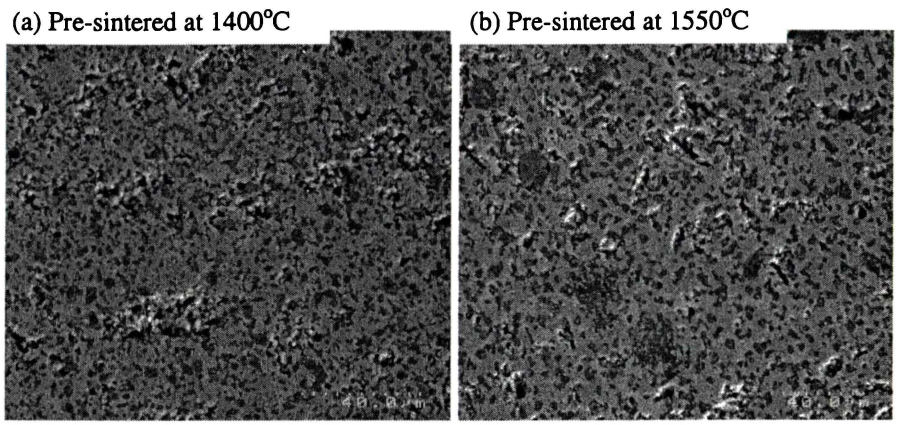

Figure 4.12 SEM images of composites E2 after hipping of pre-sintered samples.

4.2.3 TiAl and $Al_2Ti_4C_2$ based composites

Figure 4.13 shows relative densities of TiAl and $Al_2Ti_4C_2/Ti_3Al$ based composites A3, B3, C3, D3, and E3 as a function of sintering temperature. After these five composites were sintered at 1300°C for one hour, relative densities were in the range of 76 to 83%. Relative densities of composites A3 and E3 were at the higher end of the range, while those of the other composites were at the lower end. Relative densities of these five composites increased approximately linearly with increasing sintering temperature. For the samples sintered at 1600°C and 1650°C, all of these five composites had relative densities in the narrow range of 93-95%.

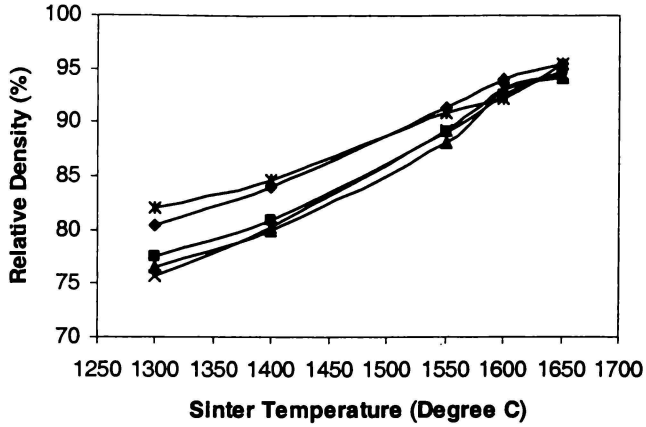

Figure 4.13 Effect of pressure-less sintering temperature on relative density of composites A3 (◆), B3 (■), C3 (▲), D3 (×) and E3 (✳).

There were a number of open pores in the TiAl phase after sintering at 1400°C. There were a very limited number of pores in the Al_2O_3 particles (Figure 4.14a). After the samples were sintered at 1550°C, the metallic phase became fully dense and the pores were mainly present inside the Al_2O_3 particles, (Figure 4.14b). There were a few pores at TiAl/Al_2O_3 interfaces. In the samples sintered at 1650°C, there were still pores present in most of the large Al_2O_3 particles.

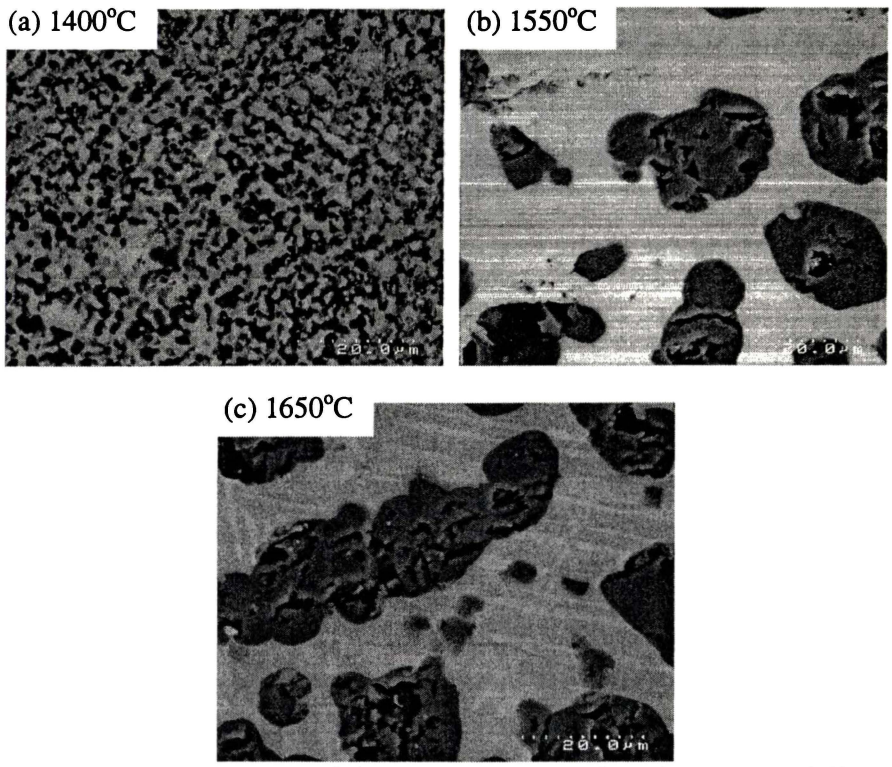

Figure 4.14 SEM images of the composite A3 after sintering at different temperatures.

For the samples sintered at 1400°C, most of the pores in composite E3 were discretely distributed in the intermetallic phase, with few pores being in the Al_2O_3 particles (Figure 4.15). After the samples were sintered at 1550°C, a small number of pores remained in the intermetallic phase and at the matrix/Al_2O_3 interfaces. After being sintered at 1650°C, there were only some large pores at the matrix/Al_2O_3 interfaces.

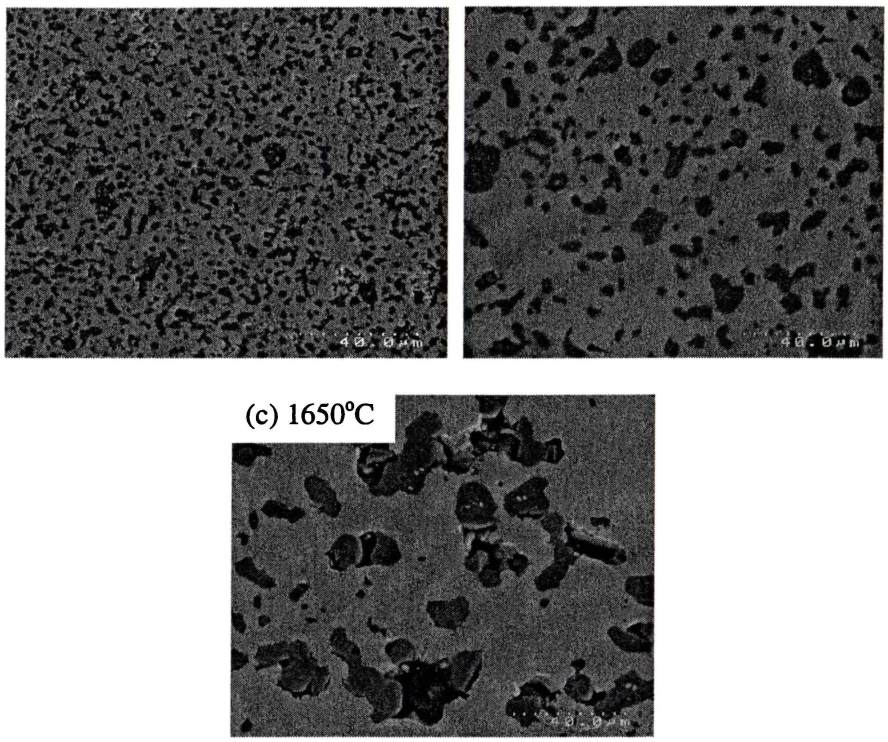

Figure 4.15 SEM images of TiAl based composite E3 after sintering at different temperatures.

The relative density of composite A3 increased by 3 to 5% after hipping, and the amount of increase appeared to be independent of pre-sintering temperature (Figure 4.16a). The composites B3, C3, D3, and E3 showed a similar effect of hipping on the relative density with pre-sintering temperature up to 1600°C. The relative densities of these composites reached about 97 to 98% after hipping of the samples pre-sintered at 1600°C and 1650°C.

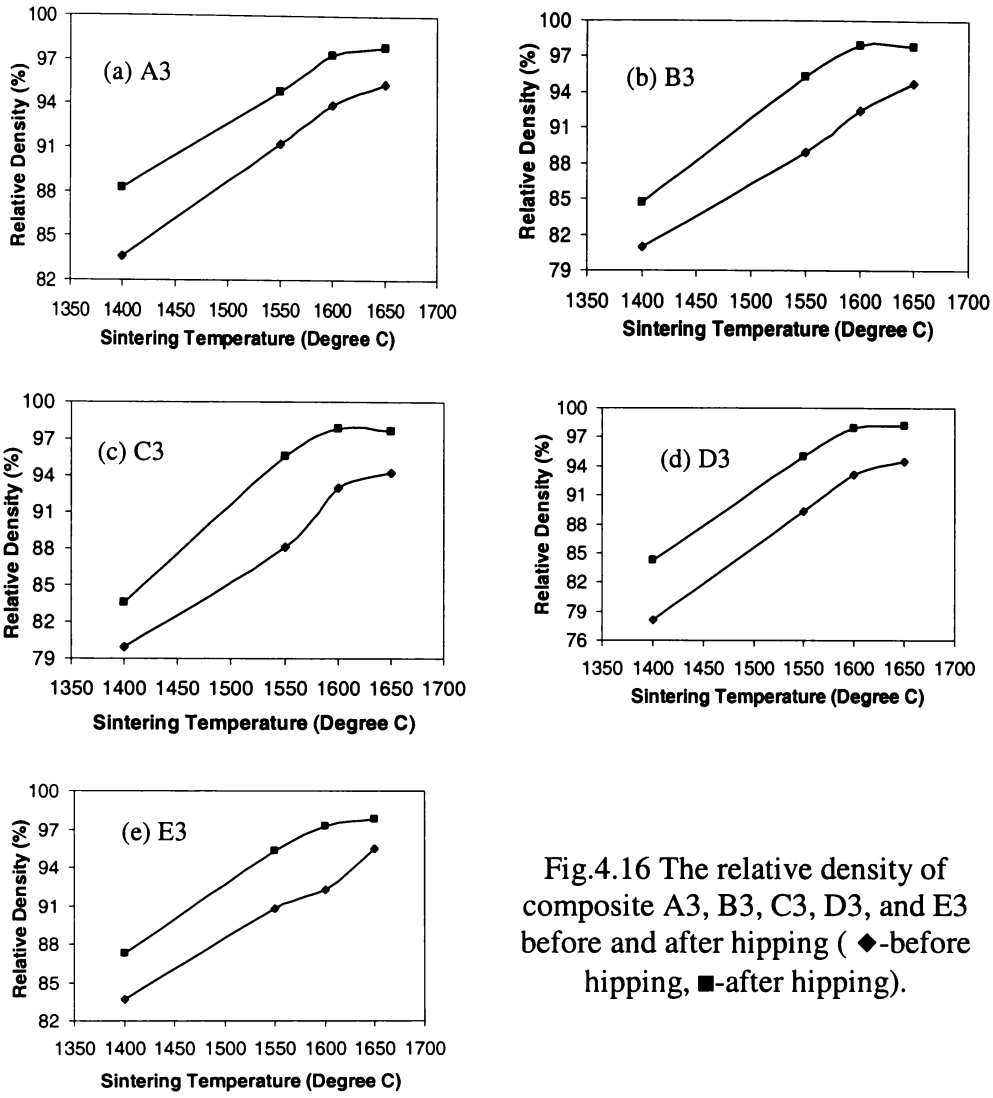

Fig.4.16 The relative density of composite A3, B3, C3, D3, and E3 before and after hipping (◆-before hipping, ■-after hipping).

The pores were grouped in composite A3 after hipping the samples pre-sintered at 1400°C (Figure 4.17). Inside each pore group, the structure of the powder particles can be clearly seen. This indicates that the open pores present limited the effect of hipping. For the samples pre-sintered at 1550°C, the TiAl matrix and the TiAl/Al_2O_3 interfaces became fully dense after hipping. The pores were mostly in Al_2O_3 particles. The pore structures in composites B3, C3, and D3 produced by hipping the pre-sintered samples were similar to that in composite A3 (not shown). For composite E3, open pores were still present in the bulk sample after hipping the samples pre-sintered at 1400°C. For the sample pre-sintered at 1550°C, large pores were observed in Al_2O_3 particles or adjacent to them (Figure 4.18).

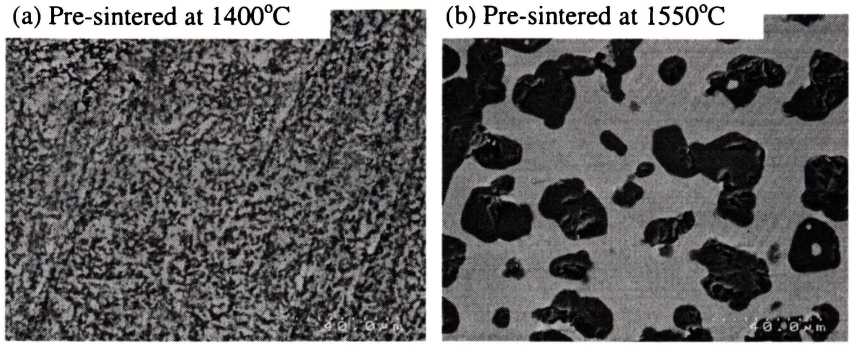

Figure 4.17 SEM images of composites A3 after hipping pre-sintered samples.

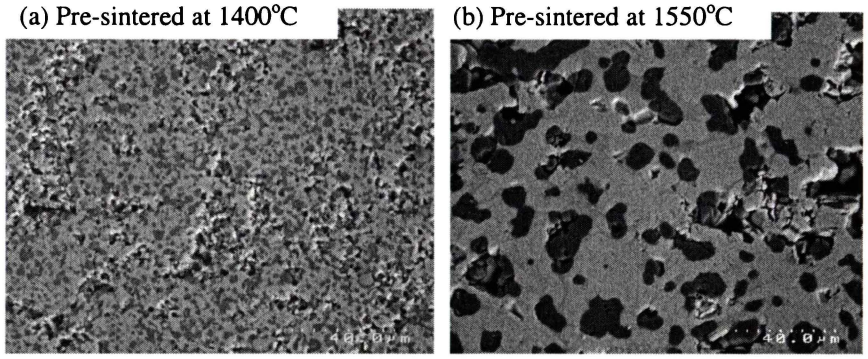

Figure 4.18 SEM images of composites E3 after hipping pre-sintered samples.

4.3 Microstructure of the composites

4.3.1 α-Ti(Al, O) and $Al_2Ti_4C_2$ based composites

The microstructure of α-Ti(Al,O) based composites A1, B1, C1, D1 and E1 produced by pressure-less sintering was shown in Figure 4.19. The composites A1, B1, and C1 consist of ceramic Al_2O_3 particles embedded in a metallic α-Ti(Al,O) matrix, and these phases are stable at temperatures up to 1650°C. In the back-scatter SEM images, the α-Ti(Al,O) matrix is the bright phase in composites A1, B1, C1 and the dark phase is Al_2O_3 particle. In composite D1 and E1, the bright phase is the $Al_2Ti_4C_2$ matrix and the dark phase is Al_2O_3 particles. The images did not show a contrast between $Al_2Ti_4C_2$ matrix and TiC particles in composite E1. After sintering at 1550°C, the Al_2O_3 particles inter-connected and form a chain. When the sintering temperature was increased to 1650°C, the small Al_2O_3 particles were consumed by large Al_2O_3 particles during coarsening. These large Al_2O_3 particles were close to a round shape, and isolated in the matrix. The Al_2O_3 particles in composites A1, B1, and C1 coarsened as sintering temperature increased, while Al_2O_3 particles in composites D1 and E1 did not show much change. The reasons are discussed in Section 4.4.

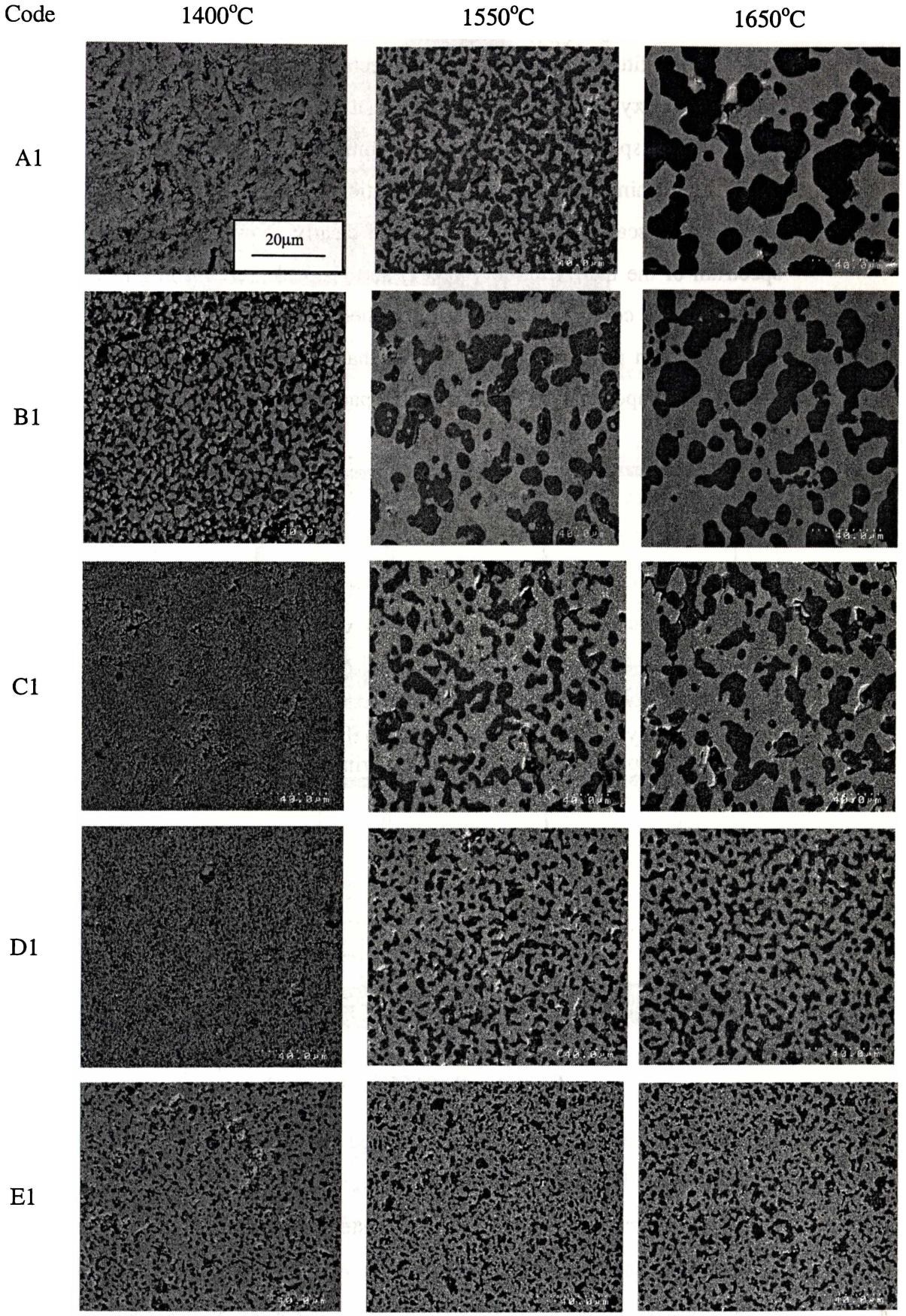

Fig. 4.19 SEM images of composites A1, B1, C1, D1, and E1 produced by pressure-less sintering at 1400°C, 1550°C, and 1650°C respectively. (40μm)

The composition of the matrix and the particles was studied with an EDX spectrometer fitted on the SEM. EDX spectrum of composite A1 matrix only had Ti, Al, and oxygen peaks, confirming that the matrix is Ti-Al-O alloy (Figure 4.20a). EDX spectrum of particles in composite A1 only had Al and oxygen peaks, confirming that they are Al_2O_3 particles (Figure 4.20b). For the composite E1, the back-scatter SEM images did not clearly show TiC particles. The EDX spectrum of the matrix had carbon, Ti and Al peaks, confirming that the matrix was a Ti-Al-C compound. Although the spectrum of the particles only shows the Al and oxygen peaks only, it suggested that TiC particles were in the $Al_2Ti_4C_2$ matrix of composite E1, and the Al_2O_3 particles did not contain TiC particles (Figure 4.21).

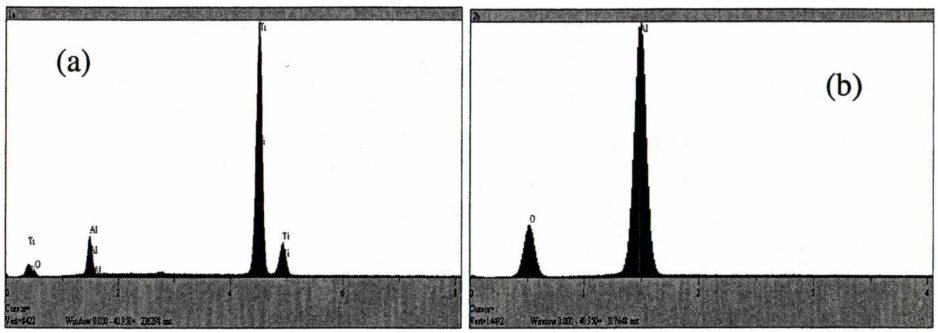

Fig 4.20 Typical EDX spectrum of (a) the matrix and (b) the particles in composite A1 produced by sintering at 1650°C for one hour.

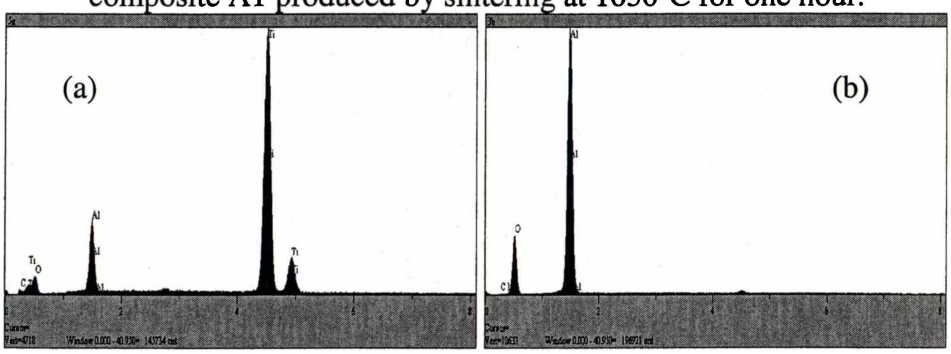

Fig 4.21 Typical EDX spectrum of the (a) matrix and (b) particles in composite E1 sintered at 1650°C for one hour.

A TEM micrograph of composite E1 sintered at 1650°C [3] clearly showed a TiC particle (Figure 4.22). The $Al_2Ti_4C_2$ matrix had a lamellar structure. The average length of the lamellar is about 5 μm. A cluster of lamellar has a width 0.6 to 0.8 μm. The lamellar has a clear boundary when abutting an Al_2O_3 particle. The overlap zone between TiC and $Al_2Ti_4C_2$ might be caused by the reaction between the TiC and $Al_2Ti_4C_2$ phases. TiC precipitates were observed in Al_2O_3 particles. EDX data indicated that the $Al_2Ti_4C_2$ matrix had 2.65 at% oxygen content.

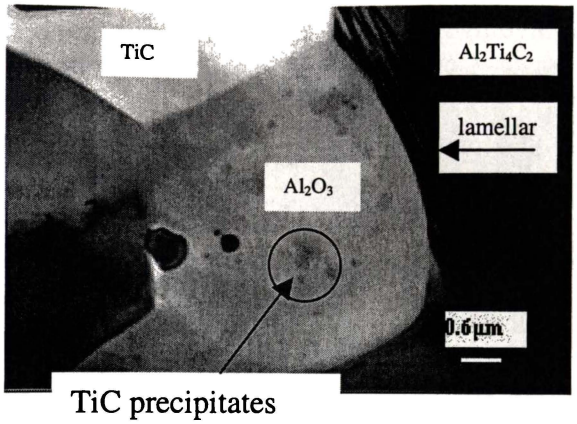

Figure 4.22 TEM micrograph of composite E1 produced by sintering at 1650°C.

The average Al_2O_3 particle size in composite B1 increased linearly with sintering temperature (Figure 4.23). Al_2O_3 particle size increased more rapidly in composites A1, C1, D1 and E1 between 1550°C to 1650°C than between 1400°C to1550°C, which indicated that the coarsening rate is more sensitive to temperatures above 1550°C. Usually coarsening rate of Al_2O_3 particles decreased from composites A1 to composite E1. The coarsening rate of Al_2O_3 particles in composites D1 and E1 was significantly lower than that in composite A1 to C1. Average Al_2O_3 particle size in composite A1 increased from 1 to 25 μm as sintering temperature from 1400°C to 1650°C while the average Al_2O_3 particle size in composite E1 increased from 2 to only 5 μm over the same temperature increase.

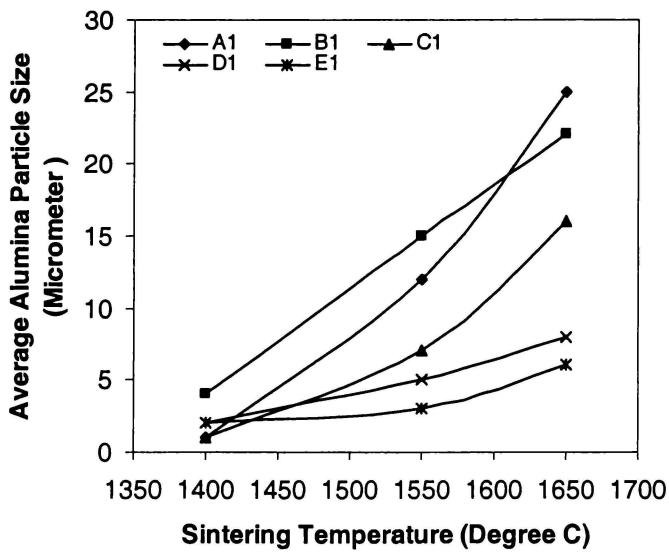

Fig. 4.23 Effect of sintering temperature on average Al_2O_3 particle size of α-Ti(Al,O) based composites.

After hipping, the average Al_2O_3 particle size in composites A1, B1, and C1 increased 2 to 6 μm for samples sintered at 1400°C and 3 to 7 μm for samples sintered at 1550°C. The average Al_2O_3 particle size increased only 1 to 2 μm after hipping Composites D1 and E1 sintered at 1400°C and 1550°C. The corresponding SEM images were shown in Figures 4.26 and 4.27. The reasons for the coarsening Al_2O_3 particles after hipping will be discussed in Section 4.4.

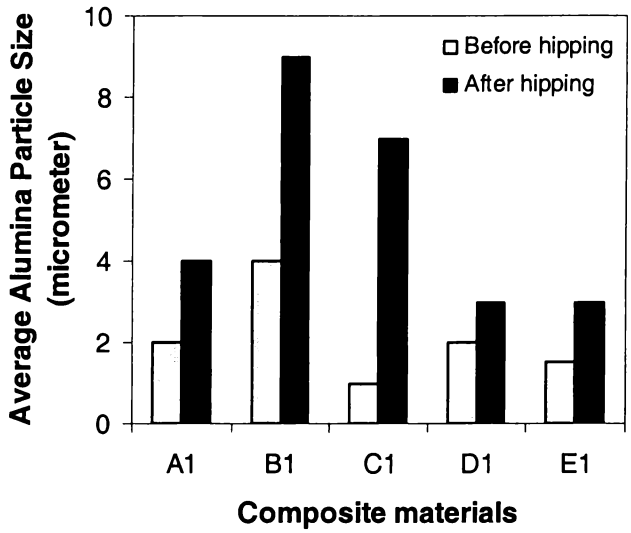

Figure 4.24 Effect of hipping on average Al_2O_3 particle size in the composites A1, B1, C1, D1, and E1 sintered at 1400°C.

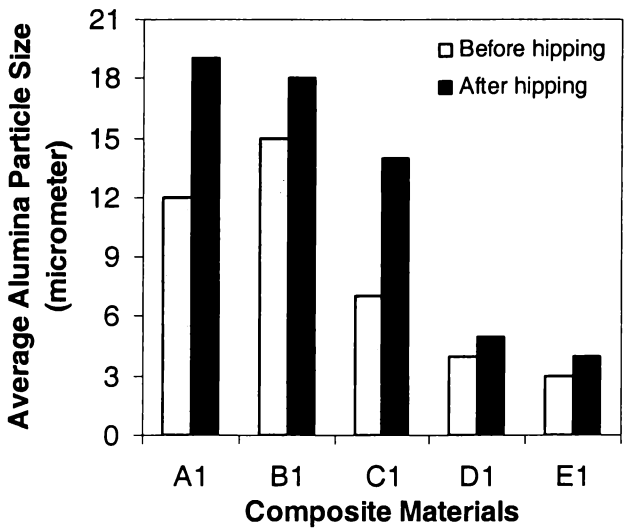

Figure 4.25 Effect of hipping on average Al_2O_3 particle size in the composites A1, B1, C1, D1, and E1 sintered at 1550°C.

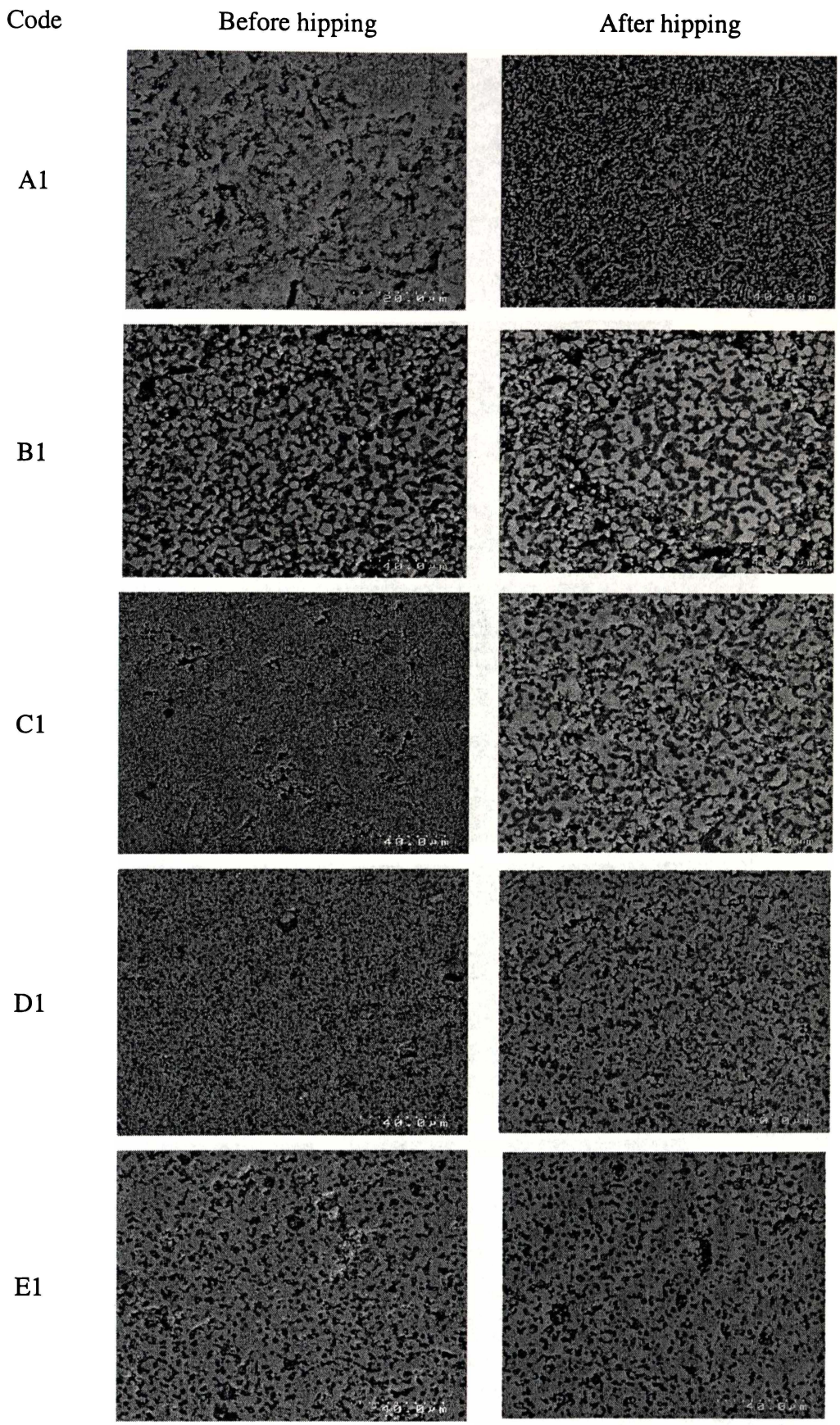

Figure 4.26 The SEM images of composites A1, B1, C1, D1, and E1 before and after hipping of the samples pre-sintering at 1400°C. (40μm).

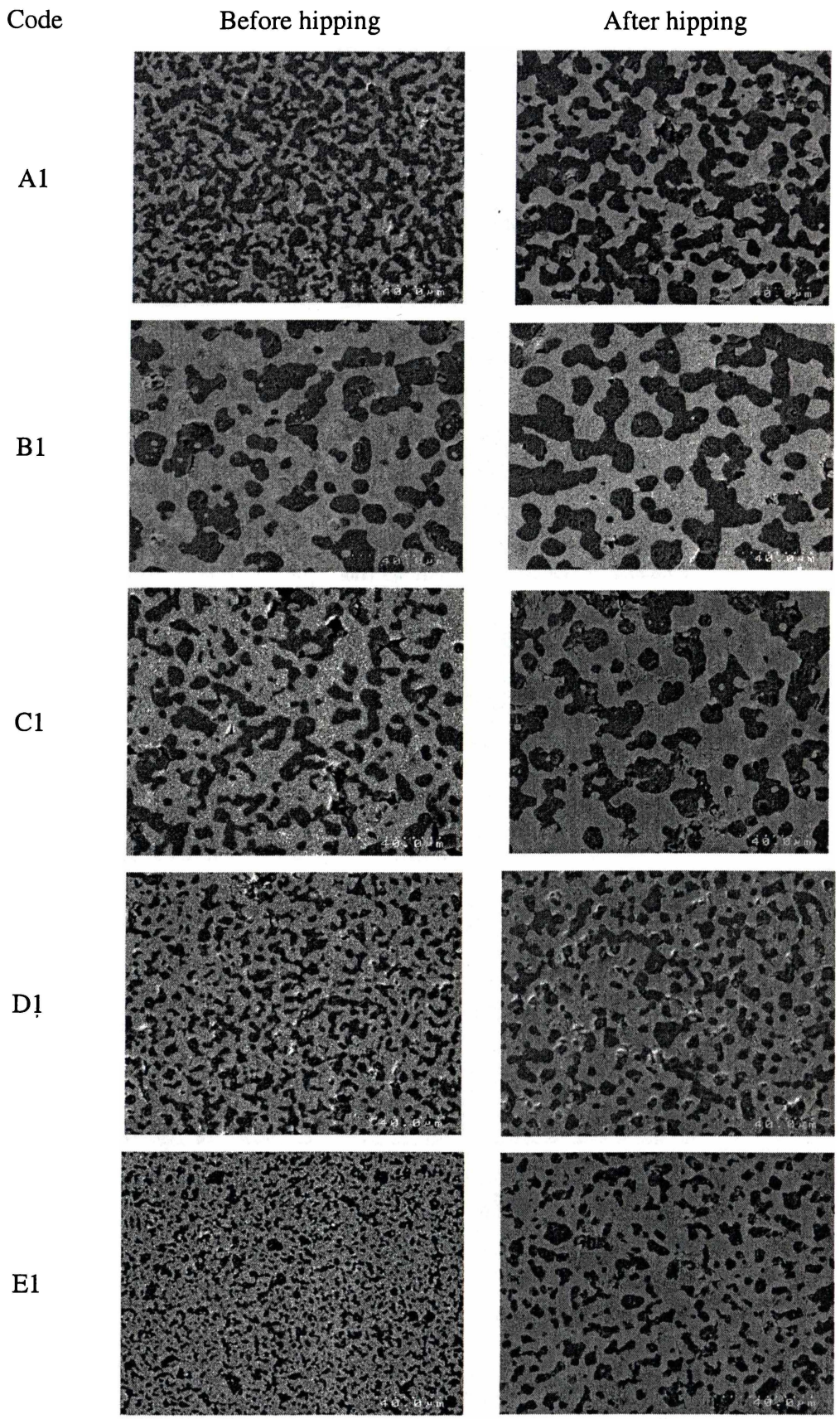

Figure 4.27 The SEM images of composites A1, B1, C1, D1, and E1 before and after hipping of the samples pre-sintered at 1550°C. (40μm).

The SEM image of composite A1 produced by directly hipping as-milled Al/TiO_2 composite powder sealed in a can at 1300°C for 2 hours under 200 MPa was shown in Figure 4.28. It shows that fully dense composite was produced under this condition. The Al_2O_3 particle size had on average 3-10 μm and were distributed along boundaries of the elongated grains of the Ti(Al,O) matrix. Figure 4.29 showed the SEM image of composite A1 produced by hipping the sample pre-sintered at 1300°C and with canning. The composite A1 produced using the latter condition appeared to have a different microstructure from that of composite A1 produced using the former condition. All the Al_2O_3 particles in composite A1 produced by latter condition had round shape and were uniformly distributed, and this microstructure was similar to the pressure-less sintered samples. The average Al_2O_3 particle size was in the range of 2-10μm.

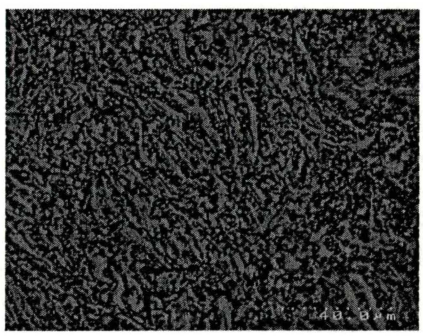

Figure 4.28 SEM image of composite A1 after hipping from as-milled powder with canning.

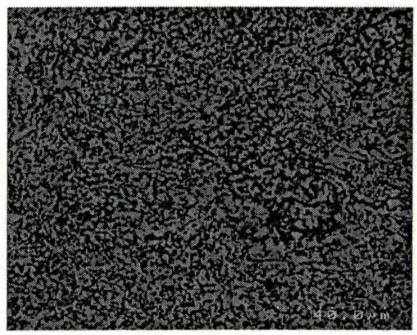

Figure 4.29 SEM image of composite A1 after hipping from the sample pre-sintering at 1300°C with canning.

The volume fraction of Al_2O_3 particles in composites A1, B1, C1, D1 and E1 was measured using image analysis from SEM images. The volume fraction of Al_2O_3 particles decreased in order from 58vol% for composite A1 to 37vol% for composite E1 (Figure 4.30).

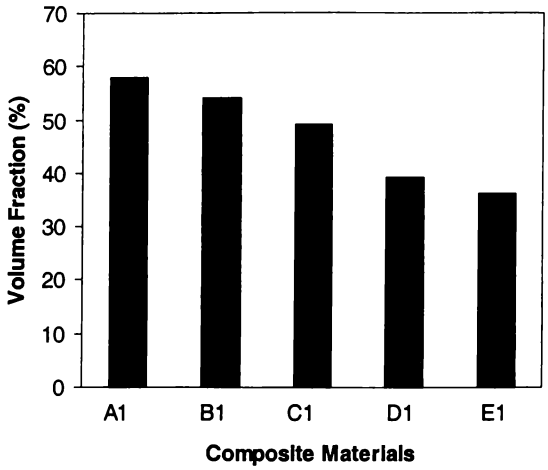

Figure 4.30 The volume fraction of Al_2O_3 particles in composites A1, B1, C1, D1 and E1.

4.3.2 Ti_3Al and $Al_2Ti_4C_2/Ti_3Al$ based composites

The effect of sintering temperature on microstructure of composites A2, B2, C2, D2 and E2 was shown in Figure 4.31. For composites A2, B2, and C2, the bright phase was Ti_3Al matrix and the dark phase was Al_2O_3 particles. For composites D2 and E2, the bright phase was $Al_2Ti_4C_2/Ti_3Al$ matrix and the dark phase was Al_2O_3 particles. There was insufficient contrast to distinguish TiC particles in composite E2. In composites A2, B2 and C2, the small Al_2O_3 particles were discretely distributed in the matrix after sintering at 1400°C. When the samples were sintered at 1550°C, the Al_2O_3 particles in composites A2 and B2 became an inter-connected net-work, while composite C2 had coarsened Al_2O_3 particles discretely distributed in the matrix. When these three composites were sintered at 1650°C, the Al_2O_3 particles were significantly coarsened. For composites D2 and E2, the coarsening of Al_2O_3 showed much independent of sintering temperatures at the range of 1400 to 1550°C. The large Al_2O_3 particles only appeared when the samples were sintered at 1650°C. The Al_2O_3 particles in composites D2 and E2 were discretely distributed in matrix and the distribution was independent of sintering temperature. The Al_2O_3 particles in composites A2, B2, and C2 coarsened with increasing sintering temperature, but the Al_2O_3 particle size in composites D2 and E2 did not change much. The reasons will be discussed in Section 4.4.

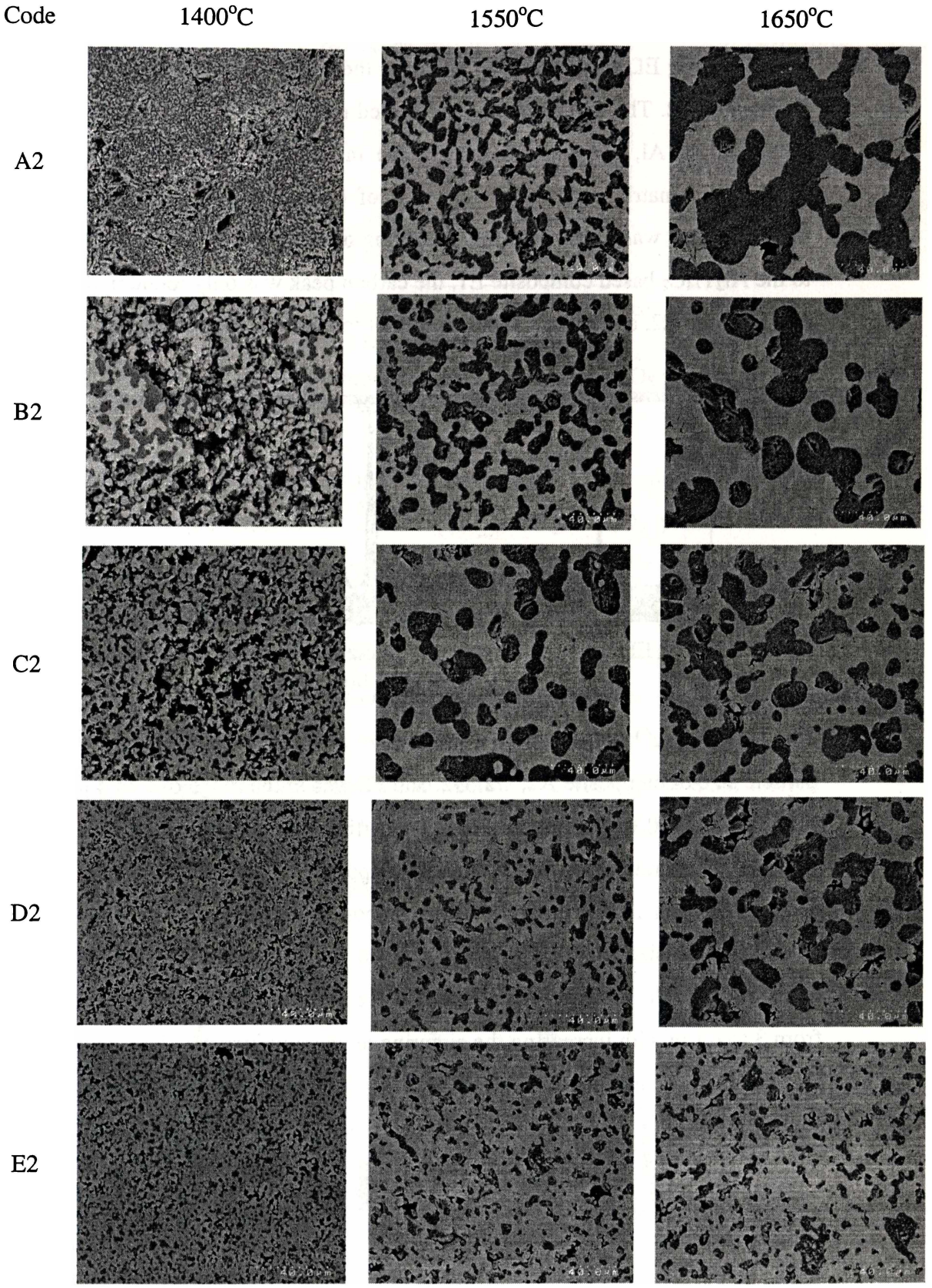

Figure 4.31 SEM images of composites A2, B2, C2, D2 and E2 produced by sintered at 1400°C, 1550°C, and 1650°C for 1 hour. (40μm)

The composition of the matrix and the particles was studied by performing analysis using EDX spectrometer fitted on the SEM, and the results were shown in Figure 4.32. The spectrum was performed on the matrix in composite A2 and only had Ti, Al, and oxygen peaks. The intensity of the aluminium peak in spectrum of matrix was higher than that of composite A1. This indicated that metallic phase was Ti_3Al with the dissolving of oxygen in composite A2. Similar to the $Al_2Ti_4C_2$ based composite E1, the carbon peak was only found in the matrix of composite E2, and carbon and Ti were not found in Al_2O_3 particles.

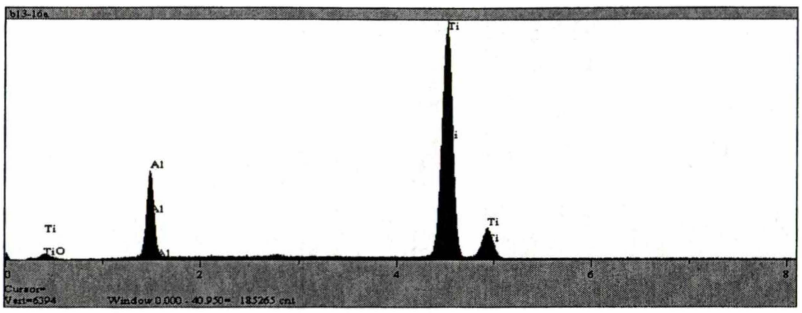

Figure 4.32 The EDX spectrum of matrix in composite A2 produced by sintered at 1650°C for 1 hour.

The average Al_2O_3 particle size of composite B2 was 6 μm. The average Al_2O_3 particle size of composite A2, C2, D2, and E2 was in the range of 2 to 4 μm after sintering at 1400°C (Figure 4.33). Al_2O_3 particle size increased with increasing sintering temperatures in all of these composites. The coarsening rates were accelerated from 1550°C to 1650°C for composites A2, B2, and D2. The average Al_2O_3 particle size in composite C2 showed linearly increasing with sintering temperatures. The average Al_2O_3 particle size in composite E2 only increased from 3 to 6 μm with increasing the sintering temperature from 1400°C to 1650°C. In general, the coarsening rate of the Al_2O_3 particles in composites D2 and E2 was significantly lower than that of the Al_2O_3 particles in composites A2, B2, C2.

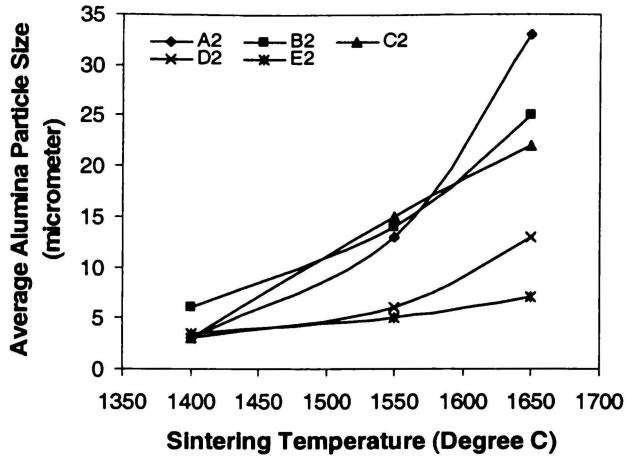

Figure 4.33 Effect of sintering temperature on the average Al_2O_3 particle size of composite A2, B2, C2, D2 and E2.

The average Al_2O_3 particle size in composite B2 increased about 4 μm after hipping samples pre-sintered at 1400°C. The average Al_2O_3 particle size in composites A2, C2, D2 and E2 only increased 1 or 2 μm after hipping (Figure 4.34a). For the samples produced by sintering at 1550°C, composite A2 shows the largest change of average Al_2O_3 particle size increased by hipping, which was 11 μm (Figure 4.34b). The average Al_2O_3 particle size in composites B2, C2, D2, and E2 only increased 2 to 4 μm after hipping. The reasons of the coarsening of Al_2O_3 particles after hipping will be discussed in Section 4.4. The typical SEM images of composites A2, B2, C2, D2 and E2 before and after hipping were shown in Figures. 4.35 and 4.36.

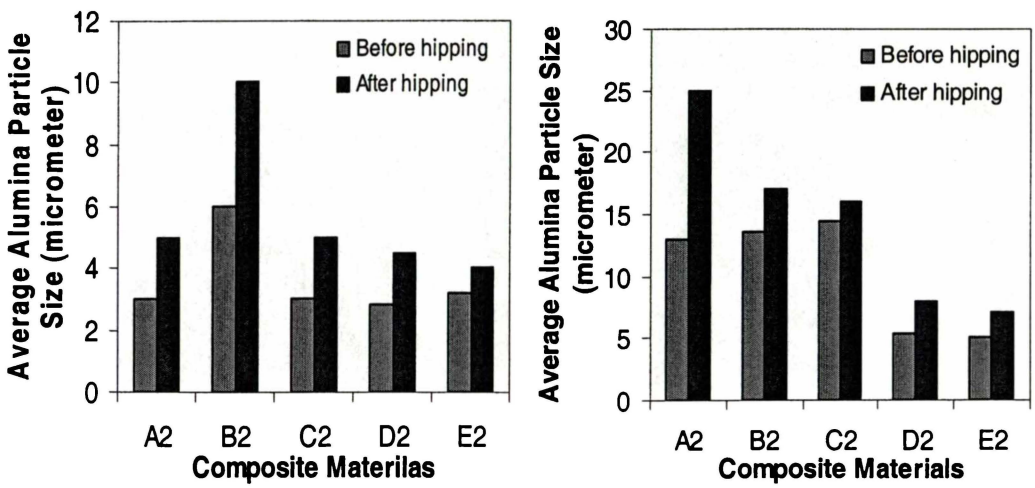

Figure 4.34 Average Al_2O_3 particle size in composites A2, B2, C2, D2 and E2 before and after hipping (a) pre-sintered at 1400°C and (b) pre-sintered at 1550°C.

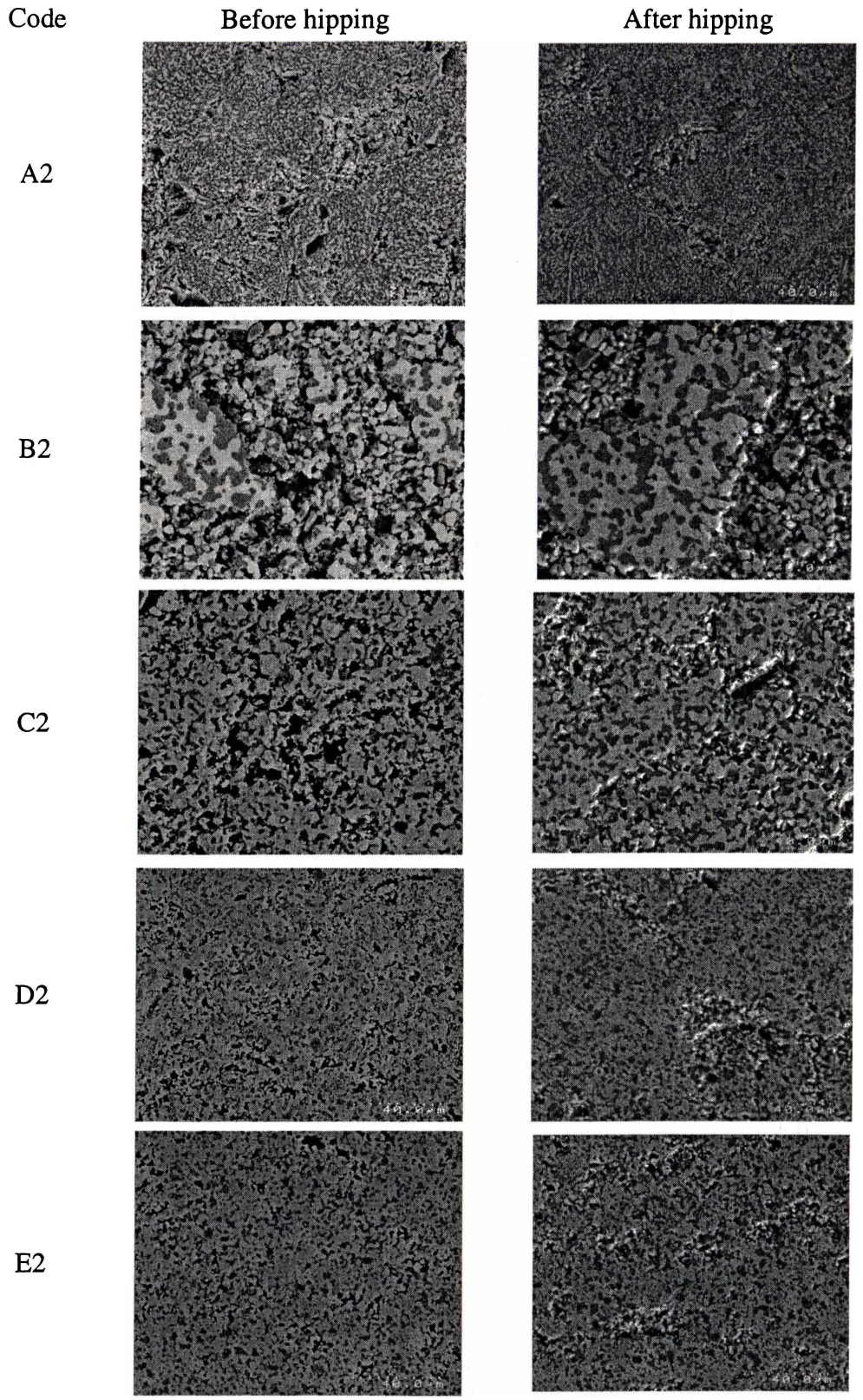

Figure 4.35 SEM images of composites A2, B2, C2, D2 and E2 before and after hipping samples pre-sintered at 1400°C for 1 hour. (40μm)

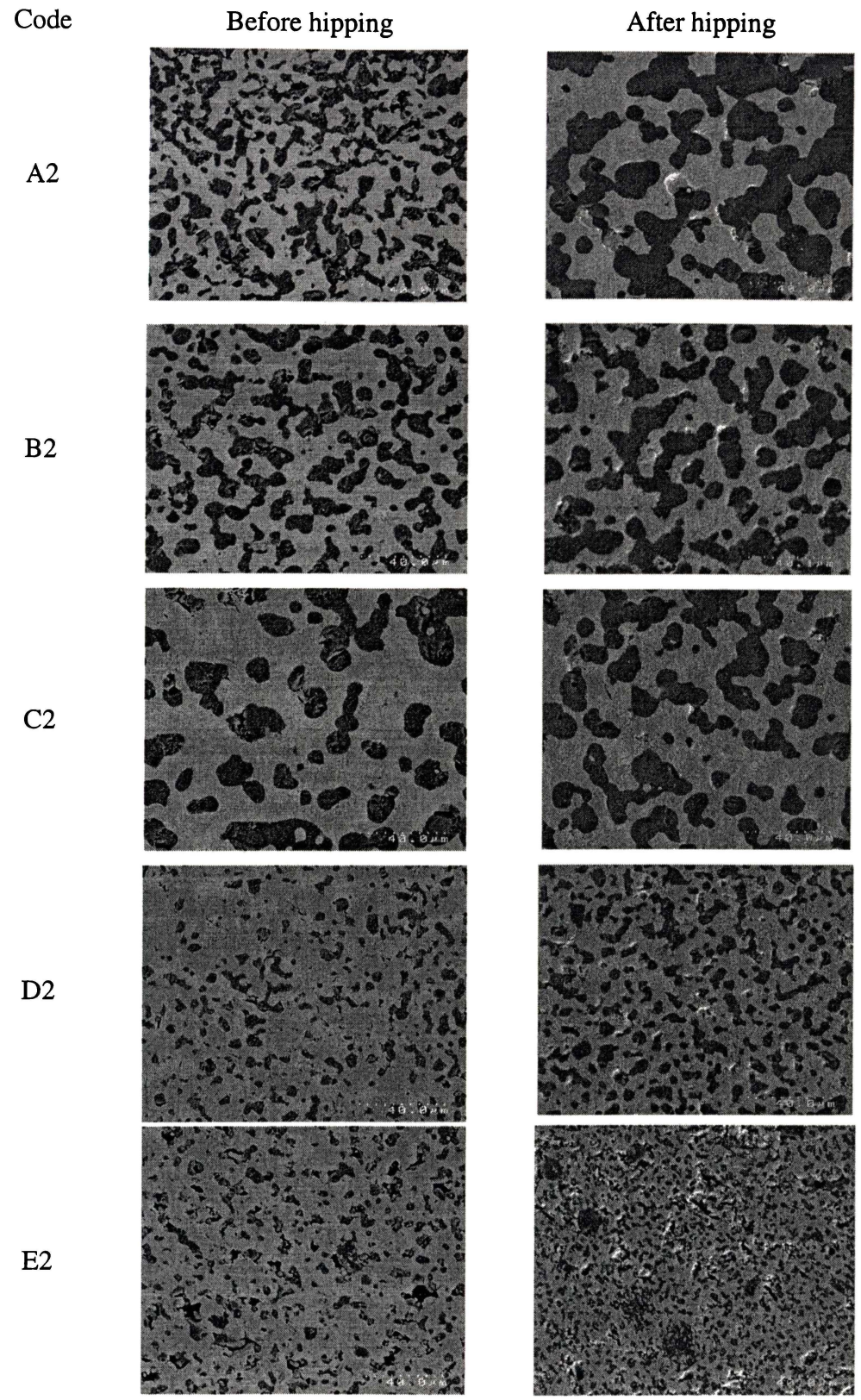

Figure 4.36 SEM images of composites A2, B2, C2, D2 and E2 before and after hipping samples pre-sintered at 1550°C for 1 hour. (40μm)

The results of the Al_2O_3 particle volume fraction of composites A2, B2, C2, D2 and E2 were shown in Figure 4.37. It shows that the volume fraction of Al_2O_3 was reduced from 56 to 35vol% from composite A2 to E2.

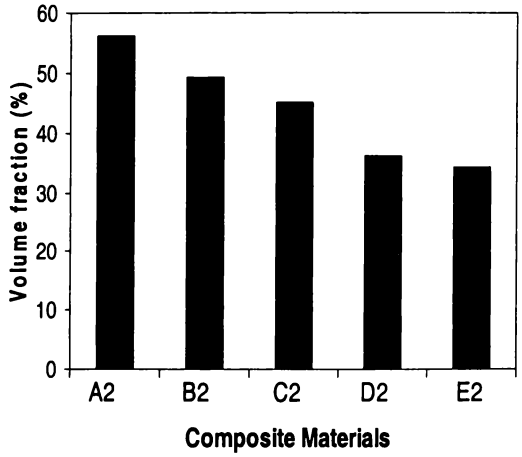

Figure 4.37 The volume fraction of Al_2O_3 particles in Ti_3Al and $Al_2Ti_4C_2$/ Ti_3Al based composites.

4.3.3 TiAl and $Al_2Ti_4C_2$/TiAl based composites

The typical SEM images of composites A3, B3, C3, D3, and E3 produced after sintering at 1400°C, 1550°C, and 1650°C for 1 hour were shown in Figure 4.38. The bright phase was TiAl matrix for composites A3, B3, and C3, and the dark phase was Al_2O_3 particles. For composites D3 and E3, the bright matrix was $Al_2Ti_4C_2$/TiAl, and the dark particles were Al_2O_3. There was insufficient contrast to distinguish TiC particles in composite E3. In composite A3, the Al_2O_3 particles inter-connected as a chain network after sintering at 1400 and 1550°C. When the samples were sintered at 1650°C, large Al_2O_3 particles grew by consuming small particles around forming elongated particles discretely distributed in TiAl matrix. For composites B3, C3, D3, and E3, the Al_2O_3 particles were more isolated. The particle shape was close to be round. The Al_2O_3 particles evenly distributed in matrix and Al_2O_3 particle size was independent of the sintering temperature. The Al_2O_3 particles in composites A3, B3 and C3 coarsened with increasing sintering temperature but Al_2O_3 particles in composites D3 and E3 did not change much. The reasons will be discussed in section 4.4.

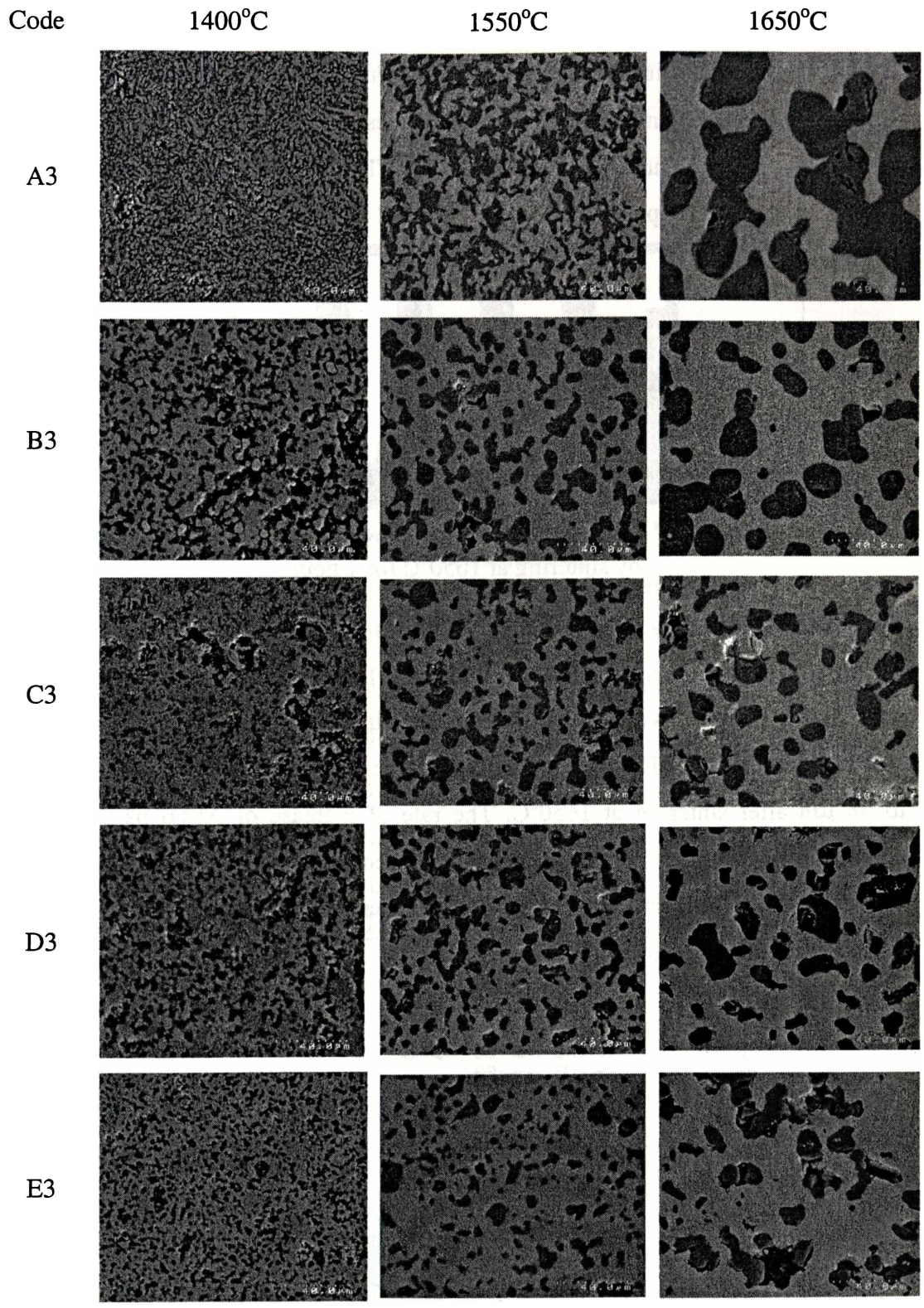

Figure 4.38 SEM images of composites A3, B3, C3, D3 and E3 obtained by pressure-less sintering at 1400°C, 1550°C and 1650°C. (40μm)

EDX data of composite A3 matrix only contained Ti, Al, and O peaks, confirming a TiAl based composite (Figure 4.39). The intensity of Al peak was higher than those of α-Ti(Al,O) and Ti_3Al based composites. It also suggested that the TiAl matrix has small amount of oxygen dissolving. The EDX spectrum for composite E3 was similar to composite E1 that only had Ti, Al and carbon peaks not shown.

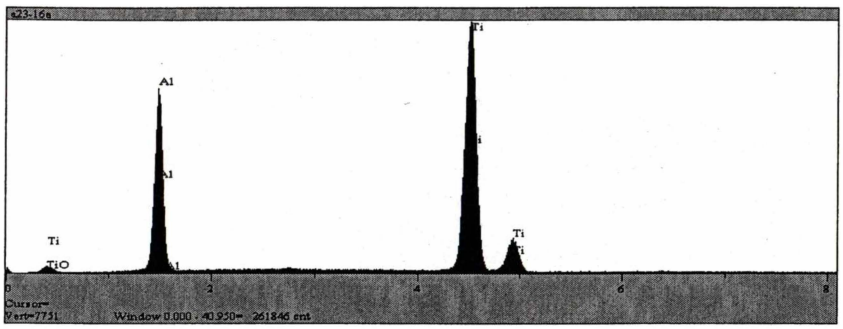

Figure 4.39 The EDX spectrum performed on matrix of composite A3 produced by sintering at 1650°C for 1 hour.

The average Al_2O_3 particle size in composites A3, B3, C3, D3 and E3 was measured by using image analysis (Figure 4.40). In general, the average Al_2O_3 particle size of these five composites increased almost linearly with increasing the sintering temperature. The average Al_2O_3 particle size of composite A3 increased to 38 μm after sintering at 1650°C. The rate of increase of Al_2O_3 particles in composite A3 with temperature accelerated when the sintering temperature was above 1550°C. The coarsening rates of Al_2O_3 particles in these five composites decreased in the order of composite A3 to E3.

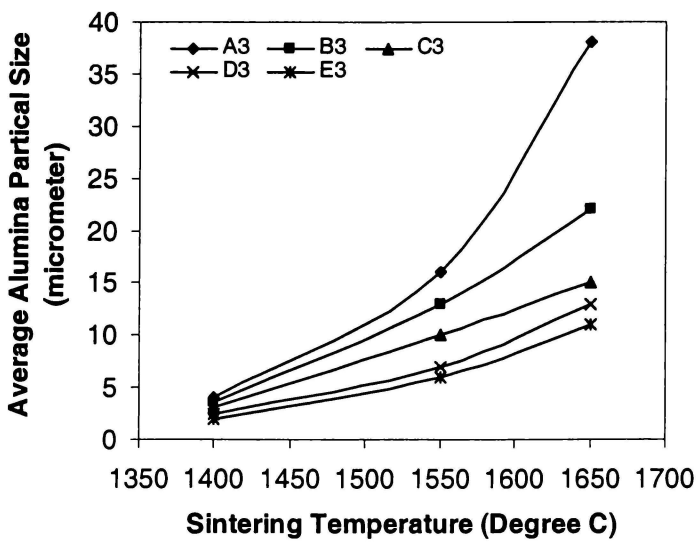

Figure 4.40 Effect of sintering temperature on average Al_2O_3 particle size of composites A3, B3, C3, D3, and E3.

The volume fraction of Al_2O_3 particles in composites A3 to E3 were shown in Figure 4.41. The volume fraction of Al_2O_3 particles reduced from 47 to 34 vol% from composite A3 to E3.

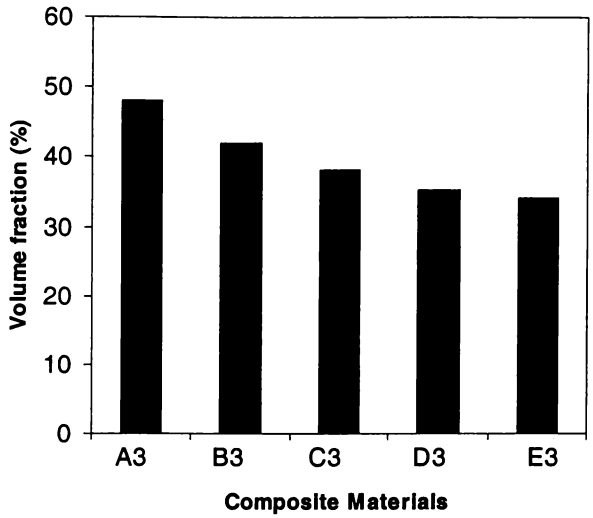

Figure 4.41 Al_2O_3 particles volume fraction in TiAl and $Al_2Ti_4C_2$ based composites

For the samples pre-sintered at 1400°C, the average Al_2O_3 particle size of these five composites were similar after hipping (Figure 4.42a) and only increased 0.5 or 1 μm. For the samples produced by sintering at 1550°C, the average Al_2O_3 particle size in composite A3 and C3 increased 7 or 9 μm after hipping. The average Al_2O_3 particle size of composites B3, D3, and E3 increased only about 2 to 3 μm after hipping. The typical microstructures of these composites are shown in Figures. 4.43 and 4.44. The reasons for the coarsening of Al_2O_3 particles will be discussed in Section 4.4.

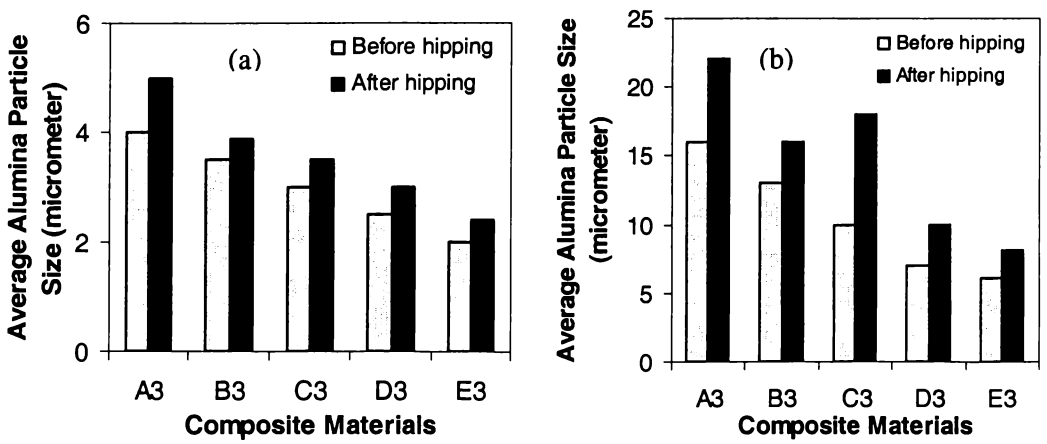

Figure 4.42 Average Al_2O_3 particle size in composites A3, B3, C3, D3 and E3 before and after hipping (a) pre-sintered at 1400°C and (b) pre-sintered at 1550°C.

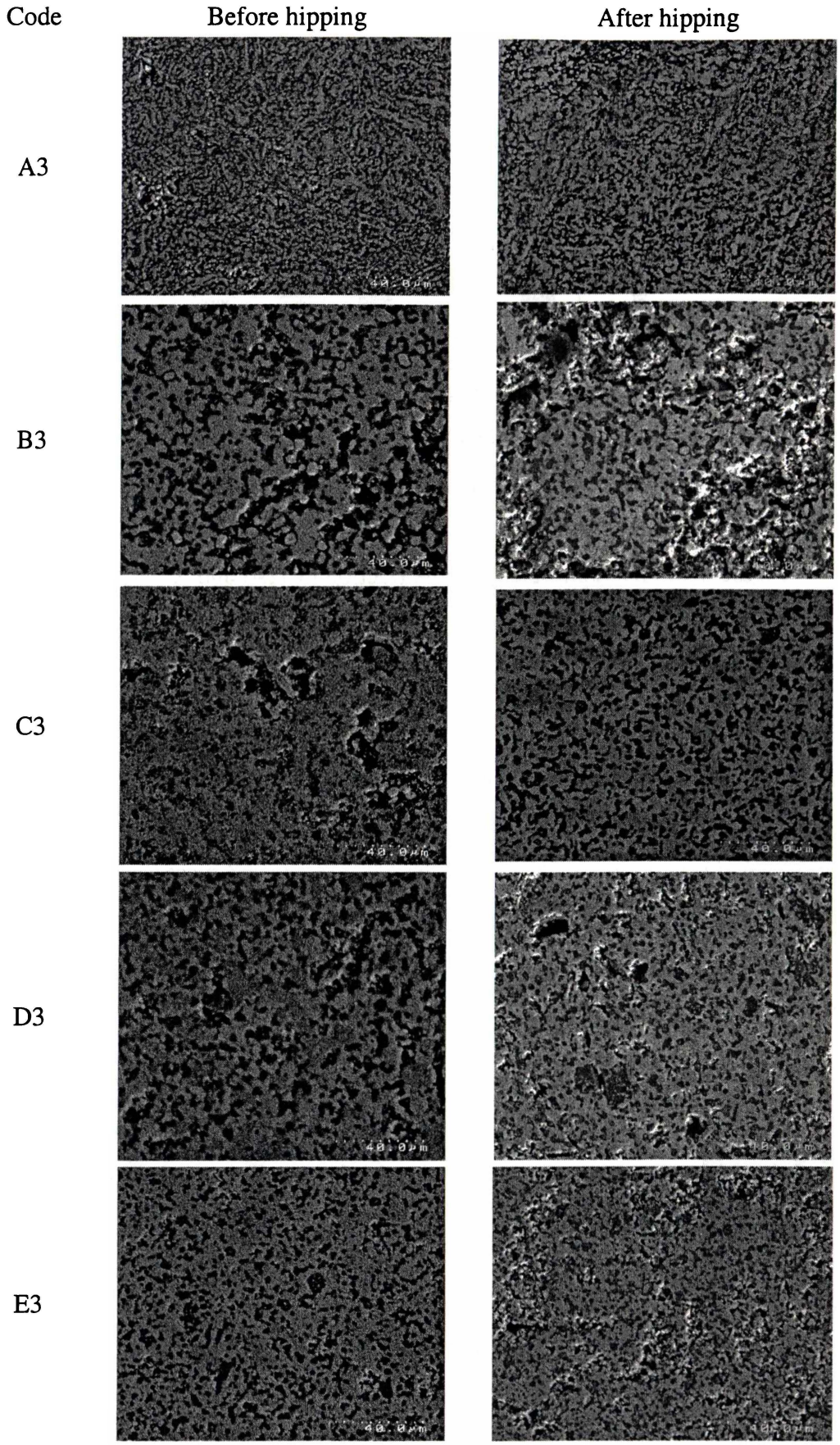

Figure 4.43 SEM images of composites A3, B3, C3, D3 and E3 before and after hipping of the samples pre-sintered at 1400°C for 1 hour. (40μm)

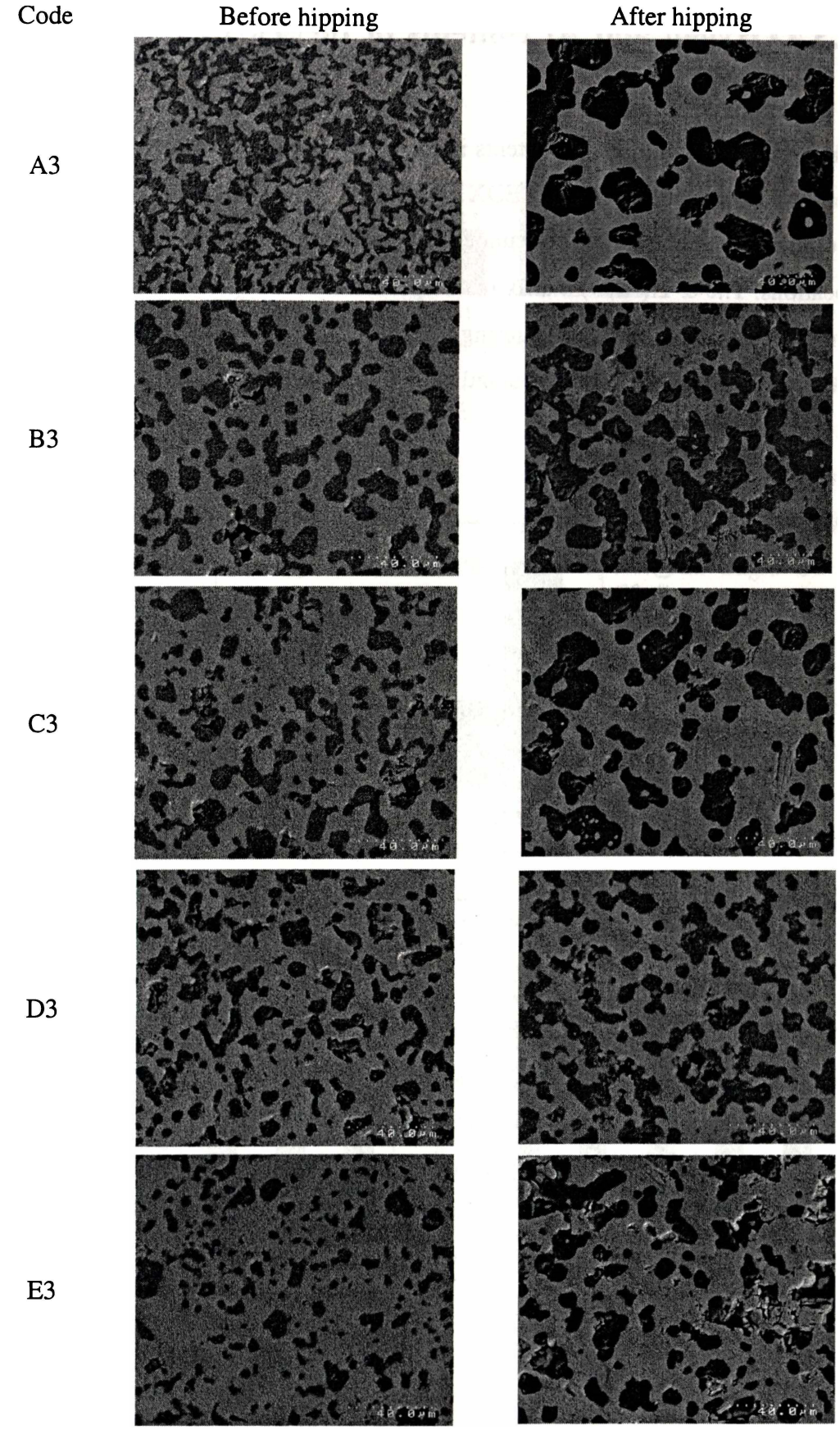

Figure 4.45 SEM images of composites A3, B3, C3, D3 and E3 before and after hipping of the samples pre-sintered at 1550°C. (40μm)

4.3.4 Oxygen and Al contents of the Ti_xAl_y and $Al_2Ti_4C_2$ phases

The oxygen and aluminum contents in the matrices of composites were measured semi-quantitatively using the EDX spectra of the matrices. The oxygen and aluminum contents were calculated by average values from five different locations. The α-Ti(Al,O) matrix in composite Al contained about 34 at% oxygen and 13 at% aluminum after sintering at 1550°C (Figure 4.46). When the samples were sintered at 1650°C, oxygen and aluminum contents reduced to 28 at% and 9 at% respectively.

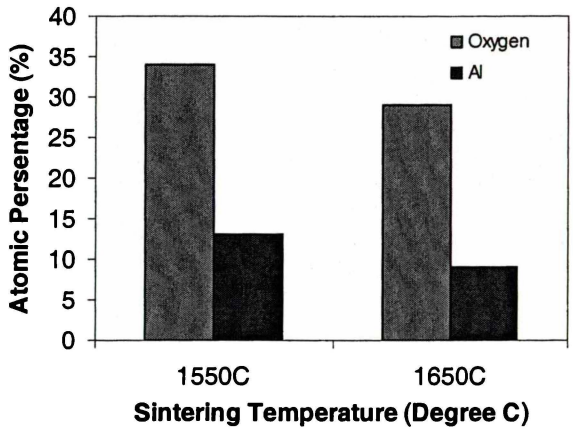

Figure 4.47 Effect of sintering temperature on oxygen and aluminum content in α-Ti(Al,O) of composite Al.

The oxygen content in the composite matrix decreased from 28 at% to 13 at% in the order composite A1 to C1 (Figure 4.47). In composites D1 and E1, the oxygen contents were 11 at% and 13 at% respectively. Data from TEM studies show that the $Al_2Ti_4C_2$ matrix phase of composite E1 has an average oxygen content of only 2.65 at%. The difference in oxygen content indicated by SEM and TEM may be because the electron beam of SEM is not narrow enough to focus only on $Al_2Ti_4C_2$ phase. Therefore, the TEM data is more accurate.

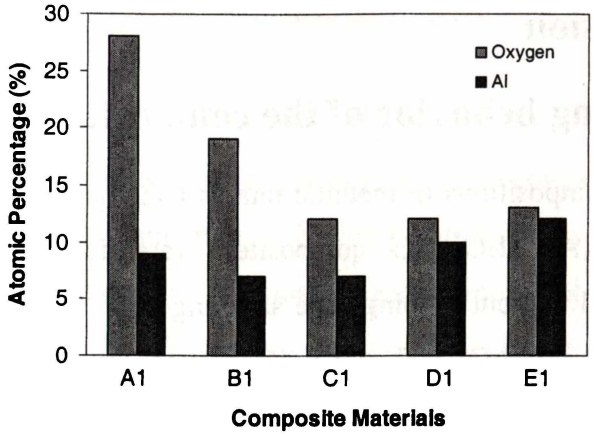

Figure 4.48 Oxygen and aluminum in α-Ti(Al,O) based composites Al, B1, C1, D1 and E1.

Oxygen content decreased from 19 at% in composite A2 to 8 at% in composite D2 (Figure 4.49). Composite E2 has an oxygen content of about 11 at%. However, the 11 at% oxygen in the matrix of composite E2 might be an overestimate of the oxygen in $Al_2Ti_4C_2$. The average oxygen content in the TiAl matrix of composites A3, B3, and C3 was lower than that of α-Ti(Al,O) and Ti_3Al based composites (Figure 4.50). The TiAl phase in composite A3 had the highest oxygen content about 4 at% and oxygen decreased to 2.3 at% in composite D3. The oxygen content in $Al_2Ti_4C_2$/TiAl matrix phases of composite E3 is similar to that of composite D3 (2.6 at%).

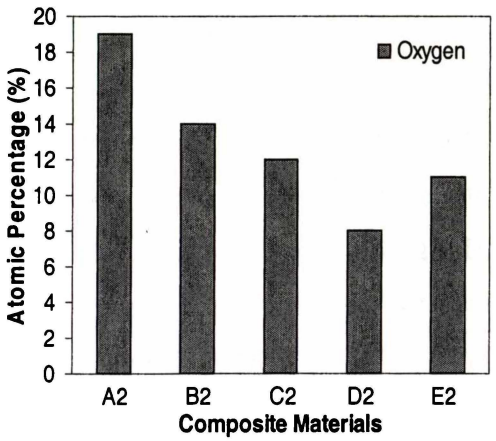

Figure 4.49 Oxygen content in the matrix phase of Ti_3Al and $Al_2Ti_4C_2$/Ti_3Al based composites.

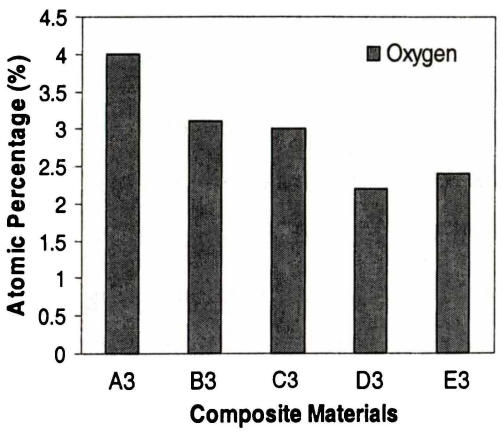

Figure 4.50 Oxygen content in metallic phase of TiAl and $Al_2Ti_4C_2$/TiAl based composite.

4.4 Discussion

4.4.1 Sintering behavior of the composites

Wide range of compositions in metallic phases and ceramic phases Ti_xAl_y/Al_2O_3 and $Al_2Ti_4C_2/Ti_xAl_y/Al_2O_3/TiC$ composites were fabricated using reaction sintering with and without hipping. The sintering behaviours of the Ti_xAl_y/Al_2O_3 and $Al_2Ti_4C_2/Ti_xAl_y/Al_2O_3/TiC$ composites were studied. Reaction kinetics between Al and TiO_2 have been examined in previous studies [2-5]. The phase formation of all these composites was discussed in Chapter Three. Changes of relative density and pore structure were used to study sintering behaviours. Apart from the pores in green compacted powder, pores can also be generated by reaction sintering due to density change between the reactants and the products [6-8]. In this study, by comparing the densities of reactants to products, the aluminum has a lower density than those of Ti_xAl_y, and Al_2O_3. This will cause the volume change of the composites after reaction. The decrease on volume after the reaction will create a pore structure in Ti_xAl_y based composites. Even though the reactions between Al and TiO_2, Ti_2O_3, or TiO_nC_{1-n} are highly exothermic, the samples showed little effect after being sintered at 1300°C and 1400°C and had 20% of porosity. This indicates that the exothermic heat was insufficient to sinter Al_2O_3 at 1300°C and 1400°C. The pores were mainly open and distributed in matrix phase of the composites.

To consolidate a composite, both the ceramic and metallic phases need to be consolidated. Normally a sintering temperature about 50% of its melting point (in Kelvin) of metals and about 80% of the melting point for ceramics is used [9]. There are two distinctive sintering temperatures for the metallic (or intermetallic) and ceramic phases of Ti_xAl_y/Al_2O_3 and $Al_2Ti_4C_2/Ti_xAl_y/Al_2O_3/TiC$ composites. Sintering temperatures for Ti_xAl_y phases are relative low because the melting point of Ti, Ti_3Al and TiAl are 1670°C, 1600°C and 1540°C respectively. On the other hand, Al_2O_3, $Al_2Ti_4C_2$ and TiC have melting points over 2300°C.

When sintering temperature was increased to 1550°C, the data show that most metallic phases in these composites were well sintered indicating that the mass diffusion rates of Ti_xAl_y are very high at this temperature. The pores exist mainly

in the Al_2O_3 particles. The Al_2O_3 particles were not sintered enough to produce a fully dense composite.

When sintering temperature was increased to 1650°C, all composites had densities of 94-96% indicating better sintering at this temperature. Pores were eliminated in most of the Al_2O_3 particles, and the pores present were at the interfaces of the matrix and Al_2O_3 particles. These may be caused by argon gas trapped in the pores. The microstructure indicates that the diffusion rate at 1650°C is high enough to cause extensive sintering of the Al_2O_3 phase, but 1550°C is too low for sintering Al_2O_3.

The sintering study indicates that adjusting sintering temperature to obtain fully dense composites is effective only if the mass diffusion rates of all phases are similar. In this study, 1650°C was the effective pressure-less sintering temperature for Ti_xAl_y/Al_2O_3 and $Al_2Ti_4C_2/Ti_xAl_y/Al_2O_3/TiC$ composites. An alternative method is to use a sintering additive, which adjusts the sintering temperature of some phases in the composite [10].

As expected, hipping without canning affected only on the closed pores. If there is a large fraction of open pores, density improvement is limited. If samples are canning fully dense samples can be obtained at low sintering temperatures (1300°C) from both as-milled powders and pre-sintered samples. Fully dense $TiAl/Al_2O_3$ composite can be obtained using hot pressing at 950°C [11].

4.4.2 Effect of sintering temperature on microstructure

The microstructure of the composites was characterized by size, shape and distribution of Al_2O_3 particles. Fine Al_2O_3 particles form immediately after the reactions between Al and TiO_2, Ti_2O_3, or TiO_nC_{1-n}. Later, high temperature sintering coarsens these particles. The Al_2O_3 particles exhibit different coarsening rates depends on the matrices used:

- Coarsening rate increases in the order α-Ti(Al,O), Ti_3Al and TiAl.
- Coarsening rate of Al_2O_3 particles in $Al_2Ti_4C_2$ based composites is significantly less than that in the Ti_xAl_y based composites.

- Coarsening rate increases with sintering temperature.
- Coarsening rate decreases as volume fraction of Al_2O_3 particles decreases.

The Al_2O_3 coarsening is controlled by the diffusion rates of oxygen and Al in the matrix and the equilibrium content of oxygen and aluminum in the matrix. Coarsening is achieved through dissolving small Al_2O_3 particles and growing the large Al_2O_3 particles. Higher oxygen content in the matrix helps diffusion of the oxygen atoms. Therefore, α-Ti(Al,O) based composites should have a higher Al_2O_3 particle coarsening rate than Ti_3Al, and TiAl based composites. However, it was observed that Al_2O_3 particles coarsened more quickly in Ti_3Al and TiAl based composites. Indicated that the melting point of the matrix has a dominant effect on the coarsening rate. When the sintering temperature is 1650°C, Ti_3Al becomes partially liquid and TiAl becomes fully liquid. The oxygen and Al can more easily diffuse in the liquid phase. The lower oxygen content and the high melting point of $Al_2Ti_4C_2$ means that oxygen and aluminum mobility in the $Al_2Ti_4C_2$ matrix is likely to be significantly lower than that in the Ti_xAl_y matrices. This leads to a much lower Al_2O_3 coarsening rate in $Al_2Ti_4C_2$ based composites when the sintering temperature is 1650°C or lower.

The increase of coarsening rate of Al_2O_3 particles with sintering temperature can be explained as the increase in Al and oxygen diffusion rates with temperature. The coarsening rate of Al_2O_3 particles decreases with decreased volume fraction of Al_2O_3 particles because the distance between individual Al_2O_3 particles is increasing. As the Al_2O_3 volume fraction increases, the distance between Al_2O_3 particles decrease making consumption of small particles easier.

4.4.3 Effect of hipping on microstructure

The Al_2O_3 particles in the composites coarsened after hipping. The coarsening rate in the Ti_xAl_y/Al_2O_3 composites is higher than that in $Al_2Ti_4C_2/Ti_xAl_y/Al_2O_3/TiC$ composites. Samples pre-sintered at 1400°C have high porosity. Applying pressure compacts the particles and increases the contact surface area between particles. This increases the ability of Al_2O_3 particles to grow. Other study reported that grain growth is accelerated by high pressure [12]. When the pressure is applied to samples pre-sintered at 1550°C and with > 92%

relative density, an oxygen concentration gradient is created. This oxygen gradient increases oxygen diffusion rates and therefore the coarsening rate of Al_2O_3 [13].

4.5 Summary

The matrices of Ti_xAl_y/Al_2O_3 and $Al_2Ti_4C_2/Ti_xAl_y/Al_2O_3/TiC$ composites become fully dense after sintering at 1550°C. The Al_2O_3 particles became fully sintered when the composites are sintered at 1650°C; 1550°C is not high enough for sintering. The Al_2O_3 particles in the α-Ti(Al,O) and Ti_3Al and based composites have a high coarsening rate above 1550°C, indicating that oxygen and Al diffusion rates of in α-Ti(Al,O) and Ti_3Al are very high at these temperatures. The Al_2O_3 particles in TiAl based composites also have a high coarsening rate at temperatures above 1550°C because TiAl melts. This study also found that Al_2O_3 particles in the $Al_2Ti_4C_2/Ti_xAl_y/Al_2O_3/TiC$ based composites have a much lower coarsening rate due to the $Al_2Ti_4C_2$ matrix having a lower oxygen content and higher melting point, which reduces the mobility of oxygen and aluminum.

References

1. JCPDS- International Centre for Diffraction Data (1995).
2. Zhihong Cai, Deliang Zhang, Aijun Huang and Rui Yang, unpublish work.
3. Z.A. Munir and U. Anselmi-Tamburini, Materials Science Reports **3**, 277-365, (1989).
4. S.P. Gaus, M.P. Haemer, H.M. Chan, H.S. Caram, N. Claussen, J. Am. Ceram. Soc., **83**, 1599-1605, (2000).
5. S.P. Gaus, M.P. Haemer, H.M. Chan, H.S. Caram, J. Bruhn, N. Claussen, J. Am. Ceram. Soc., **83**, 1606-1612, (2000).
6. N.J. Welham, Materials Science and Engineering, **A255**, 81-89, (1998).
7. A. Bose, B.H. Rabin, R.M. German, Powder Mat. Intern., **20**, 25-30, (1988).
8. Y.M. Chiang, D.P. Dirnie, W.D. Kingery, Physical Ceramic, J. Wiley, New York, (1997).
9. P.E. Bebely, E. Barringer, H.K. Bowen, J. Amer. Ceram. Soc., **68**, 76-78, (1985).
10. L.M. Zhang, R.Z. Yuan, M. Omori, and T. Hirai, in 3th Int. Symp. on 'Structureal and functional gradient materials', 59-64, Lausanne, Switzerland, ed. B. Ilschner and N. Cherradi (1994).
11. D. Horvitz, I. Gotman, E.Y. Gutmanas, N. Claussen, Journal of European Ceramic Society, **22**, 947-954, (2002).
12. J. Besson, M. Abouaf, Acta Met. Mater., **71**, 2225-2234, (1991).
13. P.G. Shewmon, Diffusion in Solid, Minerals, Metals & Materials Society, Warrendale, 32-42, (1989).

Chapter Five
Mechanical Properties of Ti_xAl_y/Al_2O_3 and $Al_2Ti_4C_2/Ti_xAl_y/Al_2O_3/TiC$ Composites

5.1 Introduction

The microstructure/processing relationships of the Ti_xAl_y/Al_2O_3 and $Al_2Ti_4C_2/Ti_xAl_y/Al_2O_3/TiC$ composites were discussed in Chapter Four. In this chapter, data on the mechanical properties of these composites such as hardness, bending strength and fracture toughness, are presented. The microstructure /property and composition/property relationships are discussed.

5.2 Hardness

Vicker's hardness was calculated using equation (2-2). Hardness of composites A1, B1, and C1 increased almost linearly as sintering temperature increased (Figure 5.1). The rate of increase was higher in pressure-less sintered samples than in samples produced by sintering followed by hipping. Hardness of composites decreased in the order composite A1, B1, and C1 for samples pressure-less sintered or sintered then hipped. After sintering at 1550°C, composite A1 had a hardness value of 1220 VHN, while composites B1 and C1 had much lower hardness value of 790 and 620 VHN respectively. After sintering at 1650°C, hardness of composite A1 increased to 1580 VHN while hardness of composites B1 and C1 increased to 1030 and 810 VHN respectively. Hipping increased the hardness of the three composites pre-sintered at 1550°C by about 10%. However, hipping had very little effect on the hardness of samples pre-sintered at 1650°C.

Hardness of composites D1 and E1 increased almost linearly with sintering temperature (Figure 5.2). Hardness of composite E1 was significantly higher than that of composite D1. Hipping increased hardness of composites D1 and E1 by 2 to 5%.

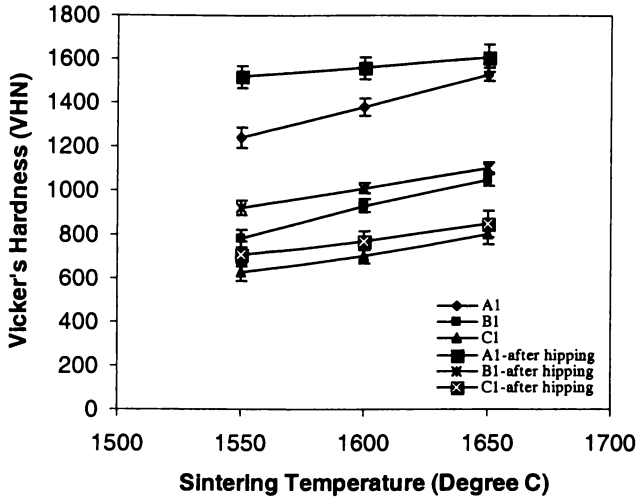

Figure 5.1 Vicker's hardness of α-Ti(Al,O) based composites A1, B1, and C1 before and after hipping as a function of pressure-less sintering temperature.

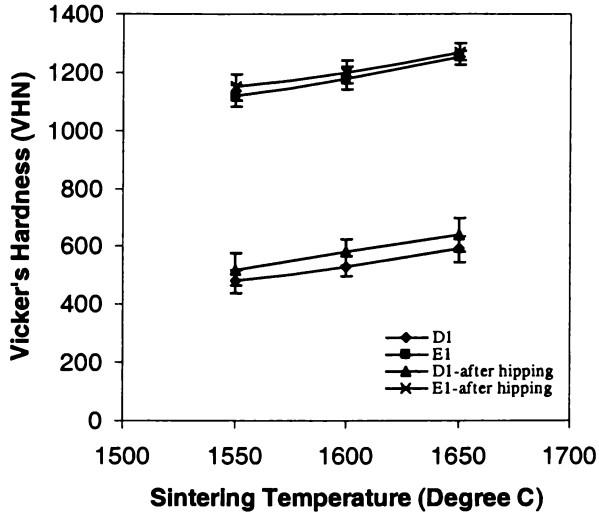

Figure 5.2 Vicker's hardness of $Al_2Ti_4C_2$ based composites D1 and E1 before and after hipping as a function of pressure-less sintering temperatures.

Hardness of composites A2, B2, and C2 increased linearly as sintering temperature increased. The rate of increase was greater in pressure-less sintered samples than in samples sintered then hipped (Figure 5.3). Hardness of composites decreased in the order composite A2, B2 and C2 for both of pressure-less sintered samples and samples sintered then hipped. Hardness of the composites produced by sintering and hipping also increased as a function of pre-sintering temperature but the magnitude of the increase was significantly smaller than for composites not hipped. For hipping samples pre-sintered at 1550°C, hardness increased by 10 to 18%. For hipping samples pre-sintered at 1650°C, hardness increased by only 2 to 5%.

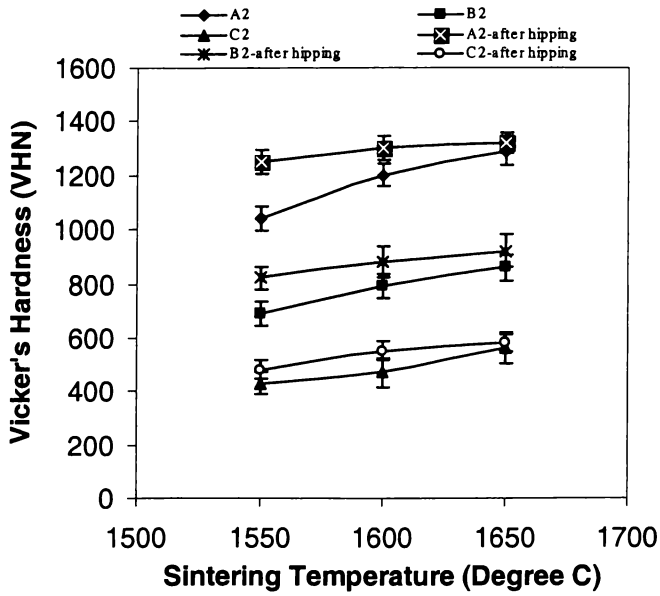

Figure 5.3 Vicker's hardness of Ti_3Al based composites A2, B2, and C2 before and after hipping as a function of pressure-less sintering temperature.

Hardness of composite E2 is significantly higher than the hardness of composite D2 (Figure 5.4). Hardness of composite E2 increased with sintering temperature. The increase was greater when temperature was increased from 1550 to 1600°C than when temperature was increased from 1600 to 1650°C. The hardness of composite D2 was almost independent of the sintering temperature in the range 1550-1650°C for both the samples with or without hipping. Hipping increased hardness of the two composites slightly (1-4%).

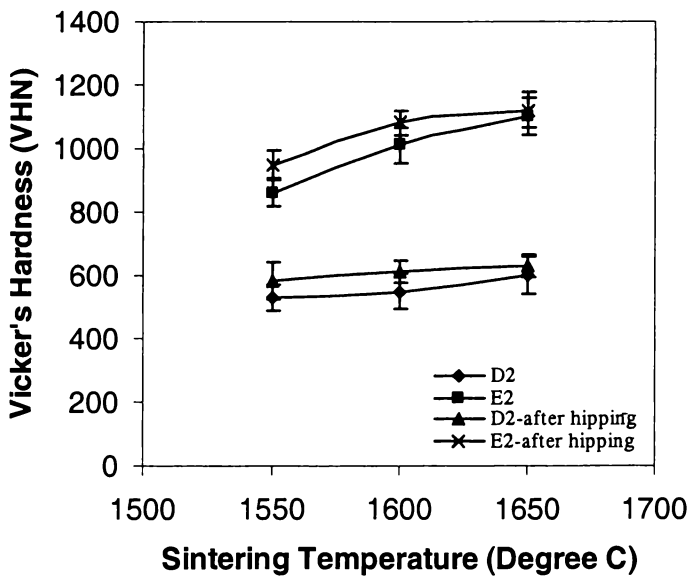

Figure 5.4 Vicker's hardness of $Al_2Ti_4C_2/Ti_3Al$ based composites D2 and E2 before and after hipping as a function of the pressure-less sintering temperatures.

Hardness of pressure-less sintered composites increased linearly with sintering temperature (Figure 5.5). The increase in hardness with sintering temperature was greater over the temperature range 1550-1600°C than the temperature range 1600-1650°C. Hardness of composites decreased in the order composite A3, B3, and C3 for both the samples with or without hipping. Hardness of composite C3 produced by sintering and followed by hipping was almost independent of pre-sintering temperature while hardness of composites A3 and B3 increased substantially in the temperature range 1550-1600°C and then stopped increasing. For a given pre-sintering temperature, hipping increased in hardness by 2-8%.

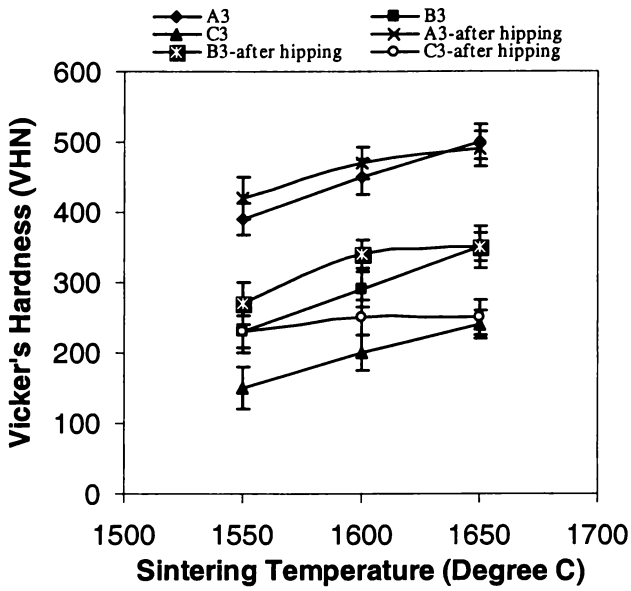

Figure 5.5 Vicker's hardness of TiAl based composites A3, B3, and C3 before and after hipping as a function of the pressure-less sintering temperature.

Composite E3 was significantly harder than composite D3 (Figure 5.6). Hardness of pressure-less sintered composites D3 and E3 increased almost linearly with sintering temperature while hardness of composites D3 and E3 produced by sintering and followed by hipping was almost independent of pre-sintering temperature. Hipping had little effect on hardness of the two composites.

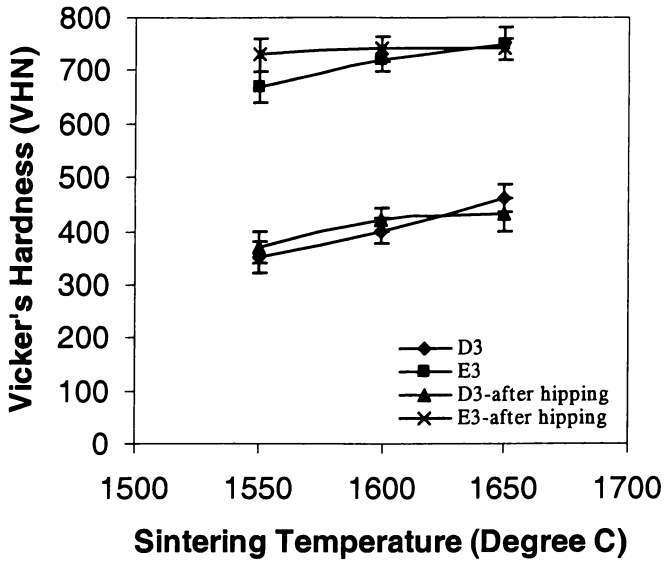

Figure 5.6 Vicker's hardness of $Al_2Ti_4C_2$/TiAl based composites D3 and E3 before and after hipping as a function of the pressure-less sintering temperatures.

5.3 Bending strength of the composites

The composites produced in this study are brittle so the fracture strength was measured by performing flexure tests using 3-point bending (equation 2-4). Bending strength of the pressure-less sintered A1, B1 and C1 samples decreased almost linearly with sintering temperature (Figure 5.7). For a given temperature, bending strength of composites increased in the order composite A1, B1, to C1. For samples after hipping, bending strength of composites decreased as pre-sintering temperature increased from 1550°C to 1650°C but the magnitude of decrease was higher than the composites without hipping. This was because hipping causes a greater amount of increase in bending strength of the samples pre-sintered at a lower temperature than that of the samples pre-sintered at a higher temperature. With the sintering temperature being 1550°C, hipping caused the bending strength of composites A1, B1, and C1 to increase by 24 to 30%. For the samples pre-sintered at 1650°C, hipping had almost no effect on bending strength.

Bending strength of composites D1 and E1 produced by pressure-less sintering decreased almost linearly with temperature (Figure 5.8). Hipping decreased bend strength more rapidly over the temperature range 1550-1600°C than in the temperature range 1600-1650°C. Hipping increased bending strength of

composites D1 and E1 pre-sintered at 1550°C by about 10%. However, hipping had little effect on the bending strength of samples pre-sintered at 1650°C.

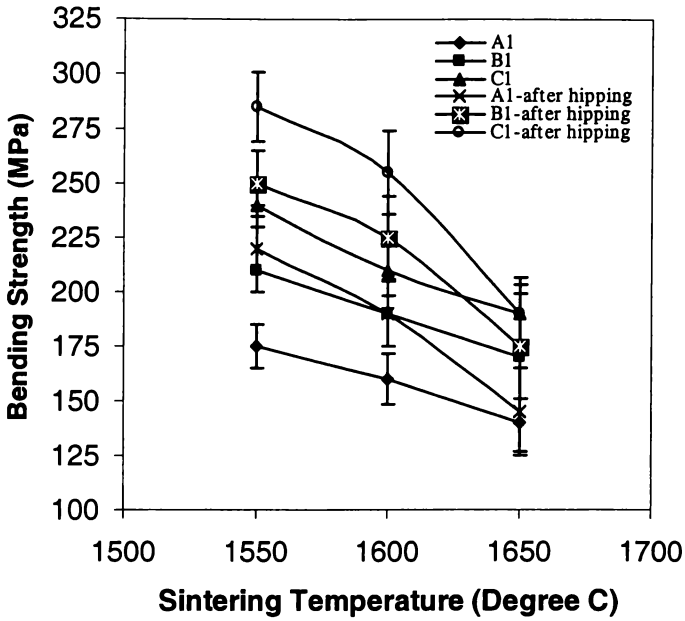

Figure 5.7 Bending strength of α-Ti(Al,O) based composites A1, B1, and C1 before and after hipping as a function of sintering temperatures.

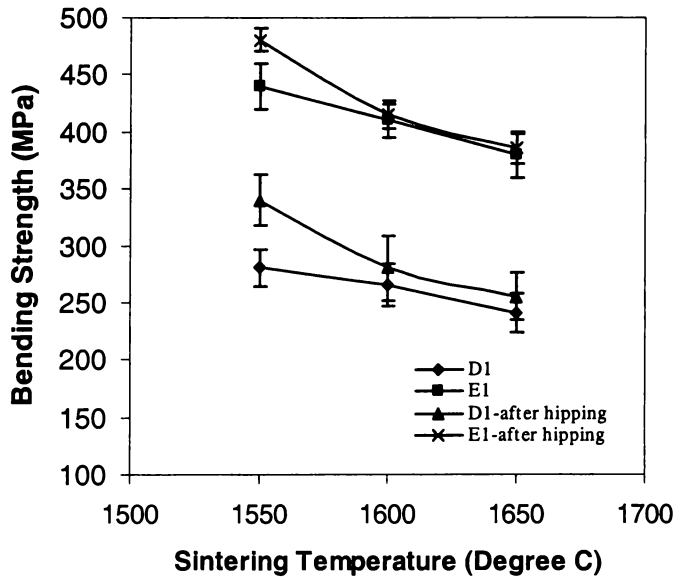

Figure 5.8 Bending strength of $Al_2Ti_4C_2$ based composites D1 and E1 before and after hipping as a function of sintering temperatures.

Maximum bending strength of composites A2, B2 and C2 were 155, 165 and 190 MPa respectively sintered at 1600°C (Figure 5.9). If samples were sintered at 1650°C, bending strength of composite A2 decreased to 95 MPa and those of composites B2 and C2 decreased to 150 and 180 MPa respectively. If the samples

were hipped after sintering, bending strength decreased as pre-sintering temperature increased. The magnitude of decrease was higher for hipped samples.

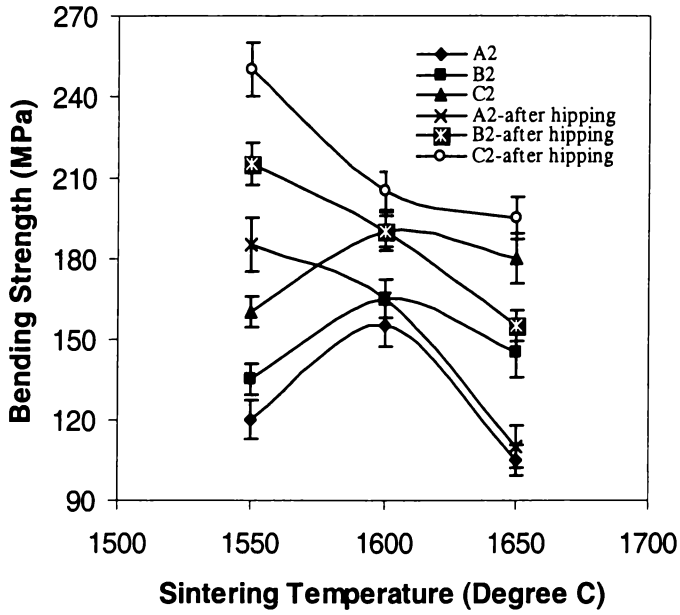

Figure 5.9 Bending strength of Ti_3Al based composites A2, B2, and C2 before and after hipping as a function of the sintering temperature.

Bending strength of composites D2 and E2 whether produced by pressure-less sintering or by sintering followed by hipping decreased almost linearly with temperature (Figure 5.10). Hipping increased bending strength of composites D2 and E2 pre-sintered at 1550°C by 6-9%. Hipping had little effect on the bending strength of samples pre-sintered at 1650°C.

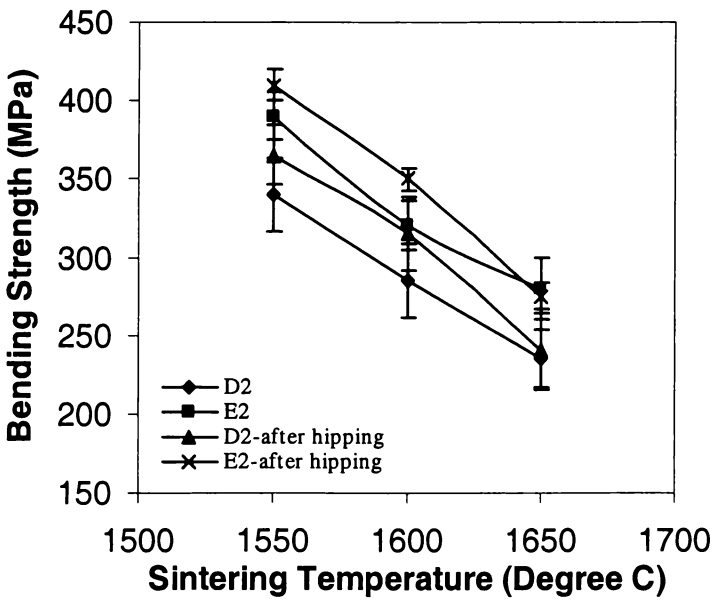

Figure 5.10 Bending strength of $Al_2Ti_4C_2/Ti_3Al$ based composites D2 and E2 before and after hipping as a function of the sintering temperature.

Bending strengths of composite A3, B3 and C3 sintered at 1600°C had maximum values of 155, 185 and 220 MPa respectively. Bending strength increased in the order of composites A3, B3, and C3. Bending strength of pressure-less sintered composite A3 was nearly independent of sintering temperature but bending strength of composites B3 and C3 decreased slightly with increasing temperature. Hipping the samples decreased bending strength of composites as the pre-sintering temperature increased from 1550°C to 1650°C. This was because hipping caused a greater amount of increase in bending strength for samples pre-sintered at a lower temperature than that of the samples pre-sintered at a higher temperature. Hipping samples pre-sintered at 1550°C, increased bending strength of composites A3, B3 and C3 by 5-15%.

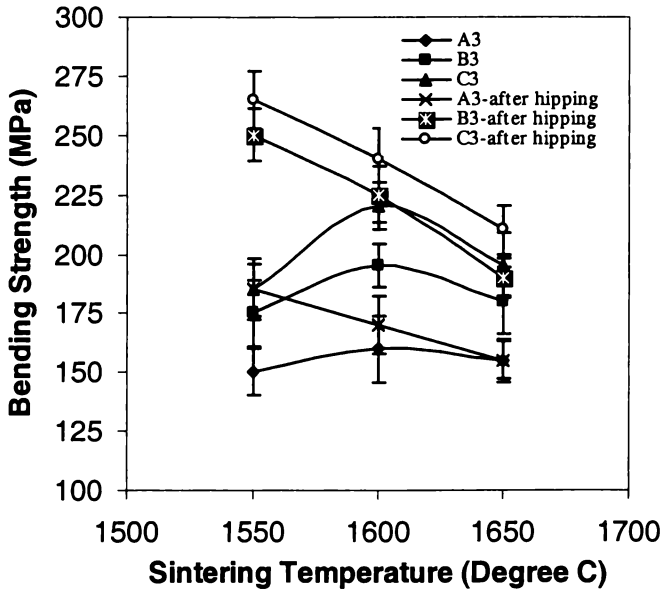

Figure 5.11 Bending strength of TiAl based composites A3, B3, and C3 before and after hipping as a function of the sintering temperature.

Bending strength of composites D3 and E3 increased with increasing sintering temperature up to 1600°C (Figure 5.12). Bending strength of composites decreased when the sintering temperature was further increased to 1650°C. Bending strength decreased almost linearly with increase in pre-sintering temperature from 1550°C to 1650°C. Bending strength of composites D3 and E3 increased by 40 and 36% respectively after hipping of the samples pre-sintered at 1550°C. For the samples pre-sintered at 1650°C, hipping had very little effect on the bending strength of composite D3, but increased bending strength of the composite E3 by about 25%.

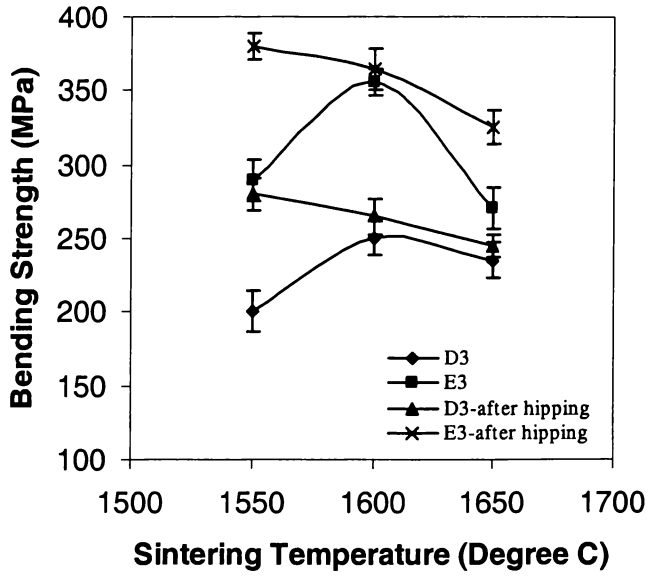

Figure 5.12 Bending strength of $Al_2Ti_4C_2$/TiAl based composites D3 and E3 before and after hipping as a function of sintering temperatures.

5.4 Fracture toughness

Vickers indentation technique was used to measure fracture toughness of the composites. Fracture toughness of the composites was calculated using equation 2-3. The limitation of this equation is crack length must be more than 2.5 times longer than the diagonal of the indent.

Table 5.1 Young's Modulus of materials used to calculate the fracture toughness of composite materials in this study.

Material	Young's modulus (GPa)	Reference
Ti	100	1
Ti_3Al	145	1
TiAl	175	1
TiC	379	2
$Al_2Ti_4C_2$	277	
Al_2O_3	390	2

Published values of Young's modulus for the materials and the rule of mixture were used to calculate fracture toughness of the composite materials in this study (Table 5.2). The Young's modulus of $Al_2Ti_4C_2$ was estimated from measurement because published values were not available. Error is calculated as half of the difference between the maximum and minimum values for each composite.

Table 5-2 Young's modulus of composites.

Name	Young's modulus (GPa)	Name	Young's modulus (GPa)	Name	Young's modulus (GPa)
A1	268	A2	282	A3	309
B1	260	B2	260	B3	268
C1	239	C2	252	C3	259
D1	236	D2	250	D3	264
E1	266	E2	280	E3	289

Fracture toughness of composites A1, B1 and C1 produced by pressure-less sintering and the samples produced by pressure-less sintering followed by hipping was between 1.9 to 3.0MPa•$m^{1/2}$ (Figure 13). Fracture toughness of composites A1 to C1 was almost independent of sintering temperature. Hipping increased fracture toughness. Fracture toughness increased slightly in the order A1 to C1.

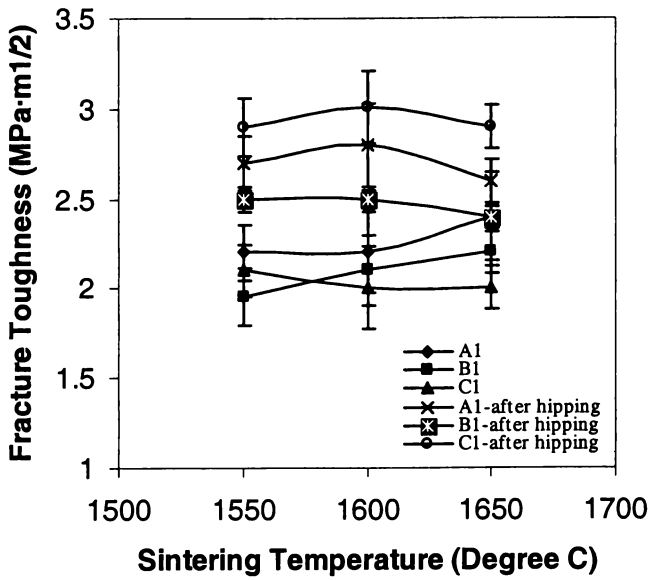

Figure 5.13 Fracture toughness of α-Ti(Al,O) based composites A1, B1, and C1 before and after hipping as a function of the sintering temperature.

Fracture toughness of composites D1 and E1 was independent of pre-sintering temperature (Figure 5.14). Hipping increased fracture toughness of composites D1 and E1 to by about 7%.

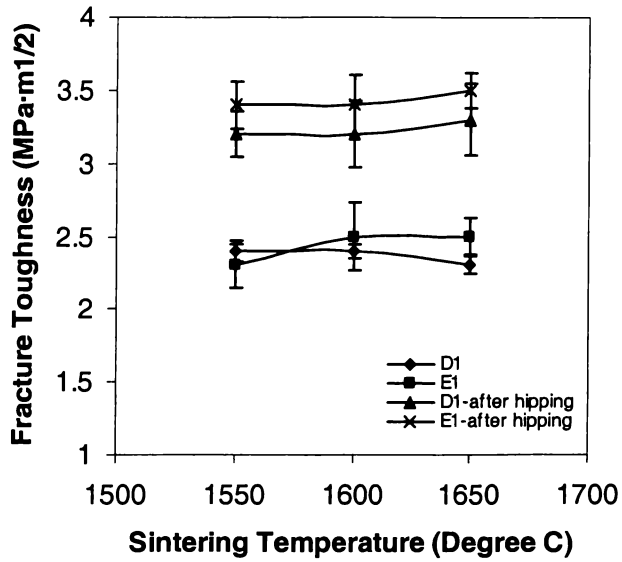

Figure 5.14 Fracture toughness of $Al_2Ti_4C_2$ based composites D1 and E1 before and after hipping as a function of the sintering temperature.

Composite A2, B2 and C2 produced by pressure-less sintering had fracture toughness values 2.0 to 2.5 MPa•$m^{1/2}$ (Figure 5.15). Fracture toughness of composite B2 increased slightly with sintering temperature but fracture toughness of composites A2 and C2 slightly decreased after sintering at 1650°C. Hipping increased fracture toughness of composites A2, B2 and C2 about 20%.

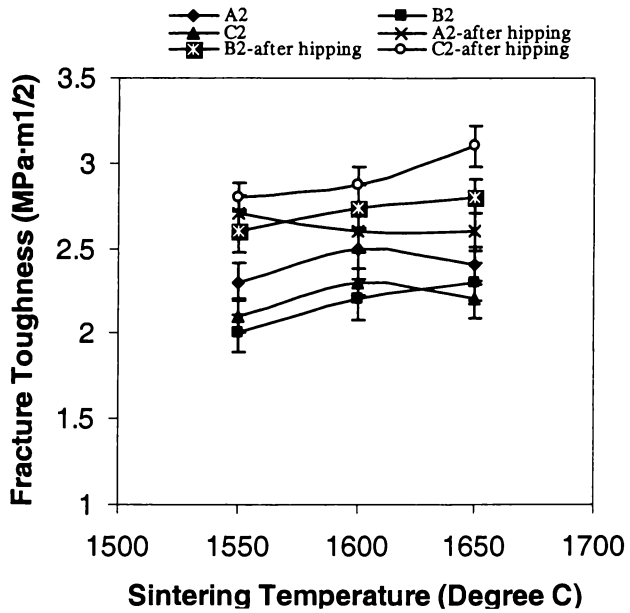

Figure 5.15 Fracture toughness of Ti_3Al based composites A2, B2, and C2 before and after hipping as a function of the sintering temperature.

Fracture toughness of composite D2 and E2 was almost independent of sintering temperature between 1550 to 1650°C (Figure 5.16). Hipping increased fracture toughness of composites D2 and E2 by about 1-9%.

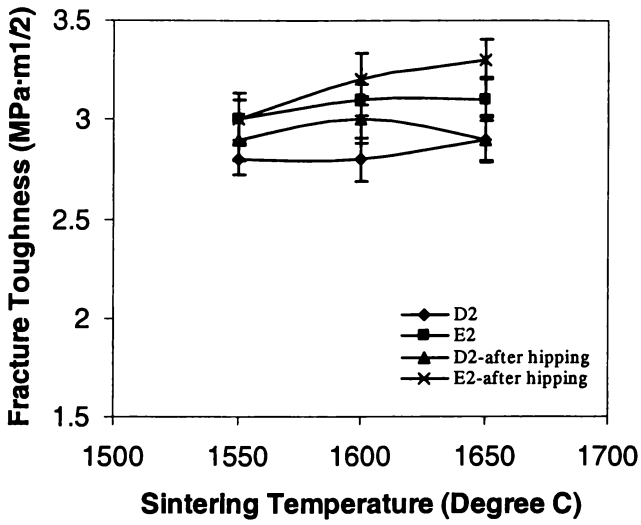

Figure 5.16 Fracture toughness of $Al_2Ti_4C_2/Ti_3Al$ based composites D2 and E2 before and after hipping as a function of pressure-less sintering temperature.

Fracture toughness of composites A3, B3, and C3 was almost independent of sintering temperature and increased in the order of composite A3, B3 and C3 (Figure 5.17). Hipping increased fracture toughness of these three composites by 4-7%.

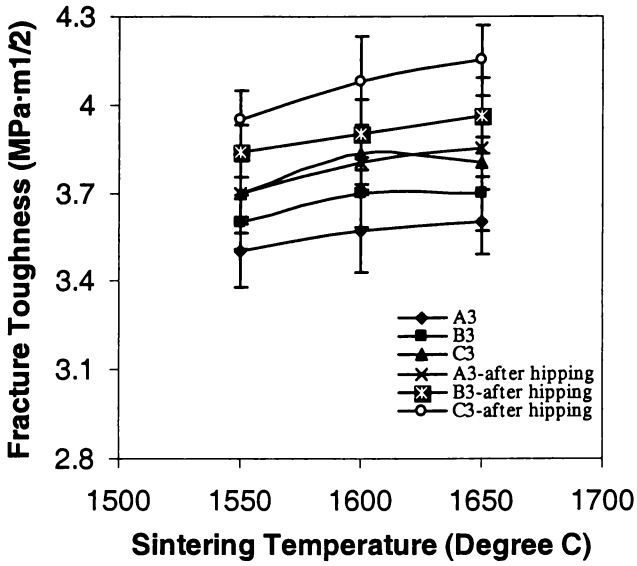

Figure 5.17 Fracture toughness of TiAl based composites A3, B3, and C3 before and after hipping as a function of pressure-less sintering temperature.

Fracture toughness of composites D3 and E3 produced by pressure-less sintering increased slightly as sintering temperature increased from 1550°C to 1600°C and was independent of sintering temperature above 1600°C (Figure 5.18). Hipping increased fracture toughness of these two composites by 4-7%.

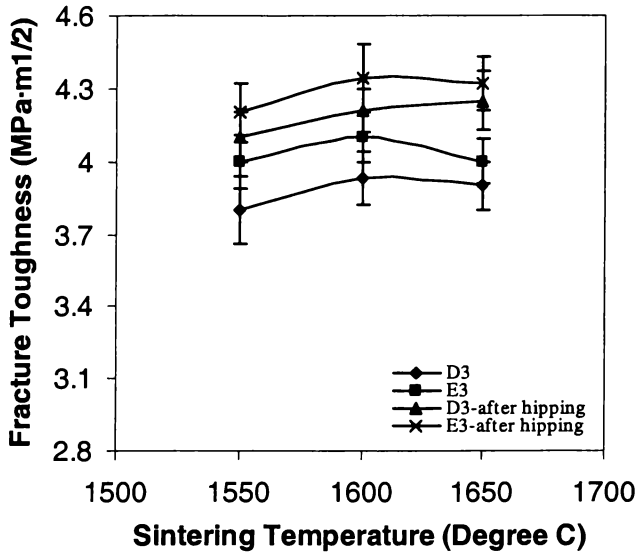

Figure 5.18 Fracture toughness of $Al_2Ti_4C_2$/TiAl based composites D3 and E3 before and after hipping as a function of the sintering temperature.

5.5 Fracture surface and crack path

Fracture surfaces from bending test samples of composites A1 and E1 produced by pressure-less sintering at 1550°C and 1650°C are shown in Figure 5.19. The fracture of the α-Ti(Al,O) metallic phase and the Al_2O_3 particles in composite A1 was transgranular. For composite E1, the fracture surface of the $Al_2Ti_4C_2$ phase was mainly transgranular but the small Al_2O_3 particles were not fractured. Instead they were separated from the matrix by decohesion.

The crack in composite A1 propagated by penetrating the Al_2O_3 particles and α-Ti(Al,O) metallic phase after indentation (Figure 5.20). The crack propagated along an almost straight line. The crack in composite E1 propagated with deflections in the α-Ti(Al,O) metallic phase and penetrated the large Al_2O_3 particles. However, the crack did not appear to penetrate the small Al_2O_3 particles; instead it went through the particle/matrix interface.

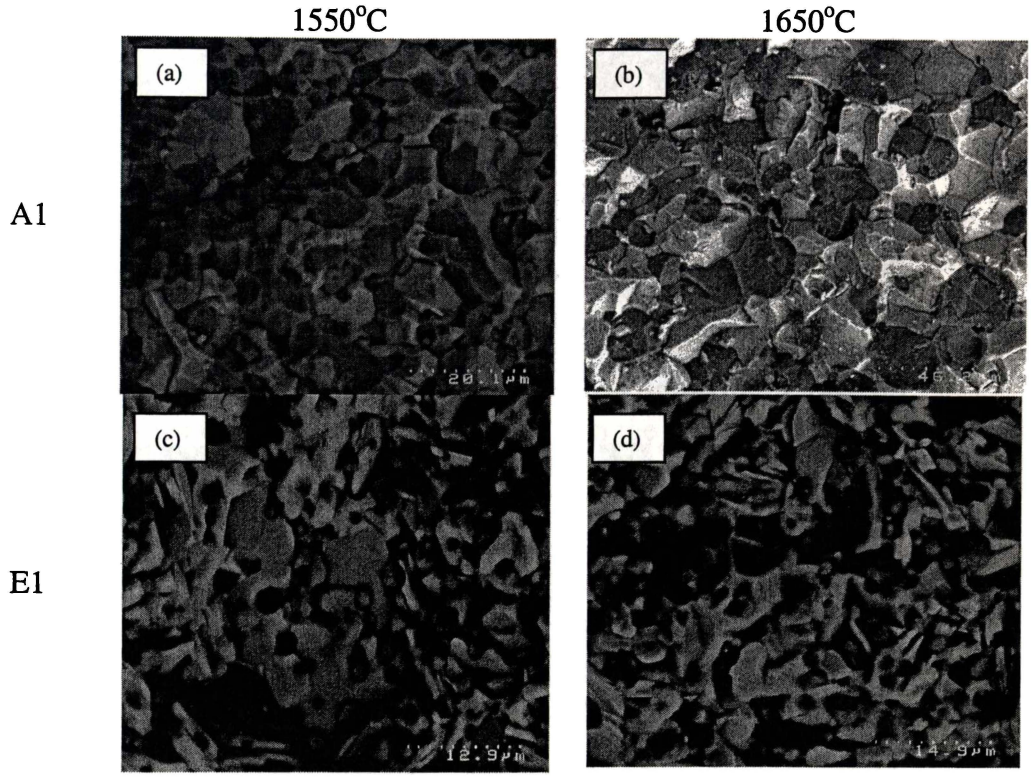

Figure 5.19 Fracture surface of composites A1 and E1 pressure-less sintered at 1550°C and 1650°C.

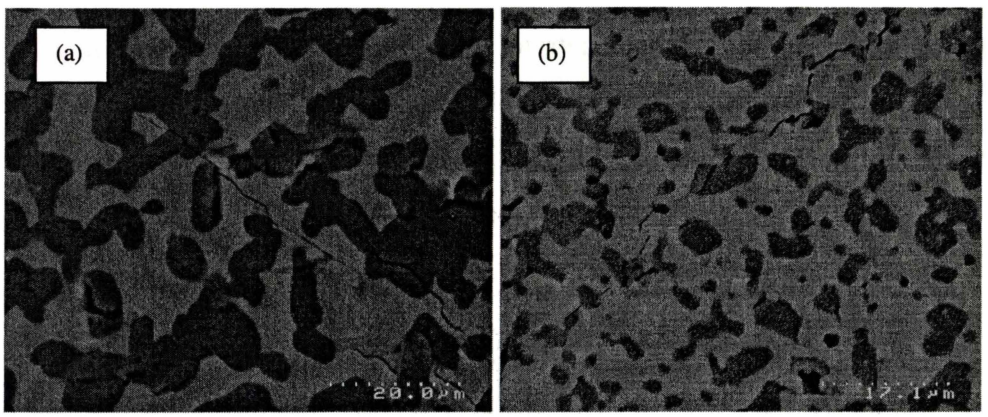

Figure 5.20 Typical crack path of composites A1 (a) and E1 (b) after indentation.

The fracture of composite A3 produced by pressure-less sintering at 1550°C and 1650°C was dominated by transgranular fractures of the TiAl metallic phase and Al_2O_3 particles (Figure 5.21). The fracture surface of the TiAl phase has a lamina structure, expected for γ-TiAl [3]. The large Al_2O_3 particles in composite E3 exhibited transgranular fracture while the small Al_2O_3 particles did not fractured but separated from the matrix by decohesion.

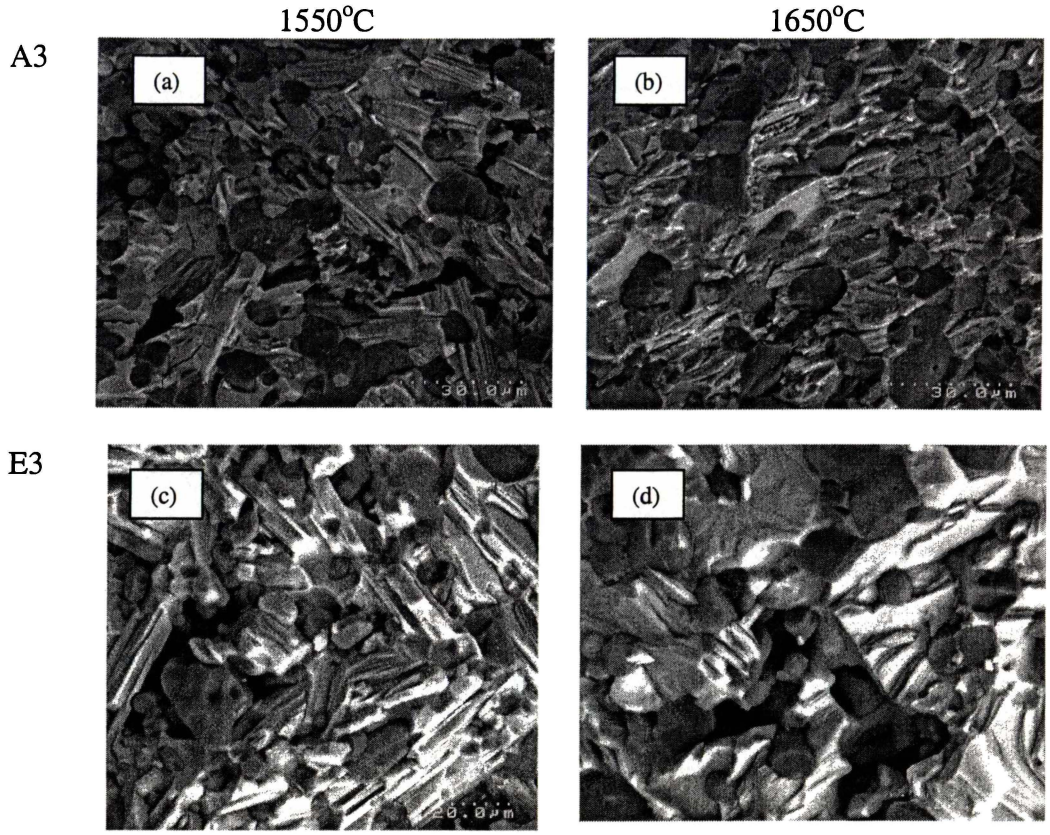

Figure 5.21 Fracture surface of composites A3 and E3 pressure-less sintered at 1550°C and 1650°C.

For composite A3, the crack penetrated the Al_2O_3 particles near the indent and then the crack deflected in the matrix and propagated along the interface between Al_2O_3 particles and the matrix (Figure 5.22). The crack in composite E3 did not penetrate the small Al_2O_3 particles but went through the particle/matrix interface.

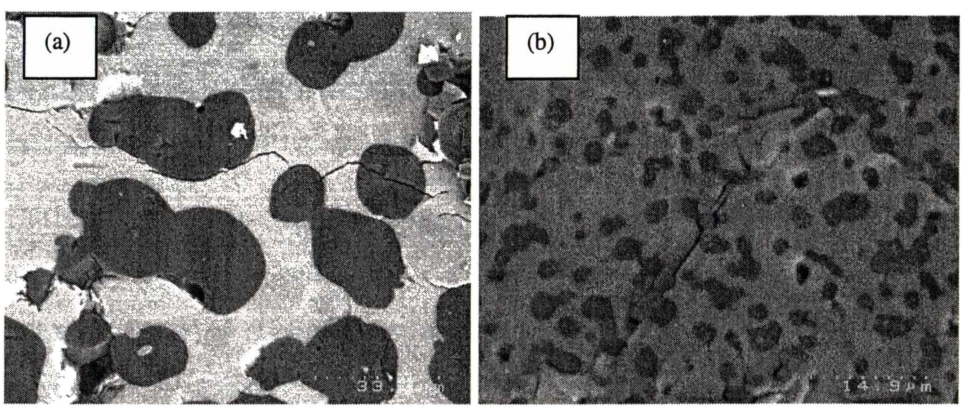

Figure 5.22 Typical crack path of composites A3 (a) and E3 (b) after indentation.

5.6 Discussion

5.6.1 Effect of porosity on mechanical properties

Hardness decreased linearly with increasing sample porosity demonstrating the pores significantly affect hardness of composites (Figure 5.23). The decrease in hardness with porosity was greater for composites A1 and A2 than the composites A3, E1, E2, and E3. This indicates that hardness of TiAl and $Al_2Ti_4C_2/Ti_xAl_y$ based composites is less affected by porosity than the α-Ti(Al,O) and Ti_3Al based composites. Other factors such as the Al_2O_3 particle size or volume fraction may also affect hardness.

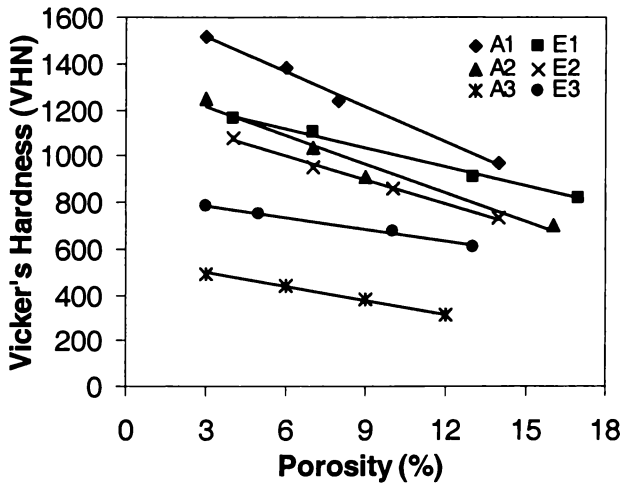

Figure 5.23 Effect of porosity on Vicker's hardness of composites A1, A2, A3, E1, E2 and E3.

Bending strength decreased linearly with increasing porosity. Bending strength of composites E1, E2, and E3 decreased more rapidly than those of composites A1, A2, and A3 (Figure 5.24). This was not unexpected as increasing pore fraction, especially as open pores, will affect bending strength. Pores affect stress distribution and induced stress concentration [4-7]. Pores can induce cracks, and fracture energy will be released as the cracks propagate. The reason for $Al_2Ti_4C_2$ based composites to have a higher rate of decreasing bending strength with increasing the porosity level is because they are ceramic based composites. Ceramic phases are less tolerant of pores because it is difficult to produce plastic zones ahead of the crack tips. On the other hand, composites A1, A2, and A3 can tolerate pores better because it can produce plastic zones at the crack tips.

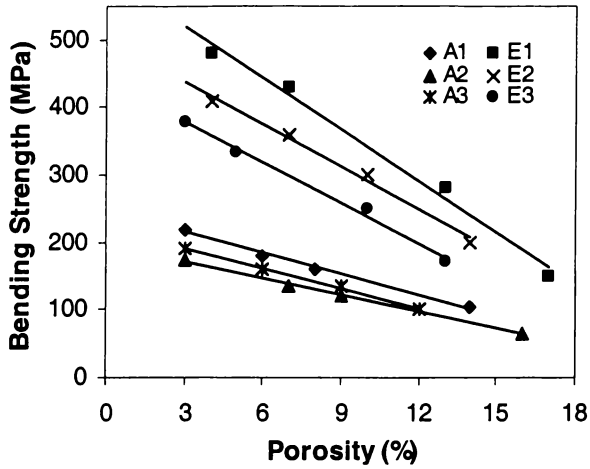

Figure 5.24 Effect of porosity on bending strength of composites A1, A2, A3, E1, E2 and E3.

5.6.2 Effect of Al_2O_3 particle size on mechanical properties

Hardness of composites A1, A2, E1 and E2 increased with Al_2O_3 particle size is greater than that of composites A3 and E3 (Figure 5.25). Hardness of composites A3 and E3 is almost independent of Al_2O_3 particle size, probably because they have a relatively low volume fraction of Al_2O_3 particles (47 and 37 vol% respectively). Thus, hardness of the matrix will dominate overall hardness of the composites. Composition and oxygen content of the matrix can also affect hardness of the matrix. Ti is harder than TiAl, and the α-Ti(Al,O) phase contains more oxygen than the TiAl matrix. Therefore, hardness of the α-Ti(Al,O) phase will be higher than that of the TiAl phase. Large Al_2O_3 particles increase hardness of composites due to the large contact areas to Al_2O_3 particles. Other researches report that the composites with large Al_2O_3 particles are harder than composites with small particles [8-9]. The size of the Al_2O_3 particles had the same effect on hardness of composites E1 and E2.

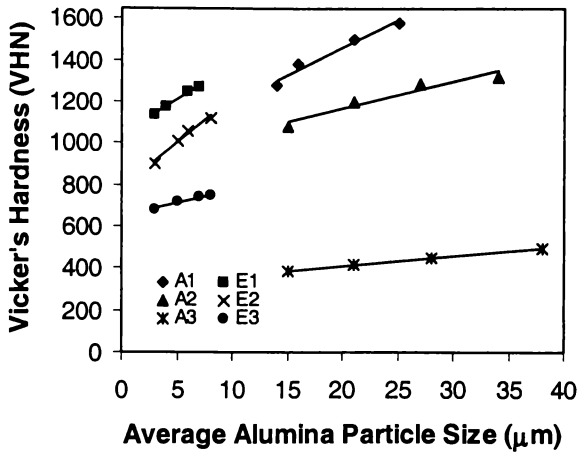

Figure 5.25 Effect of average Al_2O_3 particle size on Vicker's hardness of composites A1, A2, A3, E1, E2 and E3.

Bending strength decreased with increasing average Al_2O_3 particle size (Figure 5.26). Bending strength of composites E1, E2, and E3 decreased more rapidly than that of composites A1, A2, and A3. A previous study of Al-alloy/SiC composite explained that bending strength decreases with increasing ceramic particle size [7]. This study indicates that the critical size of Al_2O_3 particles is 10 μm. Below this, bending strength dramatically improves with decreasing Al_2O_3 particle size. When average Al_2O_3 particle size is less than 10 μm, the composites fracture by decohesion between the Al_2O_3 particles and the matrix. When the average Al_2O_3 particle size is labove 10 μm, the composites fracture by transgranular fracture of Al_2O_3 particles. The effect of Al_2O_3 particle size on bending strength can be explained by the high stress concentration around the ceramic particles. The reinforcement particles have a greater Young's modulus than the matrix [10-11]. When average Al_2O_3 particle size is small, more Al_2O_3 particles are present in a given volume of the composite (Figure 5.27). Therefore, stress concentration on each Al_2O_3 particle is less. Under these conditione, the stress is insufficient to fracture the Al_2O_3 particles, therefore, the Al_2O_3 particles detach from the matrix. After the Al_2O_3 particles coarsen, the average number of Al_2O_3 particles in the composite is reduced. Therefore, stress concentrates on each of the large Al_2O_3 particles and the average stress required to fracture the Al_2O_3 particles decreases. In the meantime, transgranular fracturing of the large Al_2O_3 particles in the composite causes large cracks in the material, which will accelerate crack propagation. These decrease strength of the composites. A

previous study also mentioned that the number of cracked reinforcement particles increased with increasing particle size [12].

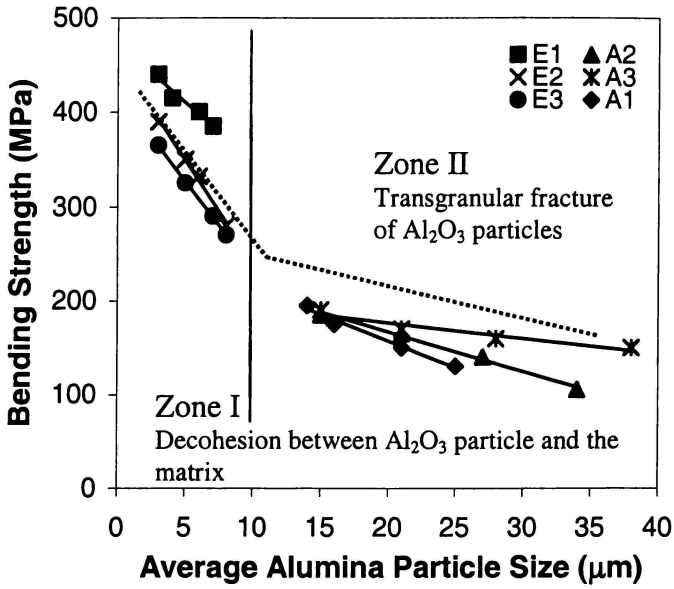

Figure 5.26 Effect of average Al_2O_3 particle size on bending strength of composites A1, A2, A3, E1, E2 and E3.

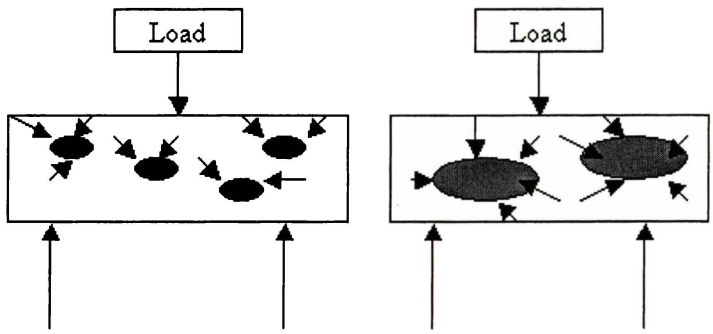

Figure 5.27 Schematic stress distributions in composites indicating effect of Al_2O_3 particle size.

5.6.3 Effect of Al_2O_3 volume fraction on mechanical properties

Vicker's hardness of α-Ti(Al,O), Ti_3Al and TiAl based composites with similar porosity increased as the Al_2O_3 volume fraction increased (Figure 5.28). This is understandable as Al_2O_3 particles are much harder than the Ti_xAl_y matrix. Hardness of α-Ti(Al,O) and Ti_3Al based composites increased more rapidly with volume fraction of Al_2O_3 particles than the TiAl based composites. This is

because the α-Ti(Al,O) and Ti_3Al based composites have relative higher volume fraction of Al_2O_3 particles than the TiAl based composites.

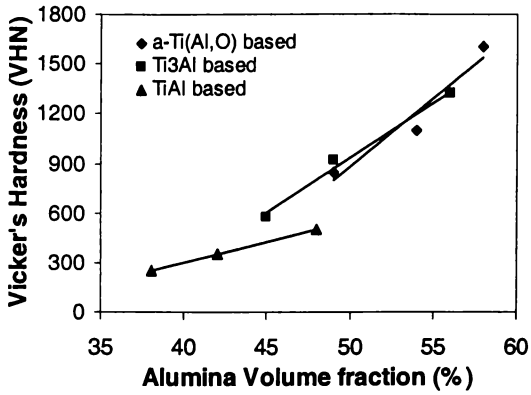

Figure 5.28 Effect of volume fraction of Al_2O_3 particles on Vicker's hardness of α-Ti(Al,O), Ti_3Al and TiAl based composites.

Bending strength of α-Ti(Al,O), Ti_3Al and TiAl based composites decreased linearly with increasing Al_2O_3 volume fraction (Figure 5.29). The volume fraction of Al_2O_3 particles had a similar effect on all three composites of similar sized Al_2O_3 particles. Having higher volume fraction particles gives a greater probability that the large Al_2O_3 particles will fracture when a load is applied. Therefore, composites with higher volume fractions of Al_2O_3 particles may fracture at a lower maximum stress in a bending situation.

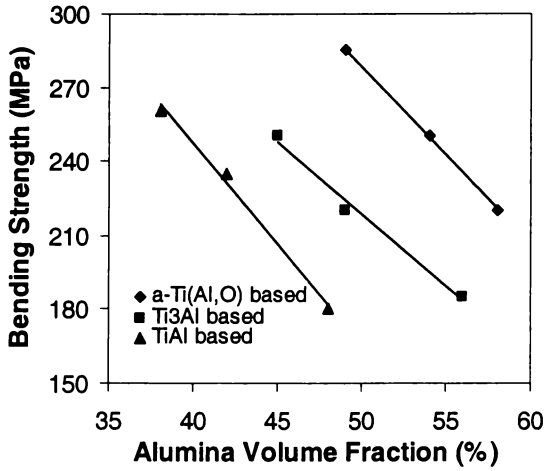

Figure 5.29 Effect of Al_2O_3 volume fraction on bending strength of α-Ti(Al,O), Ti_3Al and TiAl based composites.

5.6.4 Fracture toughness of the composites

All composites produced in this study have similar fracture toughness in range 2 to 4.3 $MPa \bullet m^{1/2}$. Fracture toughness was almost independent of porosity level and

Al_2O_3 particle size. The slight change in fracture toughness is due to the different matrices in the composites. The study also showed that fracture toughness increased slightly with decreasing Al_2O_3 volume fraction, indicating that all these materials are brittle. Fracture toughness of the composites was similar to that of a pure Al_2O_3 ceramic.

The reasons that α-Ti(Al,O), Ti_3Al and TiAl based composites have a low fracture toughness is that the metallic or intermetallic matrices have a high oxygen content. Ti(Al)-alloys with aluminum contents less than 10 at.% can dissolve a maximum of 28 at.% oxygen at 1100°C in equilibrium with Al_2O_3 [13]. The present study showed that the α-Ti(Al,O), Ti_3Al and TiAl phases contained 28, 19 and 4 at.% oxygen respectively after sintering at 1650°C. Oxygen can embrittle titanium and titanium aluminides [14-17]. The embrittled α-Ti(Al,O), Ti_3Al and TiAl phases are not expected to provide ductile ligaments to bridge cracks as occurs for ductile metals in normal metal-ceramic composites. The slightly higher fracture toughness of TiAl based composite over that of α-Ti(Al,O) and Ti_3Al based composites might be due to the low oxygen content in the TiAl phase.

The $Al_2Ti_4C_2$ based composites E1, E2, and E3 have slightly higher fracture toughness than the Ti_xAl_y based composites even though they are ceramic-ceramic composites. This might be due to the small Al_2O_3 particles in the composites. Cracks cannot penetrate the small Al_2O_3 particles; instead the crack deflects and propagates along interfaces between the Al_2O_3 particles and the matrix. This effect releases fracture energy and increase the toughness of the composites.

5.7 Summary

The size and volume fraction of Al_2O_3 particles in the composites strongly affected the mechanical properties of the Ti_xAl_y and $Al_2Ti_4C_2$ based composites produced in this study. The α-Ti(Al,O), Ti_3Al, and $Al_2Ti_4C_2$ based composites had a hardness values of 800-1600 VHN. The hardness of TiAl based composites was in the range 150-500 VHN. The Ti_xAl_y/Al_2O_3 composites had bending strength in the range 105-230 MPa, while the high bending strength of $Al_2Ti_4C_2/Ti_xAl_y/Al_2O_3$/TiC based composites was 250-460 MPa. Fracture

toughness of these composites was 2-4.5 MPa•$m^{1/2}$. Increasing Al_2O_3 particle size and volume fraction increased hardness and decreased bending strength.

References

1. I.J. Polmear, Light alloys, Third edition, ARNOLD, (1995).
2. TAPP version 2.2, E S Microware Inc. Hamilton, OH 45013 (1996).
3. G.R. Anstis, P.Chantikul, B.R. Lawn, D.B. Marshall, J. Am. Ceram. Soc. **64,** 533-538, (1981).
4. Y. Yoshino, J. Am. Ceram. Soc., **72**, 1322-1327, (1989).
5. G.G. Garret and J.F. Knott, Metall. Trans. **9A**, 1187-1193, (1978).
6. G. LeRoy, J.D. Embury, G. Edwards and M.F. Ashby, Acta Metall. **29**, 1509-1515, (1981).
7. D.L. Davidson, Metall. Trans. **18A**, 2115-2120, (1987).
8. R.J. Arsenault, S. Fishman, M. Taya, Progress in Materials Science, **38**, 1-157, (1994).
9. M.K. Srivastava, R.K. Maradal, S. Mohan, J.P. Pathak, S.N. Ojha, India Journal of Engineering and Materials Science, **6**, 27-33, (1999).
10. K.J. Bhansali, R. Mehrabian, J. Metals, **9**, 30-36, (1982).
11. N. Hansen, Acta Metall., **25**, 863-871, (1997).
12. R.J. Arsenault, N. Shi, Mater. Sci. Eng. **81**, 175-179, (1986).
13. T. Mochida, M. Taya, D.J. Lloyd, Mater. Trans. JIM, **32**, 931-938, (1991).
14. B.J. Lee, N. SaunderZ. Metallkd., **88**, 152-161, (1997).
15. T. Kawabata, M. Tadano, O. Izumi, Scr. Metall., **22**, 1725-1730, (1988)
16. Y.M. Kim, JOM, **41**, 24-30, (1989).
17. S. Yamauchi, H. Shiraish, Mater. Sci. Eng. A, **A152**, 283-287, (1992).

Chapter Six
Conclusions and Recommendations

6.1 Conclusions

- Ti_2O_3 powder can be produced by heating a C/TiO_2 composite powder with a suitable C/TiO_2 ratio to a high temperature. When the C/TiO_2 ratio in the starting composite powder is high enough, TiO_nC_{1-n} ($n<1$) forms. It is not possible to obtain pure TiO by reacting between carbon and TiO_2.

- At a high C/TiO_2 ratio, the starting reaction temperature decreases due to a finer C/TiO_2 composite structure.

- α-$Ti(Al,O)/Al_2O_3$, Ti_3Al/Al_2O_3, and $TiAl/Al_2O_3$ based composites can be produced by reacting between Al and TiO_2 or Ti_2O_3.

- The reactions between Al and TiO_nC_{1-n}, form $Al_2Ti_4C_2/Al_2O_3$ ceramic-ceramic composites. When the amount of aluminium in the starting Al/TiO_nC_{1-n} composite powders increases $Al_2Ti_4C_2$ still forms but small amounts of Ti_3Al and TiAl also form.

- Whether TiC forms from the reaction between Al and TiO_nC_{1-n} depends on the n value. When n is small enough, TiC forms; otherwise TiC does not form.

- The matrices of Ti_xAl_y/Al_2O_3 and $Al_2Ti_4C_2/Ti_xAl_y/Al_2O_3/TiC$ composites became fully sintered at 1550°C. However, to fully sintering Al_2O_3 particles the temperature must be above 1550°C.

- The coarsening rate of Al_2O_3 particles in the α-Ti(Al,O) and Ti_3Al based composites is high if the temperature is above 1550°C, indicating that oxygen and Al diffusion rates in α-Ti(Al,O) and Ti_3Al are very high.

- The coarsening rate of Al_2O_3 particles in TiAl based composites is high above 1550°C indicating TiAl became liquid at these temperatures.

- The Al_2O_3 particles in $Al_2Ti_4C_2/Ti_xAl_y/Al_2O_3/TiC$ based composites have a much lower coarsening rate, because $Al_2Ti_4C_2$ matrix has a low oxygen content and high melting point, which decreases oxygen and aluminum mobility.

- The size and volume fraction of Al_2O_3 particles in the composites strongly affect the mechanical properties of the Ti_xAl_y and $Al_2Ti_4C_2$ based composites produced.

- α-Ti(Al,O), Ti_3Al, and $Al_2Ti_4C_2$ based composites have a hardness of 800-1600 VHN and TiAl based composites had a hardness of 150-500 VHN.

- Ti_xAl_y/Al_2O_3 composites have a bending strength of 105-230 MPa and $Al_2Ti_4C_2/Ti_xAl_y/Al_2O_3/TiC$ based composites have a bending strength of 250-460MPa. The much higher bending strength of the later composite is due to the much smaller size of the Al_2O_3 particles.

- Bending strength dramatically improves with decreasing Al_2O_3 particle size below a critical Al_2O_3 size of 10 μm.

- Fracture toughness of the composites produced is 2-4.5 $MPa \bullet m^{1/2}$.

- Hardness increases and bending strength decreases with increasing Al_2O_3 particle size and volume fraction.

6.2 Potential use of materials

- The composite materials produced in this study show brittle mechanical properties. Composite strength is comparable to most of the ceramic materials. These composites have the advantage of low cost processing.

The composites could be used in where the application does not involve dramatic impact.

6.3 Recommendations for future work

- Having fine Al_2O_3 particles uniformly distributed in a metallic matrix should give good mechanical properties. To achieve this optimum microstructure in composites, different processing techniques such as adding sintering additives to decrease coarsening of Al_2O_3 particles should be investigated.

- Further work is needed to quantify n of TiO_nC_{1-n} phase.

- The effects of volume fraction and TiC particle size in the $Al_2Ti_4C_2/Ti_xAl_y/Al_2O_3/TiC$ composites should be further studied.